

Coupling dynamics to chemical modeling:  
The effects of episodic accretion and episodic  
outflow on the chemistry of protostellar cores

Inaugural-Dissertation

zur

Erlangung des Doktorgrades  
der Mathematisch-Naturwissenschaftlichen Fakultät  
der Universität zu Köln



vorgelegt von

**Nassim Tanha**  
aus Tehran, Iran

Cologne, 2023

Berichterstatter (Gutachter):

Prof. Dr. Peter Schilke

Prof. Gary Fuller, PhD

Vorsitzender der Kommission:

Prof. Dr. Susanne Crewell

Tag der mündlichen Prüfung:

24. Oktober 2023

# Abstract

Low mass proto-stars commonly go through a phase of episodic accretion. These systems exhibit a rich and diverse chemistry. In this thesis, I present a study of the spatio-temporal evolution of interstellar complex organic molecules (iCOMs) in an episodic accretion scenario, with the aim of understanding the processes involved in the early phases of star formation and the coeval chemical evolution. I post-process smoothed particle hydrodynamics (SPH) simulations of low-mass star formation in collapsing, turbulent prestellar cores. The included sub-grid episodic accretion model efficiently heats the proto-stellar accretion disk and drives episodic outflows (Rohde et al., 2021). I extract the density and temperature evolution of a subset of SPH particles and apply the astro-chemistry code Saptarsy (Choudhury et al., 2015). Saptarsy is a rate-equation-based 1D astro-chemical code which includes gas-phase reactions, gas-grain interactions and surface chemistry, as well as multilayered dust chemistry.

I investigate the time evolution of different gas phase tracers and look at the effects of the episodic flares on the chemistry surrounding the proto-stars. The flares produce an abrupt temperature change with a lifetime of a few decades. I find that different species react differently, a group of species are elevated in the interior e.g.  $\text{CH}_3\text{OH}$  abundance changes by 3 orders of magnitude within 1500 AU, whereas some others like  $\text{HCO}^+$  get destroyed, decreases abundance by 2 orders of magnitude within 1000 AU. The response time to the flares varies considerably and some molecules are not affected at all.

I focus further on methanol as the smallest and the predecessor to other iCOMs, whose abundance is systematically underestimated in most existing chemical models. The spread of abundance systematically increases in the smaller radii and reaches above 10 orders of magnitude within 400 AU, because accretion mixes material with different thermal history onto the disk. Therefore the inhomogeneity of the chemistry systematically increases with decreasing radius. Furthermore, I show outflows entrain methanol rich material as far as 10 000 AU.

I use a visualization tool, Saptalizer (Schaefer, 2017) to analyze the detail of chemistry and show methanol is destroyed in temperatures above 500 K in gas phase, by reacting with atomic hydrogen. It is produced on dust via hydrogenation of frozen out formaldehyde in temperatures  $T \sim 80$  K, while in lower temperatures of  $T \sim 30$  K it is produced by hydrogenation of frozen out carbon monoxide. The difference lies in different desorption temperatures of dust species.

This work suggests that dynamic physical modeling has non-linear and non-negligible effect on the chemistry. One can use this behavior to build a dynamic chemical clock for protostellar cores.

# Contents

<b>1</b>	<b>Introduction</b>	<b>1</b>
1.1	Star formation . . . . .	2
1.1.1	Interstellar Medium . . . . .	2
1.1.2	Molecular clouds . . . . .	3
1.1.3	Core collapse . . . . .	4
1.2	Astrochemistry . . . . .	6
1.2.1	Gas chemistry . . . . .	8
1.2.2	Dust chemistry . . . . .	10
1.2.3	Chemistry in protostellar cores . . . . .	12
<b>2</b>	<b>Methodology I</b>	<b>14</b>
2.1	(Magneto-)Hydrodynamic Simulations . . . . .	14
2.1.1	SPH codes . . . . .	15
2.1.2	Gravity . . . . .	16
2.1.3	Sink particles . . . . .	17
2.1.4	Simulation set up . . . . .	17
2.2	Chemistry Simulations . . . . .	19
2.2.1	Reaction rates and chemical network . . . . .	20
2.2.2	Saptarsy and Simulation set up . . . . .	22
2.3	RADMC-3D . . . . .	24
<b>3</b>	<b>Methodology II: Coupling dynamics to chemistry</b>	<b>26</b>
3.1	Sampling the gas . . . . .	26
3.2	Calculating the dust temperature . . . . .	27
3.2.1	Griding up the particles . . . . .	28
3.2.2	Amplifying the luminosity . . . . .	29
3.2.3	RADMC-3D Monte Carlo calculation . . . . .	31
3.3	Chemistry simulations . . . . .	33
<b>4</b>	<b>Results and discussion</b>	<b>37</b>
4.1	Temperature bins and chemical memory . . . . .	40
4.2	Radial bins and the range of accretion heating on chemistry . . . . .	49
4.2.1	Mid-range . . . . .	50
4.2.2	Exterior . . . . .	53
4.2.3	Interior . . . . .	57
4.3	Violin plots and chemical inhomogeneity . . . . .	63
4.3.1	Interior . . . . .	65
4.3.2	Mid-range . . . . .	72

4.3.3 Exterior . . . . .	79
<b>5 Conclusion and outlook</b>	<b>89</b>
5.1 Summary . . . . .	89
5.2 Outlook . . . . .	91
5.2.1 Astrochemistry . . . . .	91
5.2.2 Synthetic emission maps and comparison with observation	92
<b>References</b>	<b>93</b>
<b>Acknowledgement</b>	<b>106</b>

## List of Figures

1	A schematic picture of magnetic breaking. The image is taken from the book Ward-Thompson and Whitworth (2011). Reproduced with permission of The Licensor through PLSclear. . . . .	5
2	Artistic demonstration of how an accretion disk transitions from routine magnetospheric accretion to outburst accretion, accompanied by a rise in luminosity. Taken from Fischer et al. (2022). Credit: Caltech/T. Pyle (IPAC). Courtesy NASA/JPL-Caltech . .	6
3	A schematic picture of different phases of proto-stellar evolution. The image is taken from the book Ward-Thompson and Whitworth (2011). Reproduced with permission of The Licensor through PLSclear. . . . .	7
4	An illustration of a simplified physical and chemical structure of a protostellar core. Reprinted from Ceccarelli et al. (2023), with permission from the editors of PPVII as well as the author. . . .	12
5	A schematic illustration of SPH approach to calculate density. . .	16
6	Column density of the hydrodynamic simulation of a core collapse by Rohde et al. (2021) at $t = 50.0$ kyr. This is the simulation I use in this work. . . . .	20
7	The relative difference between the temperatures from Hydrodynamic GANDALF simulations and the dust temperatures calculated by RADMC3D versus the distance of the particles from the center for the test case. . . . .	28
8	Total mass versus total luminosity of the protostars from proto-stellar evolution model for different accretion rates. Over plotted are the sink particles from the HD GANDALF simulations . . . .	30
9	Histogram of temperature distribution for resolution tests of RADMC-3D with $10^7$ , $10^8$ and $10^9$ photon packages . . . . .	32
10	Zoomed-in histogram of temperature distribution for resolution tests of RADMC-3D with $10^7$ , $10^8$ and $10^9$ photon packages . . .	32
11	Grid resolution test for (top) the snapshot right after the first flare at 45.6 kyr and (bottom) the snapshot right after the second flare at 59.6 kyr into the simulation . . . . .	34
12	Relative difference between the number of particles of the two grids in different refinement levels, in each temperature bin for the snapshot right after the first flare at 45.6 kyr and the snapshot right after the second flare at 59.6 kyr into the simulation . . . . .	35

13	A flowchart of the pipeline of simulations, starting from hydrodynamic simulation as the physical model to the chemistry simulations.	36
14	(top)The projection of the trajectory of an example particle on x-y plane. This is an in-falling particle. The color bar shows the time. Note that the protostars and hence, the center of the in-fall moves throughout the simulation. (middle)The input of Saptarsy, including temperature and density of the example particle and (bottom)the output of Saptarsy for the example particle, only a few species are shown here as examples. The solid lines are gas and the dash lines are dust abundance. . . . .	38
15	zoom in on the left side of the middle and bottom panels of Figure 14 . . . . .	39
16	The trajectories (top), the densities (middle) and the temperatures (bottom) of a randomly selected subset of the SPH particles throughout the simulation; about 0.5 percent of the total number of SPH particles. . . . .	41
17	The gas (top) and the dust (bottom) abundance of methanol for a randomly selected subset of the SPH particles throughout the simulation . . . . .	42
18	Mean abundance in temperature bins. Each bin has a fixed number of particles (1500 particles). Different times are different line colors. The red line is the snapshot right before the first flare and the rest of the lines are the times after that flare and each is 1 kyr apart. The top panel is the gas and the bottom panel is the dust abundance . . . . .	43
19	The same plot as Figure 18, only for the second flare. . . . .	45
20	Mean abundance of ammonia (left panel) and water (right panel) in temperature bins, with the same procedure as Figure 18. . . . .	46
21	Mean abundance of HNC (left panel) and HCN (right panel) in temperature bins, with the same procedure as Figure 18. . . . .	47
22	Mean abundance of $\text{HCO}^+$ (left panel) and $\text{N}_2\text{H}^+$ (right panel) in temperature bins, with the same procedure as Figure 18. . . . .	47
23	Mean abundance of $\text{H}_2\text{S}$ (left panel) and $\text{SO}$ (right panel) in temperature bins, with the same procedure as Figure 18. . . . .	48
24	The distance between the two protostars as they revolve around each other throughout the simulation. . . . .	49

25	4 dimensional mean methanol gas abundance in logarithmically-spaced radial bins. The x axis is time, the y axis is radius and the surface is the mean gas abundance in the radial bins ( $n_x/n_H$ ). The color-bar is the temperature in kelvin. The top and bottom panel show two different angles of the plot. . . . .	51
26	Position of the two protostars throughout the time interval of the simulation we are using for our work. The position of the middle of the line connecting the two protostars is overlaid. . . . .	52
27	Column density map of the region of roughly 3000 AU radius from the binary protostars, which covers the mid-region. This is a snapshot at 50 kyr into the simulations and is located between our first two flares. . . . .	53
28	Mean gas (upper) and dust (bottom panel) abundance of methanol in 6 radial bins, i.e annuli around the protostars, between 400 and 3000 AU. The vertical lines indicate the position of the flares. . .	54
29	Mean temperature (upper) and density (bottom panel) in the same 6 radial bins as 28. We keep the same color scheme, which means we go from lighter to darker colors as we go from inner to outer layers between 400 and 3000 AU and the vertical lines indicate the position of the flares. . . . .	55
30	Time evolution of mass (upper panel) and luminosity (lower panel) of the protostars. . . . .	56
31	Column density map of the region of roughly 10000 AU, which covers the exterior region. This is a snapshot at 50 kyr into the simulations and is located between our first two flares. . . . .	57
32	Mean gas (upper) and dust (bottom panel) abundance of methanol in 5 radial bins, i.e annuli around the protostars, between 3000 and 10000 AU. The vertical lines indicate the position of the flares. . .	58
33	Mean temperature (upper) and density (bottom panel) in the same 5 radial bins as Figure 32. We keep the same color scheme, which means we go from lighter to darker colors as we go from inner to outer layers between 3000 and 10000 AU and the vertical lines indicate the position of the flares. . . . .	59
34	Column density map of the region of roughly 400 AU, which covers the interior region. This is a snapshot at 50 kyr into the simulations and is located between our first two flares. . . . .	60
35	Mean gas (upper) and dust (bottom panel) abundance of methanol in 5 radial bins, i.e annuli around the protostars, between 200 and 400 AU. The vertical lines indicate the position of the flares. . . .	61

36	Mean temperature (upper) and density (bottom panel) in the same 3 radial bins as Figure 35. We keep the same color scheme, which means we go from lighter to darker colors as we go from inner to outer layers between 200 and 400 AU and the vertical lines indicate the position of the flares. . . . .	62
37	Methanol abundance in gas and dust over plotted with temperature for one example particle, produced by Saptalizer. . . . .	63
38	Methanol formation (top) and destruction (bottom) rates on dust grains for one example particle, produced by Saptalizer. . . . .	64
39	Distribution of methanol abundance for every snapshot(every 200 yr) between the first and second flares at 45.4 and 59.4 kyr(upper panel) for dust and gas between the radii 200 and 266 AU. (Bottom panel) The temperature distribution of the same radius bin. This plot is the distribution for the most inner ring of Figure 35 between the first and second peak. . . . .	65
40	Distribution of methanol abundance for one in every 10 snapshot (every 2 kyr) between the second and third flares at 59.4 and 115.8 kyr (upper panel) for dust and gas between the radii 200 and 266 AU. (Bottom panel) The temperature distribution of the same radius bin. This plot is the distribution for the most inner ring of Figure 35 between the second and third peak. The vertical dashed lines are the accretion events corresponding to the two protostars. . . . .	66
41	Methanol chemistry on the second flare, for material in temperatures above 500 K, which is losing its dust and gas abundance. J as prefix of chemical species specifies the dust content. . . . .	67
42	Methanol chemistry right after the second flare, for material which have already lost their methanol content in both gas and dust and have temperatures around 80 K and are rebuilding methanol on dust. J as prefix of chemical species specifies the dust content. . . . .	68
43	The mass ratio of the material with methanol abundance higher than $10^{-6}$ between 200 and 266 AU radii, which where at larger radii at the moment of the second flare to the total mass in the same radii. The time interval is between the second and the third flare. This is the same time interval and radius bin as Figure 40 between the second and third peak and it is calculated for every time step. The vertical dashed lines are the accretion events corresponding to the two protostars. . . . .	70

44	Distribution of methanol abundance for every snapshot (every 200 yr) from the third flare until the end of simulation at 115.8 and 177.8 kyr(upper panel) for dust and gas between the radii 200 and 266 AU. (Bottom panel) The temperature distribution of the same radius bin. This plot is the distribution for the most inner ring of Figure 35 after the third peak. The vertical dashed lines are the accretion events corresponding to the two protostars. . . . .	71
45	distribution of methanol abundance for every snapshot (every 200 yr) between the first and second flares at 45.4 and 59.4 kyr upper panel) for dust and gas between the radii 400 and 833 AU. (Bottom panel) is the temperature distribution of the same radius bin. This plot is the distribution for the most inner ring of Figure 28. The vertical dashed lines are the accretion events corresponding to the two protostars. . . . .	73
46	distribution of methanol abundance for one in every 10 snapshot (every 2 kyr) between the second and third flares at 45.4 and 59.4 kyr (upper panel) for dust and gas between the radii 400 and 833 AU. (Bottom panel) is the temperature distribution of the same radius bin. This plot is the distribution for the most inner ring of Figure 28. The vertical dashed lines are the accretion events corresponding to the two protostars. . . . .	74
47	distribution of methanol abundance for every snapshot (every 200 yr) between the second and third flares at 45.4 and 59.4 kyr (upper panel) for dust and gas between the radii 400 and 833 AU. (Bottom panel) is the temperature distribution of the same radius bin. This plot is the distribution for the most inner ring of Figure 28. The vertical dashed lines are the accretion events corresponding to the two protostars. . . . .	75
48	Methanol chemistry on the flare, for material in temperatures between 200 and 500 K, which is loosing its dust and gas abundance due to thermal desorption. J as prefix of chemical species specifies the dust content . . . . .	76
49	Methanol chemistry right after the flare, for material which has been heated up between 200 and 500 K, has lost its dust methanol content during the flare due to thermal desorption and now has cooled down to around 30 K and is rebuilding methanol on dust. J as prefix of chemical species specifies the dust content. . . . .	77
50	Comparison of the desorption time of different species as a function of dust temperature . . . . .	79

51	distribution of methanol abundance for every snapshot (every 200 yr) between the first and second flares at 45.4 and 59.4 kyr (upper panel) for dust and gas between the radii 8600 and 10000 AU. (Bottom panel) is the temperature distribution of the same radius bin. The vertical dashed lines are the accretion events corresponding to the two protostars. . . . .	80
52	distribution of methanol abundance for one in every 10 snapshot (every 2 kyr) between the second and third flares at 45.4 and 59.4 kyr (upper panel) for dust and gas between the radii 8600 and 10000 AU. (Bottom panel) is the temperature distribution of the same radius bin. The vertical dashed lines are the accretion events corresponding to the two protostars. . . . .	81
53	distribution of methanol abundance for every snapshot (every 200 yr) between the second and third flares at 45.4 and 59.4 kyr (upper panel) for dust and gas between the radii 8600 and 10000 AU. (Bottom panel) is the temperature distribution of the same radius bin. The vertical dashed lines are the accretion events corresponding to the two protostars. . . . .	82
54	Mass ratio of migrated methanol rich material. These are the ratio of the number of particles with gas abundance higher than $5.0e^{-6}$ , between 8600 and 10000 AU which were at a radii less than 3000 AU on the second flare, to the total particles in this region. The vertical dashed lines are the accretion events corresponding to the two protostars. . . . .	83
55	Trajectories (upper panel) and the densities (middle pannel) and the temperatures (bottom panel) of the entrained particles. These are particles with gas abundances higher than $5.0e^{-6}$ , between 8600 and 10000 AU which were at a radii less than 3000 AU on the second flare at the peak of Figure 54. . . . .	85
56	The gas (upper panel) and dust (bottom panel) abundances of methanol for entrained particles. These are particles with gas abundances higher than $5.0e^{-6}$ , between 8600 and 10000 AU which were at a radii less than 3000 AU on the second flare at the peak of Figure 54. . . . .	86
57	Methanol abundance on gas (left) and dust (right) of the SPH particles, in snapshots right before the first flare (top), on the first flare (middle) and right after the first flare (bottom). . . . .	87

58	Methanol abundance on gas (left) and dust (right) of the SPH particles for the snapshot with the highest enrichment of methanol in outer region. . . . .	88
----	--	----

## List of Tables

1	List of gas phase reactions included in Saptarsy. . . . .	23
2	List of dust phase reactions included in Saptarsy. . . . .	23
3	List of gas grain interactions included in Saptarsy. . . . .	23
4	The binding energy of different species to ice layers on the dust. .	78

# 1 Introduction

The history of science starts with astronomy. "Where do these bright points in the night sky, which we call stars, come from?" This question has accompanied humankind since the dawn of civilization. Throughout the centuries we have learned a lot about the universe beyond our planet and yet, there are still many questions unanswered about how star forms.

We know that the stars are not uniformly scattered in the universe. They are organized in very massive structures we call galaxies. Galaxies convert their material into stars. Where stars are formed within galaxies; how efficient do galaxies produce stars; what is the distribution of physical properties of the resulting stars and how it is all related to the environment they are formed in, are all subjects of research in the field of star formation.

The medium within a galaxy between the stars is called the interstellar medium (ISM). It is the birth place of the stars and it is affected by the feedback from the stars in turn. As such, the study of ISM, as the ecosystem in which stars are born and die, is interconnected with star formation. Stars form in the densest and coldest part of the ISM. Cold and dense enough for gas to be found in molecular form and make up for a rich chemistry.

Physics and chemistry are coupled in the ISM. On the one hand, the physical properties of this medium, such as its local temperature and density and the amount of radiation can affect whether different molecules can react with each other and if so, how fast these reactions take place. On the other hand, certain chemical reactions are endothermic and can remove thermal energy of the ISM and cool down the gas, which again affects the dynamic of the gas. In fact, one of the main cooling mechanisms of the ISM is the formation of CO, which plays a key role in the formation of the so called molecular clouds (Draine, 2010; Tielens, 2005; Ward-Thompson & Whitworth, 2011), or the nurseries of stars. In this chapter, I talk more about the physics and the chemistry of the ISM and how they interact with each other.

Another reason which makes chemistry of the ISM an important subject for astrophysicists, is the fact that a big portion of the data, we gather from the space and specifically the molecular clouds are chemical data. Molecules emit photons which we observe with our telescopes. Consequently, we need to understand the intersection of chemistry and physics in the ISM to be able to map these chemical information into physical data. Then studying the chemical compositions of astronomical sources gives us information about the physical conditions and the processes involved in the formation of those sources. Therefore, knowing about molecular evolution, gives us information about the places in the ISM

where molecules exist, namely, the molecular clouds. Molecular clouds are the places where star formation takes place. Hence we learn about the physics of star formation by studying the formation of molecules in the ISM.

Proper modeling of the ISM should include the coupled behavior of the physics and chemistry, but so far the physical models which are used for chemical modelings are rather simple, with simplified geometry, such as 1D or sometimes 2D models, i.e. spherical or cylindrical geometries, and simplified time evolution, following semi-analytical models of star formation. But we know that the star forming regions are extremely complex, highly dynamic and non-symmetric systems. In fact, we utilize sophisticated numerical simulations to deal with the complexity of the physical processes involved in the ISM. The main idea of this work is to develop a method to couple dynamics to chemistry and I do it by post processing the hydrodynamic simulations of a core collapse with the chemistry code Saptarsy.

One could raise the question, why not implement a full chemical model in the hydrodynamic simulations instead of post processing, since that is the most realistic approach to modeling. The answer lies in the feasibility of such simulations. Adding a full chemical model to the hydrodynamic simulations will make them too expensive and unfeasible. Furthermore, not all of the chemical reactions are dynamically relevant. Glover and Clark (2012) have shown that a very simplified chemical model including only Hydrogen chemistry with 8 reactions and a reduced model of CO formation and destruction (Nelson & Langer, 1997) is enough for calculating the effects of chemistry on the dynamic of the gas. In other words, we do not need to include a big and computationally expensive network into the hydrodynamic simulations, and only a reduced one is enough and the rest can be done in a post processing step. In this work, I look at the effects of this kind of dynamic modeling on the chemistry of star formation.

## 1.1 Star formation

In this section I talk briefly about how material is organized in the ISM and how it is related to start formation, followed by what we know about the star formation process.

### 1.1.1 Interstellar Medium

The matter in the interstellar medium consists of gas and dust, which is distributed inhomogeneously throughout the galaxy. The dust is made of graphite and amorphous silicate solid particles and has 1% of the mass of the ISM. The gas is found to exist in distinct phases based on its thermal and chemical properties

(see for example Tielens (2005); Klessen and Glover (2016)).

- **Hot ionized medium (HIM):** These are mainly produced by supernova explosions in very hot ( $T \sim 10^6$  K) ionized bubbles of gas. They are the hottest regions of the galaxy with the lowest densities ( $\rho \sim 10^{-2} \text{ cm}^{-3}$ ) and fill most of the volume of the halo.
- **Warm ionized medium (WIM):** It is 90 percent of the total ionized gas within the ISM and is very diffused and has a scale height of the order of 1 kpc. Its temperature is around 8000 K and its density is between 0.2 to  $0.5 \text{ cm}^{-3}$  and has a rather large filling factor.
- **Warm neutral medium (WNM):** These regions have temperatures between 6000 and 10 000 K and densities comparable to WIM, have a large scale height of 220 pc.
- **Cold neutral medium (CNM):** 80 percent of the atomic hydrogen is in the diffuse HI clouds with a low scale height of 100 pc. They have a similar densities as the WNM, but less temperatures of 50 to 100 K.
- **Molecular gas:** The coldest ( $T \sim 10\text{-}20$  K) and the densest ( $\rho > 10^2 \text{ cm}^{-3}$ ) phase of the ISM, which is distributed in discrete regions we call molecular clouds. Molecular clouds are the nurseries of the stars and as such their properties are very interesting and important for the field of star formation. In the next section, I will talk about Molecular clouds and their properties in more detail.

### 1.1.2 Molecular clouds

The ISM is a highly turbulent environment, where the gas is constantly changing between different phases. Molecular clouds are formed by the convergence of turbulent flows. These flows of gas are caused by different sources of energy. One is feedback from stars in forms of outflows, radiation, stellar winds and the most energetic of all, supernovae and the other is global collapse and gravity within the galaxy.

Molecular clouds mainly consist of molecular gas, from which the main contributor is  $\text{H}_2$  and some He (around 26%). Molecular clouds cover a big range of physical properties. Their mass varies between  $10^2 M_\odot$  and  $10^7 M_\odot$  and their size between  $\sim 1$  to  $\sim 100$  pc and densities between  $\sim 10$  to  $10^4 \text{ cm}^{-3}$ . (See Draine (2010); Dobbs et al. (2014); Chevance et al. (2022))

Molecular clouds are inhomogeneous on all scales (Ward-Thompson and Whitworth (2011)). They are highly structured and filamentary. (André et al. (2014),

Pineda et al. (2022)). Filaments fragment into dense cores. If the cores are gravitationally unstable, they will further collapse and form stars. I will discuss the core collapse in more detail in the next section.

### 1.1.3 Core collapse

A gravitationally unstable pre-stellar core collapses isothermally, while its density is low enough that it remains optically thin and can radiate away the gravitational energy. The isothermal collapse continues until the density is high enough for the core to become optically thick to its own cooling radiation. It then starts to heat up as it contracts and finally ends up in a hydrostatic equilibrium i.e. the internal pressure supports the opaque central object against its gravity. This hydrostatic object, often called the first hydrostatic core, or the protostar, is embedded in a relatively diffused infalling envelope.

As the envelope gets more dense, it becomes more optically thick and the luminosity decreases. The temperature at the outer edge of the envelope remains constant, while the temperature of the inner region of the protostar increases. The protostar starts accreting from the envelope, as it stays in hydrostatic equilibrium and contracts quasi-statically. Since the accreting material has angular momentum, a circumstellar disk forms, where the material accumulates and spirals inwards onto the equator of the protostar. The protostar remains convective in this phase.

As the core collapses with any angular momentum, the conservation of angular momentum dictates that the angular velocity increases with the decreasing radius, which in turn increases the rotational energy. The increasing rotational energy would balance the gravitational energy and halts the collapse, if there would not be a mechanism to remove some angular momentum from the system. This problem is commonly known as the angular momentum problem in star formation. protostars are often observed to have bipolar outflows, which are thought to solve the angular momentum problem. These outflows are along the rotation axis and perpendicular to the accretion disk. The outflows are believed to be caused by the so-called magnetic braking. Figure 1 shows this mechanism.

Magnetic field is frozen into the ISM in most places, i.e. the ISM and the magnetic field are coupled. The magnetic field lines twist as the core rotates while collapsing. It produces torsional waves which travel along the field lines with high velocity and drag some of the material with them and spin them up and thus removes the angular momentum from the core. From observation we know that the outflows start as high velocity jets ( $\sim 500$  AU). As the jets hits the surrounding gas, they produce very compact, shock-heated objects called Herbig-Hebro objects ( $\sim 5000$  AU) and sweep up and accelerate the gas very far from

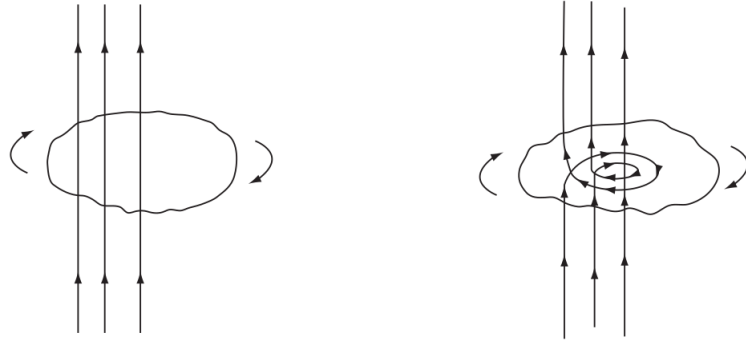


Figure 1: A schematic picture of magnetic breaking. The image is taken from the book Ward-Thompson and Whitworth (2011). Reproduced with permission of The Licensor through PLSclear.

the protostar and produce diffused lobes of high velocity gas ( $\sim 50\,000$  AU).

One of the accretion scenarios is the episodic accretion model. As the name suggests, it refers to a model where the accretion rate is time dependent and is not continuous and instead, most of the accretion happens in short outbursts. It was first introduced as a possible solution to the so-called luminosity problem. Based on observations, the stellar mass and accretion time scales do not match up with the accretion rates derived from the observed luminosity of protostars (Kenyon et al., 1990; Kenyon & Hartmann, 1995; Evans et al., 2009) and the protostars are under-luminous. Episodic accretion solves this problem by keeping the average accretion rate to what the models calculate from the observed luminosity, while the protostars spend most of their life during the low-accretion phase, where they are also mostly observed. Episodic accretion is a typical phenomenon in low mass star formation, as we now know. Certain examples of episodic accretion include the FU Orionis objects (FUors). Young stellar objects (YSO) known as FUors exhibit rapid enhancement in accretion rates from  $10^{-7}$  to  $10^{-4} M_{\odot}\text{yr}^{-1}$  that last for decades or longer (Audard et al., 2014). There are other types of accretion variability, which could explain the luminosity curves of protostars as well. For a comprehensive review see Fischer et al. (2022).

The interaction between the magnetic field of the protostar and the accretion disk is believed to control the accretion. The inner edge of the accretion disk is truncated by the magnetosphere of the protostar. Disk material is then channeled from the disk inner edge onto the star along the magnetic field lines (Bouvier, Alencar, Harries, Johns-Krull, & Romanova, 2007) producing a funnel flow. This is the general mechanism of the accretion for low mass accretion rates (between  $10^{-7}$  to  $10^{-6} M_{\odot}\text{yr}^{-1}$ ). Some other mechanism should break the magnetospheric accretion to produce the outbursts. This is still not well known and there are different schools of thought. I discuss one model which is the base of the subgrid



Figure 2: Artistic demonstration of how an accretion disk transitions from routine magnetospheric accretion to outburst accretion, accompanied by a rise in luminosity. Taken from Fischer et al. (2022). Credit: Caltech/T. Pyle (IPAC). Courtesy NASA/JPL-Caltech

model used in the simulations I have used for this work. For further reading please see (Audard et al., 2014).

A combination of gravitational instability (GI) and magnetorotational instability (MRI), can be used to explain FUors outbursts, because they both can transfer angular momentum in disks. If the disk becomes sufficiently cool or has high enough surface density, GIs can occur and cause spiral waves and transport angular momentum efficiently outwards, thus transport mass inwards (see Durisen et al. (2007) and the references therein). Mass keeps piling up in the inner disk and heats it up, which increases the collisional ionization. This process continues until the ionization is high enough that the disk couples with the magnetic field and triggers MRI, which transports angular momentum (see Balbus and Hawley (1998) and the references therein) and causes an outburst of material onto the protostar, hence raising the luminosity. Figure 2 shows the quiescent and the outburst states of an episodic accretion model. Zhu, Hartmann, and Gammie (2009); Zhu, Hartmann, Gammie, and McKinney (2009); Zhu et al. (2010) has developed a MRI triggered episodic accretion model, based on which (Stamatellos, Whitworth, & Hubber, 2012) has developed a subgrid model which was used in core collapse MHD simulations of (Rohde et al., 2019, 2021, 2022). These are the simulations I use in this work.

As the star continues to contract and heat up, radiative energy transport takes over the convection. The opacity changes and luminosity starts to rise again. When the protostar and its disk has emptied the envelope from gas, the remaining object is called a pre-main-sequence star. Once the temperature of the interior of the core reaches the hydrogen burning phase, the star formation is complete. Figure 3 shows the schematic presentation of different proto-stellar phases.

## 1.2 Astrochemistry

The first molecule discovered in space was CH in 1937 Dunham (1937); Swings and Rosenfeld (1937). Since then the number of molecules found in the ISM

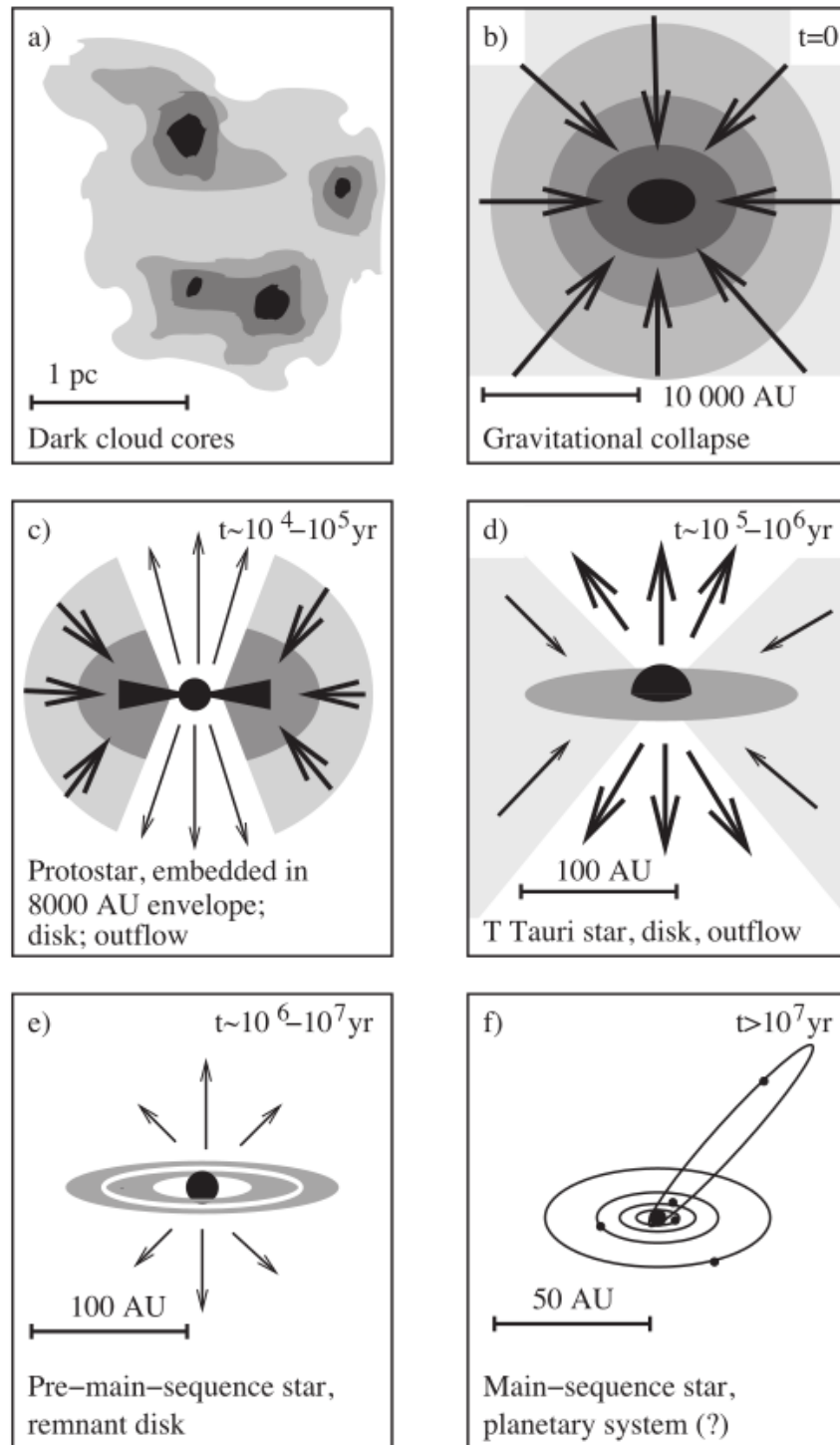


Figure 3: A schematic picture of different phases of proto-stellar evolution. The image is taken from the book Ward-Thompson and Whitworth (2011). Reproduced with permission of The Licensor through PLSclear.

has reached above 290 and counting (The Cologne Database for Molecular Spectroscopy). One calls the molecules in the ISM with more than six atoms and at least one carbon atom, interstellar complex organic molecules (iCOM) Ceccarelli et al. (2017); Herbst and van Dishoeck (2009). iCOMs amount to 40% of the detected molecules in space and are considered the link between interstellar chemistry and the emergence of life on Earth Ceccarelli et al. (2023). Astrochemistry is in other words molecular astrophysics and studies how molecules are formed and destroyed in space and how they interact with their physical environment van Dishoeck (2018). In this section, I talk about different types of reactions in the ISM and how they are linked to the physics of the ISM. In the end, I discuss the chemistry of a collapsing core.

### 1.2.1 Gas chemistry

Molecular clouds are hostile environments for chemical reactions. The dense parts of the ISM have lower densities than what we consider to be a vacuum on Earth. Similarly, the temperatures in the molecular clouds are very low ( $\rho \sim 10^2 \text{cm}^{-3}$   $T \sim 10 - 20$  K). These conditions make certain reactions inefficient. For example, reactions of the type



is very inefficient in molecular clouds. Since the product is only stable if it can get rid of the excess energy, released from the reaction. Hence, the stability depends on a third collisional party which can absorb the extra energy. But the very low density of the molecular clouds makes the probability of such a third body collision very low. The same goes for reactions of the type



There needs to be another party so that the excess energy can turn into kinetic energy of the products traveling in opposite directions, hence the most common type of efficient reaction in the ISM is



Furthermore, the reactions have to be exothermic and are not to have energy barriers. As a result of low temperature of the molecular clouds, the environment cannot provide the necessary energy for these reactions to take place.

Another important component of the chemical reactions in the ISM is the degree of ionization. There are different sources of ionization in the interstellar medium. Stars emit UV radiation which can ionize or dissociate molecules. Espe-

cially in clouds near high mass stars, interstellar UV radiation becomes important, although they cannot penetrate into the dense cores (Yamamoto, 2017). Another source of ionization is the so called cosmic rays. Cosmic rays are high energy particles, mainly relativistic protons, some helium ions, little electrons and some heavier ions, which are accelerated above the thermal velocity distribution. (Draine, 2010; Tielens, 2005). Cosmic rays can ionize the gas and the resulting energetic electrons can excite  $\text{H}_2$  molecules, thus producing UV radiation (Prasad & Tarafdar, 1983; Gredel, Lepp, Dalgarno, & Herbst, 1989). Since cosmic rays can penetrate the dense gas, via this cosmic ray-induced UV radiation, photoprocesses can occur even in dense cores in the absence of interstellar UV radiation.

Shocks can also produce UV radiation. Fast shocks dissociate molecules and within the post shocked gas,  $\text{H}^+$  ions recombine with electrons and emit the famous Lyman- $\alpha$  1216 Å line (Hollenbach & McKee, 1979; Neufeld & Dalgarno, 1989; Yamamoto, 2017).

The possible reactions can be categorized into different reaction types, which I discuss in the following.

- **Ion-molecule reactions:** As a result of all the ionization sources, mentioned before, molecular clouds are weakly ionized and the degree of ionization depends on the density. Thus ion-molecule reactions are important.
- **Neutral-neutral reactions:** This is the most "simple" type of reaction, which is an important contributor to the gas reactions in the ISM.
- **Radiative association reactions:** These are reactions of the type:



where two reactants collide and emit a photon to stabilize. Radiative electron recombination reaction falls under this category, where an electron recombines with an ion. So is radiative electron attachment reaction, where a negative ion is formed by attaching an electron to a neutral atom or molecule.

- **Dissociative electron recombination:** These reactions are of the type:



where a molecular ion and an electron react and produce two or more products. This reaction type is essential in producing neutral species in the ISM. The molecular ions used in this reaction type are usually formed by ion-molecule reactions.

- **Photodissociation and Photoionization:** As it was discussed before, the ISM is filled with UV radiation, . UV radiation can (photo-)dissociate or (photo-)ionize the molecules it interact with. Photoprocesses are the most significant in the periphery of a molecular cloud. deeper in the cloud they lose their importance by increasing attenuation of the UV radiation by the dust grains and increasing visual extinction,  $A_V$ . If a species is abundant, (for example  $H_2$  and CO), the molecules in the periphery of the cloud dissociate and use up all the UV radiation and the molecules deeper in the cloud of the same species will not go through photodissociation. This mechanism is called self-shielding. The more abundant molecules can also shield other less abundant species by accidental overlapping of transition frequencies.

### 1.2.2 Dust chemistry

Interstellar dust grains play a crucial role in the rich chemistry of molecular clouds. Dust grains act as the facilitator of chemical reactions in cold molecular clouds. In the previous section, I discussed how reaction type mentioned in Equation 1 are not efficient, as we need a third body to remove the excess energy of the reaction. Dust can act as that third body and absorb the extra energy by warming up. For example, the most abundant molecule in the ISM,  $H_2$ , can only be efficiently produced on dust (Hollenbach & Salpeter, 1970; Vidali, 2013). But for that, the atoms and molecules need to get on the dust first.

The grain cores have a typical radius of  $0.1 \mu\text{m}$  and are covered by water ice mantle. In cold molecular clouds, when molecules collide with dust grains, they stick to the grain by van der Waals or electrostatic force. The adsorbed molecules can thermally desorb into the gas again. There is a temperature for each species below which the molecule is efficiently removed from the gas and it is referred to as desorption temperature or sublimation temperature. This process is called depletion. If a reaction should follow, the atoms and molecules should be able to move on the surface, so they can encounter and react with one another. The minima of the interaction potential of the chemical species and the dust surface are called the 'sites', where the chemical species are adsorbed. If the molecules can overcome the barrier energy between the sites, they can hop between the sites. This barrier energy is commonly assumed to be half of the desorption energy for simplicity. H atom is an exception, because it is light enough to move through quantum tunneling. Thus even at low temperatures of around 10 K H atoms are mobile and reactive.

Many important molecules are formed on the grain surface through hydrogenation chains, such as methane ( $CH_4$ ), methanol ( $CH_3OH$ ), water ( $H_2O$ ) and

ammonia ( $\text{NH}_3$ ). Dust chemistry is also the onset of reactions which produce iCOMs. Besides hydrogenation, radicals play an important role in producing big molecules, as they are also very reactive. Radicals are formed via different processes on the dust. They can form as byproducts of hydrogenation reactions. Another contribution comes from photodissociation of molecules by either interstellar UV radiation (for low  $A_v$ ), or cosmic ray-induced UV radiation (for high  $A_v$ ).

After molecules are formed on the dust grains, they will remain there, unless the dust temperature reaches the desorption temperature of these species. However, we observe iCOMs such as ( $\text{HCOOCH}_3$ ,  $\text{CH}_3\text{OCH}_3$ ,  $\text{CH}_3\text{CHO}$  and  $\text{CH}_3\text{OH}$ ) in cold clouds Jiménez-Serra et al. (2016) for L1544 in Taurus, Bacmann, Taquet, Faure, Kahane, and Ceccarelli (2012) for L1689B and Taquet et al. (2017) for Barnard 5 in Perseus). Hence either these molecules are not produced on dust grains, or there must be non-thermal desorption mechanism, which can release the species on dust into the gas phase, even in low temperatures. There is no consensus on what these other processes are (Wakelam et al., 2021; Jørgensen, Belloche, & Garrod, 2020; van Dishoeck, 2018). Different models are suggested for non-thermal mechanisms for desorption of dust-produced species off the dust. I will list some of these models.

Exothermic reactions can release the product into the gas phase, by using the excess energy of the reaction to overcome the binding energy between the product and the surface. This process is called chemical desorption (Yamamoto et al., 2019; Minissale et al., 2016; Garrod et al., 2007). Cosmic rays can directly affect the ice chemistry in various ways (Wakelam et al. (2021) and the references therein), such as heating the dust grain (Shen et al., 2004; Leger et al., 1985) and sputtering the ice mantle (Toulemonde et al., 2000). UV radiation, either from the external stars in low density regions or cosmic-ray induced UV radiation in high density regions can cause photodesorption (Wakelam et al., 2021; Yamamoto, 2017). While these and other models are the subjects of many lab experiments and studies, the efficiency of these mechanisms is not fully constrained and our models are yet to properly produce the observed abundances of iCOMs. Methanol specifically is under-produced in these models (Wakelam et al., 2021; Bertin et al., 2016; Martín-Doménech et al., 2016). In this work, by coupling dynamics to the chemical models I find another candidate to produce iCOMs in cold cores, namely a combination of episodic accretion heating to release the dust species into the gas phase and episodic outflow to move the chemically rich material outwards.

### 1.2.3 Chemistry in protostellar cores

Planetary systems form around low-mass stars. This makes the chemical studies of low mass star forming regions important, as it can connect the chemistry in the large scale and molecular clouds to the planets. The chemistry of low mass star forming regions starts in the late 80s and early 90s by first observations of some molecules in dark cores (Suzuki et al., 1992; Zhou et al., 1989; Benson & Myers, 1989). Later on, it was discovered that there is a very small (a few tens of AUs) and hot region around the low-mass protostars. It was followed by detection of different iCOMs in low mass star forming regions (Cazaux et al., 2003). In this work, I model the chemistry of low-mass protostellar cores, hence in what follows I discuss the chemistry in these objects and how it is related to their physical parameters in the state of the art chemical models in more detail.

If one simplifies the structure of a solar-like protostellar cores to a central source of heat and an infalling envelope with a density profile that peaks toward the center, one can divide its chemical structure into three main zones. Figure 7 shows an illustration of these zones (Ceccarelli et al., 2023).

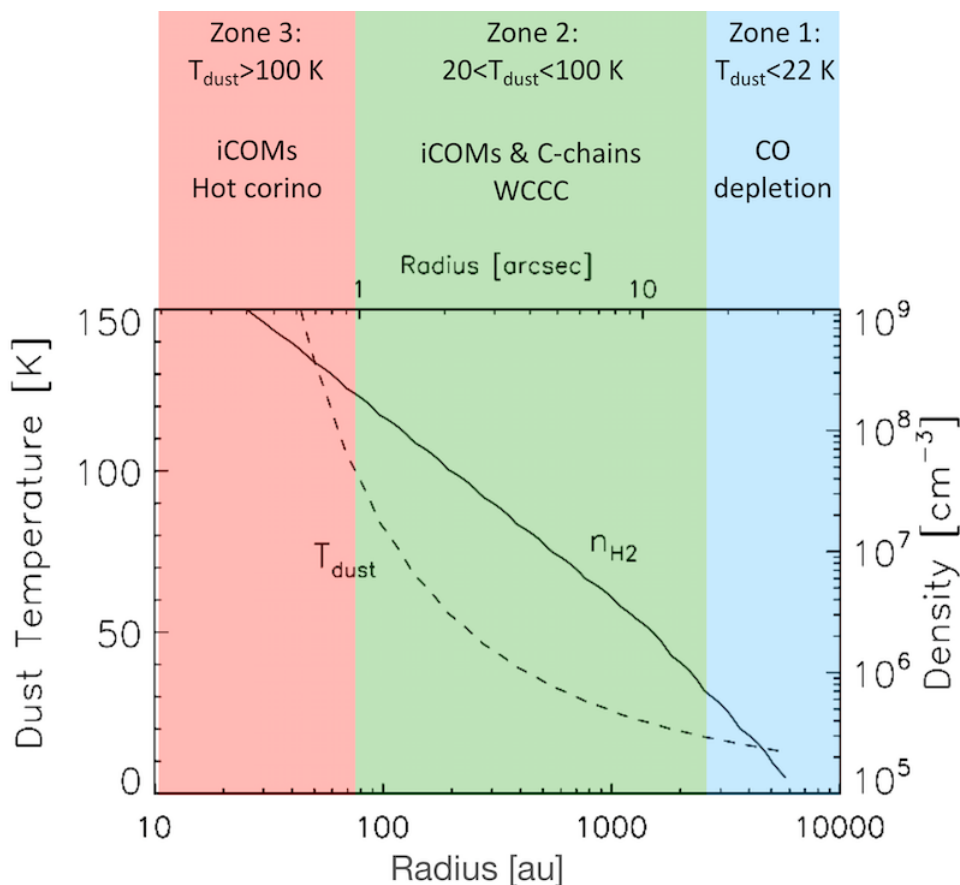


Figure 4: An illustration of a simplified physical and chemical structure of a protostellar core. Reprinted from Ceccarelli et al. (2023), with permission from the editors of PPVII as well as the author.

1. Exterior, cold region of the core with dust temperatures below 22 K. Most molecules, including CO are frozen out onto the dust mantles.
2. Intermediate region with dust temperatures between 22 and 100 K (the desorption temperatures of CO and H<sub>2</sub>O respectively). In this temperature range, methane desorbs into the gas phase and enough of it can produce unsaturated carbon chains. Some sources are observed whose chemistry is dominated by this kind of 'warm carbon chain chemistry (WCCC) (Sakai & Yamamoto, 2013).
3. Interior, hot region of the core with dust temperatures above 100 K. The water in the ice mantle sublimates into the gas phase and releases all the other species trapped within. The release of methanol gives rise to the enrichment of the region with iCOMs. This region has the same properties of the so called "hot cores" in high mass star forming regions, with the difference that it is much smaller in diameter. As such, with the same analogy as hot cores, they were named hot corinos (Ceccarelli, 2004).

In most observed cases of solar-type protostars, their spectra either represents that of a hot corino, or WCCC. However, in recent years sources which include both cases in different scales have been observed (Ceccarelli et al., 2023).

The reality of the physics of a protostellar core is much more complicated than the simplified model I described (see Section 1.1.3). The core collapse is a highly dynamic and non-symmetric and non-linear process. As such one can deduce that the dynamic nature of the protostellar cores should reflect in the chemistry of these objects. This is the subject of the study in this work.

## 2 Methodology I

We saw in Chapter 1 how the physics of the ISM is non-linear and complex. Many different physical processes are acting simultaneously and govern and shape the properties and behavior of the ISM and star formation. To have a theoretical understanding of the observed data, one needs to consider, hydrodynamics, radiative transport, nuclear physics, magnetic fields, etc. Even the chemical composition and reactions in the ISM can affect its dynamics. Furthermore, astrophysics is a multi-scale problem. For example, the impact of gravity (a long range field) and turbulence (a local property of the gas) are comparable. This means that the typical approximations one uses in analytical methods are not necessarily valid in astronomical objects. Therefore, it is needed to take physical processes in a huge length scales into account. From sub-parsec scales to kilo-parsec scales. As a result, one needs to use numerical methods to be able to model such sophisticated system.

On the other hand, unlike many other areas of physics, astronomical objects are experimentally out of our reach. We cannot change the initial condition of any astronomical object to see how it affects its evolution. Computer simulations we utilize to model the ISM can be used as our "laboratories". We can change the mass distribution, the magnetic field, the turbulent seeds, or any other physical parameters of the system and see which configurations can reproduce what we observe in real astronomical objects.

In this chapter, I will discuss the codes and simulations which are used in this work. Since the main part of this project was to combine these different simulation units to develop a method to couple dynamic to chemistry simulations, I assign a separate chapter to the pipeline. Here I go through different units of simulation and introduce the codes and the setup.

### 2.1 (Magneto-)Hydrodynamic Simulations

One can consider the ISM to be a fluid, as the mean free path between the gas particles which build up the ISM is much smaller than the physical length scales involved in the ISM (Shu, 1991). As such one can use fluid dynamics or the equations of hydrodynamics (Euler equations) to describe the evolution of this fluids physical parameters, such as density, velocity and internal energy.

$$\frac{d\rho}{dt} + \rho \nabla \mathbf{v} = 0, \quad \text{Continuity equation;} \quad (6)$$

$$\frac{d\mathbf{v}}{dt} + \frac{\nabla P}{\rho} = 0, \quad \text{Momentum equation;} \quad (7)$$

$$\frac{du}{dt} + \frac{P}{\rho} \nabla \mathbf{v} = 0, \quad \text{Energy equation,} \quad (8)$$

where  $d/dt = \partial/\partial t + \mathbf{v} \nabla$  is the convective derivative. As it was discussed before, the physics of the ISM is highly non-linear and complex, hence one needs to use numerical methods to solve hydrodynamic equation for the ISM. There are different schemes to solve these equations, mainly based on how one discretizes the fluid. For a review on some of these different approaches please see Bodenheimer et al. (2006). Here I describe the smoothed particle hydrodynamics (SPH) method, which is the scheme employed in the hydrodynamic simulations used in this work. followed by the set-up of the said simulations.

### 2.1.1 SPH codes

SPH is a technique to discretize the fluid into elements, the "SPH particles", which are moving with the flow. This technique was independently developed by Lucy (1977) and Gingold and Monaghan (1977) and is based on the Lagrangian description of fluid dynamics, which is a formulation based on co-moving coordinates of a fluid element. SPH's main principle is to use sampling particles to describe hydrodynamics, hence providing a mesh-free prescription. Equations of hydrodynamics are derived in terms of these particles.

Another way of thinking about SPH formulation is to think of it as using local sampling of the mass distribution to calculate the density (Price, 2012). Figure 5 shows an illustration of the SPH approach to calculate the density for each particle, which uses a weighted summation over nearby particles (Neighboring particles).

$$\rho(\mathbf{r}) = \sum_{i=1}^{N_{\text{neig}}} m_i W(\mathbf{r} - \mathbf{r}_i, h), \quad (9)$$

where  $W$  is a weight function, known as smoothing kernel and  $h$  is a length scale, the so called "smoothing length", over which  $W$  drops, defining an effective "radius" for the particle.  $m_i$  is the mass and  $\mathbf{r}$  is the position of each particle and  $N_{\text{neig}}$  is the number of neighbors, or the number of particles which are included in the density summation.

Any other continuous quantity is calculated by:

$$A(\mathbf{r}) = \sum_{i=1}^{N_{\text{neig}}} \frac{m_i}{\rho_i} A_i W(\mathbf{r} - \mathbf{r}_i, h). \quad (10)$$

The smoothing length is set to be proportional to the local number density of the

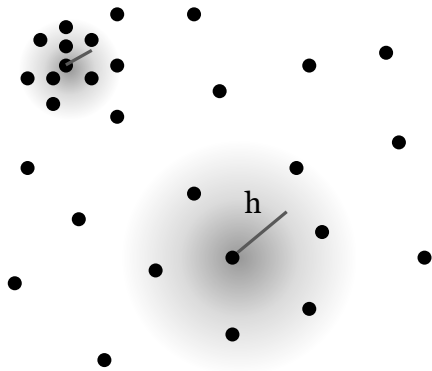


Figure 5: A schematic illustration of SPH approach to calculate density.

particles, and in case of equal mass particles, proportional to the volume density:

$$h(\mathbf{r}) = \eta \left( \frac{m}{\rho} \right)^{1/d}, \quad (11)$$

where  $d$  is the number of dimensions and  $\eta$  is the constant of proportionality. In a typical modern SPH code, Equations 9 and 11 are solved simultaneously. This results in one of the main advantages of SPH schemes. The resolution, represented by the smoothing length, is proportional to the density. This is extremely useful in simulating many astronomical objects, where the density contrast is very high and one wants the resolution to follow the mass.

Another important advantage of SPH is its conservation properties. This formulation conserves mass, linear and angular momentum, energy and entropy simultaneously (Springel, 2010). Conservation of mass in particular, is of interest for this work, as I post-process hydrodynamic simulations with a chemistry code. Chemistry is a local phenomena and the conservation of mass makes the chemistry calculation self-consistent, when they are done for each particle separately.

### 2.1.2 Gravity

One of the biggest sources of dynamics in the ISM is gravity. The ISM fluid is self-gravitating, which causes collapse and star formation. So additional terms should be added to the equation of motion. While hydrodynamic forces are local and one needs to consider only the neighboring particles (see Section 2.1.1), gravity has infinitely large range, hence the gravitational effect of every two pair of particles should be calculated. This, however, is very computationally expensive. Hence one needs some methods of approximation. One such technique, widely and successfully used in modern codes is called a tree (Barnes & Hut, 1986).

The main idea of a gravitational tree is that two objects, which are sufficiently close to one another can be lumped together and approximated as one object. The mass distribution of the material close by has a bigger effect than the ones far away. Hence the criterion of objects being sufficiently close together should involve the distance of these objects as well. A limit on the viewing angle encompasses both the effect of distance between the to-be-grouped objects and between the group and the reference object. First one builds a tree, starting from the entire domain as a cell, called the root cell. The root cell is then divided into two cells, called child cells, in such a way that each cell contains equal numbers of particles. The division of children's cells continues until the number of particles in each cell is less than a pre-set number. The final resulting cells from this procedure are called the leaf cells. After the gravity tree is built, one "walks the tree" to calculate the gravitational force on each particle. In a top to bottom approach, one starts from the first child cells and calculates the opening angle. If it is smaller than a pre-set angle ( $\theta_{max}$ ), i.e.

$$\frac{s}{d} \leq \theta_{max}, \quad (12)$$

all the particles in that cell are considered a point mass whose mass is equal to the total mass of the particles within and the position at the center of mass of those particles. In Equation 12,  $s$  is the cell size and  $d$  is the cell distance. This method reduces the computing time from  $\mathcal{O}(N^2)$  to  $\mathcal{O}(N \log N)$ .

### 2.1.3 Sink particles

Time steps are constructed in SPH codes such that it ensures SPH particles cannot move further than their smoothing length in less than a time step. It ensures that their physical properties would not change too fast. In the ISM simulations, regions of high density can become gravitationally unstable and collapse, which corresponds to a core collapse. The collapsing cores will have increasingly high densities, velocities and accelerations, which leads to increasingly small time steps until the simulation becomes computationally unfeasible. One commonly used solution is to use the so called "sink particles" (Bate, Bonnell, & Price, 1995). A protostar is replaced by one particle, with the mass and linear momentum of all the particles within. The sink particle only interacts gravitationally with the SPH particles and can accrete them.

### 2.1.4 Simulation set up

I use a hydrodynamic simulation of a core collapse performed by Rohde et al. (2021) with the SPH code GANDALF (Hubber et al., 2018). These simulations

use an approximate method of estimating optical depth from local properties of SPH particles, i.e. density, temperature and local pressure gradient and calculate cooling and heating rates (Stamatellos, Whitworth, Bisbas, & Goodwin, 2007; Lombardi, McNally, & Faber, 2015). This method includes the effects of cooling and heating by compression and expansion, viscous dissipation, external irradiation and radiative cooling.

Sink particles (see Section 2.1.3) are used to represent protostars (Hubber, Walch, & Whitworth, 2013). These simulations incorporate an episodic accretion scenario (see Section 1.1.3) based on a model by (Stamatellos et al., 2012). This model assumes a combination of gravitational and magneto-rotational instabilities to be the trigger for the outbursts. These simulations include a subgrid model to follow the proto-stellar evolution. This protostar evolution code is based on stellar evolution model from Offner et al. (2009). This model has been originally developed by Nakano et al. (1995) and later on improved by Nakano et al. (2000) and Tan and McKee (2004). The main idea of this model is to approximate the star with a self-gravitating sphere of gas, for which the rate of contraction is controlled by energy conservation. The evolution of the protostar is followed within distinct phases.

1. Pre-collapse: very low mass phase ( $m \lesssim 0.01M_{\odot}$ ), before the protostar is formed.
2. No burning: the mass is high enough for  $H_2$  dissociation and the second collapse starts and stellar densities are reached.
3. Core deuterium burning at fixed  $T_c$ : Central temperatures reach  $T_c \approx 1.5 \times 10^6$  K, necessary for burning deuterium and remains at this temperature until there is deuterium to burn. The core remains fully convective.
4. Core deuterium burning at variable  $T_c$ : The core temperature rises and the accreted deuterium travels fast to the center and burns. The opacity is reduced due to rising temperature.
5. Shell deuterium burning: The opacity becomes low enough for the convection to stop and radiation takes over and causes the radius to expand. Deuterium still burns in a shell surrounding the radiative core.
6. Main sequence: The temperature reaches  $10^7$  K and, enough for hydrogen fusion. A new star is born. This is the end of this model where the star stabilizes in the main sequence.

The output of this subgrid model is the stellar luminosity,  $L_{\star}$  and stellar radius,  $R_{\star}$  and they are calculated by balancing accretion, gravitational contraction, nuclear

burning, ionization and radiation. The accretion luminosity is proportional to the accretion rate, hence, it follows the same highly non-linear behavior between the outbursts and the quiescent phase. Using both the episodic accretion model and the stellar evolution model, the protostar luminosity is calculated and its effect on the temperature surrounding the core is taken into account by adding a term in temperature.

The hydrodynamic simulations include an episodic outflow model, for which a subgrid model is used. This model assumes that the ejected mass is 10 percent of the accreted mass. The outflow model by Matzner and McKee (1999) is used to calculate the density and velocity distribution of the outflow, resulting in a two-component outflow, a collimated high velocity jet, and a low velocity wide-angle disc wind.

I used one of the 88 simulations performed in Rohde et al. (2021). The initial condition of the simulation consists of a dense core ( $M_{\text{core}} = 1 M_{\odot}$ ), which is embedded in a low-density envelope with a temperature of  $T = 10$  K, the density of  $\rho_{\text{env}} = 10^{-23} \text{ g cm}^{-3}$ , which extends to the radius of  $r_{\text{env}} = 0.75$  pc. The density distribution follows that of a Bonner-Ebert sphere (Bonnor, 1956; Ebert, 1957), with a core radius of  $r_{\text{core}} = 0.013$  pc and a central density of  $\rho_{\text{core}} = 4.8 \times 10^{-17} \text{ g cm}^{-3}$ , with a free-fall time of  $t_{\text{ff}} = 24.6$  kyr. An isotropic random Gaussian velocity field (Walch, Naab, Whitworth, Burkert, & Gritschneider, 2010) is applied to the dense core to produce turbulence. The amplitude of the turbulence follows a power spectrum:

$$P_k \propto k^{-4} \quad \text{with } k \in [1, 64], \quad (13)$$

and its strength is controlled by setting the virial ratio

$$\alpha_{\text{vir}} = \frac{2(E_{\text{turb}} + E_{\text{therm}})}{|E_{\text{grav}}|} = 1. \quad (14)$$

The mass resolution is 400 000 SPH particles per  $M_{\odot}$ . This simulation produces a binary system. Figure 6 shows the column density of the simulation 50 kyr into the simulation. One sees the outflow bullets and outflow cavities. I look at these simulations in Chapter 4. I use this hydrodynamic simulation as the physical model for the chemistry simulation I perform in this work. In Chapter 3 I explain how I use the result of this simulation to find the time evolution of the spatial distribution of methanol.

## 2.2 Chemistry Simulations

As I discuss in Section 1.1.3, proto-stellar cores are nurseries of iCOMs and have rich chemistry. The most common way of modeling the complex chemistry of the

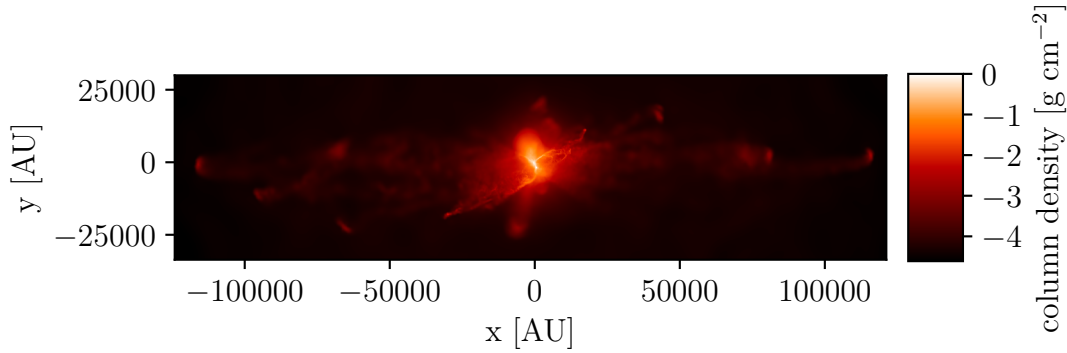
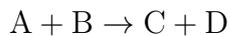


Figure 6: Column density of the hydrodynamic simulation of a core collapse by Rohde et al. (2021) at  $t = 50.0$  kyr. This is the simulation I use in this work.

ISM is to use a rate equation. In this section I present this method and how it is used to understand the chemistry of proto-stellar cores. Then I discuss the chemistry code, Saptarsy, used in this work.

### 2.2.1 Reaction rates and chemical network

Assuming a binary reaction like in Equation 3,



one can calculate the rate of this equation as a function of the number density of these species. If there is no mass exchange from the system where this reaction takes place, the reaction rate should be proportional to the amount of reactant species available. The number density of A and B will decrease in time as the number density of C and D will increase. Using  $[X]$  as the number density of a molecule X (called the abundance of X), the change in [A] should be equal to the change in B in the same period of time. Combining everything together the rate equation is

$$\frac{d[A]}{dt} = \frac{d[B]}{dt} = -\frac{d[C]}{dt} = -\frac{d[D]}{dt} = -k[A][B], \quad (15)$$

where the proportionality coefficient  $k$  is called the reaction rate coefficient and has the units of  $[\text{cm}^3\text{s}^{-1}]$ . Rate coefficients are typically a function of temperature and are measured in laboratories. One can find different relationships for the rate coefficient for different types of chemical reactions (see Tielens (2005); Yamamoto (2017)). However, there is a generalized way one can use to describe the rate coefficients. Svante Arrhenius (Arrhenius, 1889) proposed a formulation for the temperature dependency of reversible reactions

$$k(T) = \alpha \exp\left(-\frac{\gamma}{T}\right), \quad (16)$$

where  $\gamma$  is the barrier energy, which needs to be overcome for the reaction to proceed.

Since the reaction rate is a function of the collision rate (Tielens, 2005; Yamamoto, 2017), one can deduce that the rate coefficient is a function of temperature. Hence modifications were proposed on Arrhenius equation to take the temperature dependency into account (Canosa et al., 1997; Smith et al., 2006). The general form of a modified Arrhenius equation is

$$k(T) = \alpha \left( \frac{T}{300\text{K}} \right)^\beta \exp \left( -\frac{\gamma}{T} \right). \quad (17)$$

Values for  $\alpha$ ,  $\beta$  and  $\gamma$  are deduced by measuring reaction rates for different temperatures. There are different data bases which gather the latest measurements of these constants for different gas-grain reactions in the ISM, such as UMIST database for astrochemistry (McElroy et al., 2013)<sup>1</sup> and KIDA (Wakelam et al., 2012),<sup>2</sup>.

One can build a network of chemical reactions, having these databases at hand and numerically solve the coupled differential equations to calculate the time evolution of the abundances of different species. This approach to modeling chemistry has been attempted since the 70s (Allen & Robinson, 1977; Tielens & Hagen, 1982; Hasegawa et al., 1992). The early models had the drawback that the discrete nature of the dust was not taken into account. In the cases of very small dust grains, H atoms are highly mobile, due to quantum tunneling (see Section 1.2.2). So much so that the timescale for atomic hydrogen to scan the dust and react with another molecule can become smaller than the timescale of accretion of another Hydrogen atom and the reaction rate method overestimate these reactions. Later models include modifications on the rate equation method to treat this issue (Caselli et al., 1998, 2002; Garrod, 2008). The former modifies the sweeping rate of H for dust grains at 10K and the latter limits the reaction rates by the accretion rates when the abundance of reactants are very low.

One other drawback of reaction rate chemistry codes is the uncertainty of the rate coefficients (van Dishoeck, 2018). These uncertainties can propagate in the network and cause errors in the calculated abundances. Wakelam et al. (2010) shows that even for simple molecules like H<sub>2</sub>O, SO or CH, the resulting uncertainty in abundance is at a factor of  $\sim 3$ .

Despite all these drawbacks, reaction rate simulations are cost efficient and are able to reproduce acceptable results. I use a reaction rate code, Saptarsy, to model the chemistry of a core collapse in this work. In the next section I discuss

<sup>1</sup><http://udfa.ajmarkwick.net>

<sup>2</sup><https://kida.astrochem-tools.org/>

this code and the simulation setup I used for this thesis.

### 2.2.2 Saptarsy and Simulation set up

Saptarsy is a rate equation based gas-grain chemistry code to calculate the effects of spatio-temporal variation of physical parameters on the chemistry. It was developed by Choudhury et al. (2015) based on Astrochem code by Bergin et al. (1995) with major modifications. The code can deal with gas phase reactions, gas-grain interactions and dust surface reactions. Stéphan et al. (2018) added a spline interpolation and a multi-layered dust model was implemented later by Schaefer (2017).

The code solves the reaction rate equations, using the Netlib library solver, DVODPK<sup>3</sup> for solving the ordinary differential equations and Harwell Mathematical Software Library advance solver MA28<sup>4</sup> for solving sparse systems of linear equations. Gas phase and dust surface interact through accretion and desorption. The gas and dust surface reactions are implemented based on the networks of (Hasegawa et al., 1992; Hasegawa & Herbst, 1993).

The modified Arrhenius equation (Equation 16) is used for calculating the reaction rate of the two body chemical reactions and the reactions with 3 or more reactants are not included. There are however other types of reactions which are involved and implemented in Saptarsy (Garrod, 2008), whose reaction rate is calculated differently. These reactions are listed in tables 1, 2 and 3 for gas phase reactions, dust surface reactions and gas-grain interactions respectively.

In the cold cores, as molecules freeze out onto the dust, they fill up all the sites on the dust surface. However, the accretion of different chemical species does not stop and they continue freezing out on top of the previously absorbed species. The buried species become non-reactive. Hence a three-phase model, including a gas phase, a surface phase and a mantle phase is a more realistic way of describing the dust chemistry and its interactions with the gas phase. Schaefer (2017) implemented a multi-layered dust model into Saptarsy. The model keeps track of a so called occupation fraction, defined as

$$\Omega_t = \frac{N_{\text{species}}^s(t)}{N_{\text{sites}}^s}, \quad (18)$$

where  $N_{\text{species}}^s$  and  $N_{\text{sites}}^s$  are the number of species on the dust and number of sites. When  $\Omega_t \geq 1$ , a layer is filled and a new layer is built. In order to prevent the number of active species to drop to zero every time a new layer starts, the surface is divided into segments and the occupation factor is calculated for each

---

<sup>3</sup><https://www.netlib.org/ode/>

<sup>4</sup><https://www.hsl.rl.ac.uk/>

<b>Gas phase reactions</b>	
Neutral - neutral	$A + B \rightarrow C + D$
Neutral - neutral	$A + B \rightarrow C^+ + e$
Ion - neutral	$A^{+/-} + B \rightarrow C^{+/-} + D$
Charge exchange	$A^{+/-} + B \rightarrow A + B^{+/-}$
Cation - Anion recombination	$A^{+/-} + B^{-/+} \rightarrow A + B$
Radiative recombination	$A^+ + e \rightarrow A + h\nu$
Electron attachment	$A + e \rightarrow A^- + h\nu$
Radiative association	$A + B \rightarrow AB + h\nu$
Radiative association	$A^+ + B \rightarrow AB^+ + h\nu$
Associative detachment	$A^- + B \rightarrow AB + e$
Dissociative recombination	$A^+ + e \rightarrow C + D$
Collisional dissociation	$AB + C \rightarrow A + B + C$
Photo-ionization	$A + h\nu \rightarrow A^+ + e$
Photo-dissociation	$AB + h\nu \rightarrow A + B$
Cosmic-Ray ionization	$A + CR \rightarrow A^+ + e$
Cosmic-Ray dissociation	$AB + CR \rightarrow A + B$

Table 1: List of gas phase reactions included in Saptarsy.

<b>Dust surface reaction</b>	
Grain-surface chemical reactions	$s-A + s-B \rightarrow s-AB$
Photodissociation by cosmic rays	$s-AB \rightarrow s-A + s-B$
Photodissociation by background photons	$s-AB \rightarrow s-A + s-B$

Table 2: List of dust phase reactions included in Saptarsy.

<b>Gas-grain interactions</b>	
Gas-grain interaction	$A + G^- \rightarrow A^-G$
Electron-grain recombination	$A^- + G \rightarrow A + G^-$
Surface accretion	$A \rightarrow s-A$
Cosmic Ray induced general desorption	$s-A + CR \rightarrow A$
Photo-desorption	$s-A + h\nu \rightarrow A$
Thermal desorption	$s-A \rightarrow A$
Reactive desorption	$s-A + s-B \rightarrow AB$

Table 3: List of gas grain interactions included in Saptarsy.

of them. The number of sites increases layer by layer to take the growth of surface area by increasing radius into account. The reverse is done when the temperature rises and the species on the dust start to desorb into the gas phase and the dust loses its accumulated layers of molecules.

The chemical network I use in this work is a reduced gas-grain network with 185 species from Garrod (2008), to which new reactions for HCN and HNC (Graninger et al., 2014; Loison et al., 2014) were added as well as CH<sub>3</sub>O in both gas and dust. Moreover, the desorption energies were updated based on KIDA. This is the smallest possible network, which would produce the smallest and arguably one of the most important iCOMS, methanol. We chose to not use a bigger network, as even this one has over 2500 reactions and even bigger networks are not feasible.

As initial conditions for the simulations, I use the elemental abundances EA2, from Wakelam and Herbst (2008), which is based on observations in  $\zeta$  Ophiuchi cloud and is modified based on Orion observations (Baldwin et al., 1991; Osterbrock, Tran, & Veilleux, 1992). For dust grain properties, the parameters from Semenov et al. (2010) is implemented. Dust grains are assumed to be spherical carbonaceous particles with a radius of  $r_d = 0.1 \mu\text{m}$ , a density of  $\rho_d = 3 \text{ g cm}^{-3}$ , a dust to gas mass ratio of 0.01 and a surface density of sites of  $\Sigma_{\text{site}} = 1.5 \times 10^{15} \text{ cm}^{-2}$ . I use the binding to desorption energy of  $\frac{E_b}{E_D} = 0.3$  according to (Hasegawa et al., 1992). The cosmic ionization rate is adopted as  $\zeta_{CR} = 1.3 \times 10^{-17} \text{ s}^{-1}$  (Semenov et al., 2010). I use the same multi-layer dust parameters as Schaefer (2017), i.e.  $N_{\text{segment}} = 4$ .

I explain how I couple the physical model presented in Section 2.1.4 to the chemical model I described here in Chapter 3.

## 2.3 RADMC-3D

As a protostar forms, collapses and starts radiating (see Section 1.1.3), it heats up the dust via radiation. This thermal heating is a key component in releasing the buried species in the dust mantle and as such a correct estimation of dust temperature has a key role in controlling chemistry. To calculate the dust temperature via radiative heating, one needs to solve radiative transfer equations for the rays coming from the radiation source. Since the hydrodynamic simulations I use for this work do not include radiative transfer (see Section 2.1.4), I use RADMC-3D code (Dullemond et al., 2012) to calculate the dust temperature.

RADMC-3D is a code to calculate radiative transfer for astrophysical purposes. Among other capabilities, it can calculate dust temperature using a Monte Carlo method. It uses an adaptive mesh refinement grid (AMR grid) as an in-

put for density. It takes one or multiple sources of luminosity, divides the total luminosity of the sources by the number of photons, which is a parameter set by the user and finally emits the photon packages one by one in random directions. When a photon package encounters a dust grain, two things can happen. It either scatters off the dust, i.e. changes its direction, or it gets absorbed and re-emitted at another wavelength in another direction and increases the temperature of the cell (Bjorkman & Wood, 2001). The photon package continues bounding off the dust grains until it leaves the domain.

In my physical model, the dense core is a highly embedded source and is optically thick. This causes the Monte Carlo simulations to become very slow, as the photon package can collide with too many dust grains in a very dense region and 'get lost' in the dense core. To solve this issue, RADMC-3D has the ability to use the modified random walk (MRW) method (Fleck & Canfield, 1984; Min, Dullemond, Dominik, de Koter, & Hovenier, 2009; Robitaille, 2010). MRW method solves a diffusion equation with a constant density for one cell analytically, which in a highly optically thick cell, is equivalent to hundreds of absorption events, thus reduces the computational time considerably. Moreover, the thermal Monte Carlo simulation is parallelized with OpenMP, which I make use of in this work.

I produce the AMR grid, the density distribution and the necessary information about the protostars as sources of luminosity out of the hydrodynamic simulations. I explain how this is done in Chapter 3. The other inputs of the simulations are related to dust properties. I use one dust species, namely the silicate grain. How dust grains change the wavelength and the direction of the photons, through scattering and absorption/re-emission processes, is generally a function of wavelength and also depends on the depleted molecules on the surface of the dust grains, which can change the grain's optical properties. I use the model by Ossenkopf and Henning (1994), who have calculated the dust opacity in dense protostellar cores between 1  $\mu\text{m}$  and 1.3 mm. I use a black body spectra for the protostars.

In the next chapter, I discuss how I use the output from the hydrodynamic simulations for RADMC-3D simulations and how I use the resulting output as input for the chemistry simulations with Saptarsy.

### 3 Methodology II: Coupling dynamics to chemistry

The main goal of this work is to couple dynamics to the chemistry by post processing the hydrodynamic simulations with the chemistry code, Saptarsy. For this work, I chose to use SPH simulations of a core collapse. As it is discussed in Section 2.1, one of the advantages of SPH scheme is its conservation properties. SPH particles are Lagrangian fluid elements, hence they are mass conserved. In addition chemistry is a local process. The lack of mass exchange between the SPH particles, means that I can avoid dealing with fluxes while modeling chemistry. The central framework of this work is to sample the gas by sampling the SPH particles. Then following these particles throughout the simulations, tracking their physical properties and finally running each particle as a separate simulation with Saptarsy, i.e. treating each particle as an independent physical model for the chemistry.

Initially I worked on a simple, proof-of-concept model (test model from here on forward). After the pipeline was worked out, I improve on different aspects of the model and run a bigger, more comprehensive model (final model from here on forward). In this chapter I explain different steps of the pipeline, starting from hydrodynamic simulations and ending with chemistry simulations. For each step, I introduce the test model set up and the final model set up.

#### 3.1 Sampling the gas

The region of interest for chemistry are inner parts of the core, where not most species are frozen out on the dust, therefore the sampled particles should spend considerable amount of time in the inner region of the core. To this end, I first select all the particles which end up in the inner 15 000 AU of the center of the simulation box at the end of the time interval of analysis (62.6 kyr into the hydrodynamic simulation) and randomly pick 10 percent of those particles, which amount to 22867 particles. Having sampled the gas, in every snapshot between the 37.8 and 62.6 kyr (duration of 24.8 kyr), I track the sampled particles and record their physical properties, i.e. positions, velocities and densities along their trajectory throughout the simulation. These became the input of the next steps in the pipeline. I explain the choice of this specific time interval in the Section 3.2.3.

For the final model, I improve on the sampling process. I make corrections for the center. Instead of taking the center of the simulation box, I take the middle point between the two sink particles, since they move as they revolve around

their center of mass. I change the sampling method to a mass weighed selection. I make 16 logarithmically-spaced radial bins between 250 AU and 10 000 AU and I randomly pick 1000 particles from each bin. I am not interested in disk chemistry for this work and as such the lower limit was chosen to stay outside of the disk (see Section 4.2 and Figures 24 and 26). Test model show that the chemistry does not change after 10 000 AU, hence the upper limit was chosen as such. In bins with with less than 1000 particles, I select all the particles. In order to keep the statistic consistent with time evolution, I sample from the first snapshot and check every 50 snapshots (once every 10 kyr) whether there are still 1000 particles in every bin. If the condition is not met, I select further particles until either all the particles in that bin are picked or the 1000 particles limit is reached. I also extended the time interval to 700 snapshot, i.e. the duration of 140 kyr, up to 177.8 Kyr into the hydrodynamic simulation.

### 3.2 Calculating the dust temperature

The GANDALF simulations I use do not include radiative transfer. Therefore, the dust temperature caused by radiation from the protostars are not accurately calculated (see Section 3.2.3). But the dust temperature plays a key role in starting the chemistry by releasing the buried molecules onto the gas phase. To solve this issue, I use the radiative transfer code RADMC3D to calculated dust temperature. RADMC-3D uses an adaptive mesh refinement(AMR) grid as input, so I first need to map the SPH particles into and AMR grid. I discuss this step in Section 3.2.1. I perform a test to investigate the temperature difference for the test model. Figure 7 shows the difference between the temperatures from the hydrodynamic simulations with GANDALF and the dust temperatures calculated with RADMC-3D versus the distance of each SPH particle from the center of the simulation box for a snapshot at the end of the time interval(at 62.6 kyr). There is a significant difference between the two, especially in larger radii, as such calculating the dust temperature with RADMC3D improves on the modeling in a significant way.

The hydrodynamic simulations are of a small core, with the total mass of  $1 M_{\odot}$  and it fragments into a binary system, which gives rise to very low mass stars( $0.37$  and  $0.36 M_{\odot}$ ). The luminosity of such low mass protostars is not enough to heat up the dust and causing thermal desorption. Since I am interested in investigating chemistry, I amplify the luminosity artificially to compensate. This step, its scope of validity and its ramifications will be discussed in Section 3.2.2. Finally the RADMC-3D simulations will be discussed in Section 3.2.3.

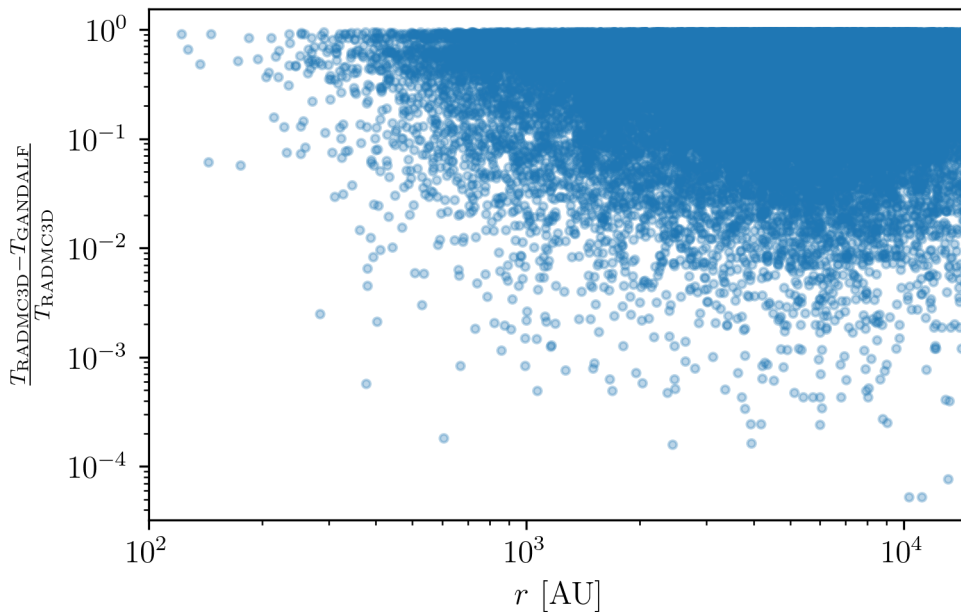


Figure 7: The relative difference between the temperatures from Hydrodynamic GANDALF simulations and the dust temperatures calculated by RADMC3D versus the distance of the particles from the center for the test case.

### 3.2.1 Griding up the particles

To map the SPH particles to an AMR grid, one needs to take the kernel of the smoothing length of particles into account to calculate the physical properties like densities in each cell. To perform these calculations we used the code SPHtool<sup>5</sup> (link to the git repository) and used the regridding function of the code. The code has been developed by Attila Juhasz. It builds an octree based on user defined parameters, in a two-step refinement method, finds all the particles within  $2h$  distance from the center of each cell and uses a cubic spline kernel to calculate the desired variables in the center of the cell.

To build the octree, first step is to build the tree based on the maximum number of particles per AMR grid cell, given by the user and the maximum grid depth, i.e., until one of the both criteria is reached. To set the size of the root cell for the test model, I calculate the 10 percent of maximum and minimum of each Cartesian coordinates and pick the largest one among them. I initially choose 300 particles and level 2 for the maximum number of particles per AMR grid and the maximum grid depth respectively. On the next step, density variation is measured within each cell by randomly choosing a user defined number of points and calculating  $(\max \rho_i - \min \rho_i) / \max \rho_i$ . If this quantity is higher than

<sup>5</sup>[https://bitbucket.org/at\\_juhasz/sphtool/src/master/](https://bitbucket.org/at_juhasz/sphtool/src/master/)

a threshold, the cell is refined further, either until this criteria is met or the maximum refinement level is reached. In the test case I set the number of trial points to be 300, the density variation threshold to be 0.5 and the maximum refinement level to be level 10. The resulting maximum grid resolution varies between 15 and 17 AU for this time interval. The variation is due to the fact that I set the box size based on the furthest particles and this varies with time.

I changed the parameters for the final model as follows. I start from a box with the size being much larger than the diameter of the region of interest, i.e., 50 000 AU, as to prevent edge effects in RADMC3D. I keep the maximum number of particles per grid cell to remain 300 particles, since it was found to be robust by the author. I increase the maximum grid depth to level 8, because building the AMR grid takes considerably less time than the density refinement step. I decreased the number of trial points to 50. This decreases the run time significantly, which allowed me to increase the maximum refinement level to level 12. I keep the same density variation threshold. These parameters result in the maximum grid resolution of 12 AU.

I use SPHtool to produce both the AMR grid and calculate the densities within each cell in the input format of RADMC-3D. I run the code on every snapshot and use the output files in the next steps as inputs for the code RADMC-3D.

### 3.2.2 Amplifying the luminosity

As it is discussed before, in order to produce enough heating for an active chemistry, I amplify the luminosity. The relationship between Temperature and the Luminosity of a black body is described with

$$L = \sigma AT^4, \quad (19)$$

where  $L$  is luminosity,  $A$  is the surface area of the emitting object,  $T$  is the temperature and  $\sigma$  is the Stefan–Boltzmann constant.

I test different factors, starting with raising the surface temperature by a factor of 2, and 3, resulting in increasing the luminosity by the factor of 16 and 81. I run RADMC3D simulations on a non-outburst snapshot (at 62.6 Kyr) and checked the size of the region where the temperature was raised above 100 K. Without any amplification, only 3 cells have temperatures above 100 K. Amplifying the luminosity by a factor of 16 results in a region about 200 AU with temperatures above 100 K and a couple of cells with temperatures above 200 K around each sink particle. Increasing the luminosity by a factor of 81 caused a region of the size of 470 AU and 200 AU with temperatures above 100 K and 200 K respectively. Therefore, increasing the luminosity by the factor of 81 produces enough heating,

so that we do not need to go into higher luminosities.

Raising the luminosity of a star is equivalent to increasing its mass. But the relationship between the mass and luminosity of protostars is not linear. To investigate the effective equivalent mass increase, I run the star formation model, which is implemented in GANDALF, as an independent unit and change the mass accretion rates to probe the behavior of the mass and the luminosity of the protostar. This star formation model is explained in Section 2.1.4.

The only variable parameter in the model is the mass accretion rate and I vary it with the following values:  $10^{-7}$ ,  $10^{-6}$ ,  $10^{-5}$  and  $10^{-4} M_{\odot} \text{ yr}^{-1}$ . In Figure 8 the total luminosity versus stellar mass of the different models is shown. The lines end when the protostar enters the main sequence. The total mass at the end of each line corresponds to the mass of the final main sequence star. It is overlaid with the values from the simulations for the two protostars forming in the HD simulations.

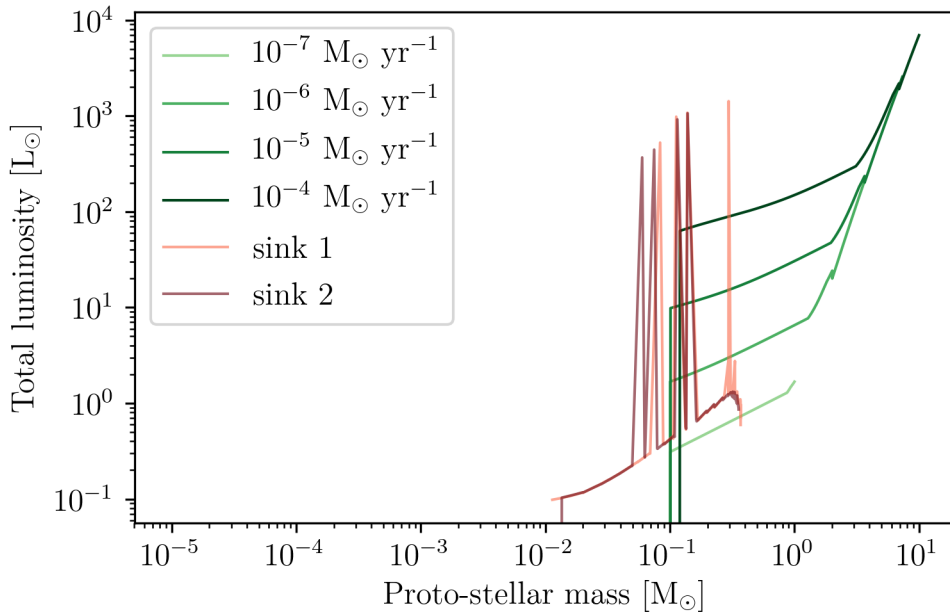


Figure 8: Total mass versus total luminosity of the protostars from proto-stellar evolution model for different accretion rates. Over plotted are the sink particles from the HD GANDALF simulations

It is note-worthy that the protostar evolution models we are running are continues accretion scenario and the accretion rate is constant throughout the simulation, while in hydrodynamic simulations the model is coupled to the accretion rate coming from the episodic accretion scenario, therefore producing the spikes in luminosity which correspond to accretion events.

Increasing the luminosity by a factor of 81 is equivalent to moving the simulation data points vertically upward. Doing so, the simulation data falls between the models with  $10^{-6} M_{\odot} \text{ yr}^{-1}$  and  $10^{-5} M_{\odot} \text{ yr}^{-1}$ . These two models enter the main sequence with 3.6 and 7.4  $M_{\odot}$ . So the model still lies within intermediate mass regime. In future works, a physical model with a higher initial core mass should be employed to achieve a self-consistent model.

### 3.2.3 RADMC-3D Monte Carlo calculation

I use the radiative transfer code RADMC-3D to calculate dust temperature. For that we use the thermal Monte Carlo computation. The method is explained in Section 2.3. protostars are the sources of luminosity, hence, The inputs of the RADMC-3D for the stars as luminosity sources are the radius, mass, temperature and the position of the stars. All of which are calculated in the subgrid protostar evolution model in GANDALF simulations.

I perform a resolution test to choose the number of photons for the dust temperature simulations. I run RADMC-3D Monte Carlo simulations for one snapshot and vary the number of photons as  $10^7$ ,  $10^8$  and  $10^9$  photon packages. Figure 9 shows the histogram of the temperature distribution. While there is major difference between runs with  $10^7$  and  $10^8$  photon packages, the difference between  $10^8$  and  $10^9$  photon packages are small and mostly in very low temperatures below 3 K (Figure 10). Since the core temperature is set to be 10 K in the hydrodynamic simulations and the temperature cannot drop below that, a lower limit of 10 K is set, i.e, the temperature of all particles with  $T < 10$  K is raised to 10 K. Hence, that difference is unimportant to this work's analysis. Therefore, I set the number of photon packages to  $10^8$ .

Having the AMR grid and the density structure calculated with SPHtool in Section 3.2.1, all the ingredients are available to calculate the dust temperature. I use the modified random walk switch in RADMC-3D, since the core is highly embedded and optical depth is high. This slows down the Monte Carlo calculations considerably (see Section 2.3). I perform RADMC3D thermal dust temperature calculation for every snapshot. The simulation time systematically takes longer in the earlier snapshots with respect to the later ones. As the material accretes into the protostars, the optical depth decreases and the photons scatter less, hence the computation time decreases. I run these simulations on the cluster ODIN. ODIN has a time limit for maximum 5 days for each job submission. RADMC-3D does not provide restart files and if the simulation is stopped one has to start from the beginning. In my test model, I started the simulations from where the first sink particle appears, i.e. 13.6 kyr into the simulation. But among the first 24.2 kyr, many of the RADMC-3D runs did not finish on ODIN. The first snapshot after

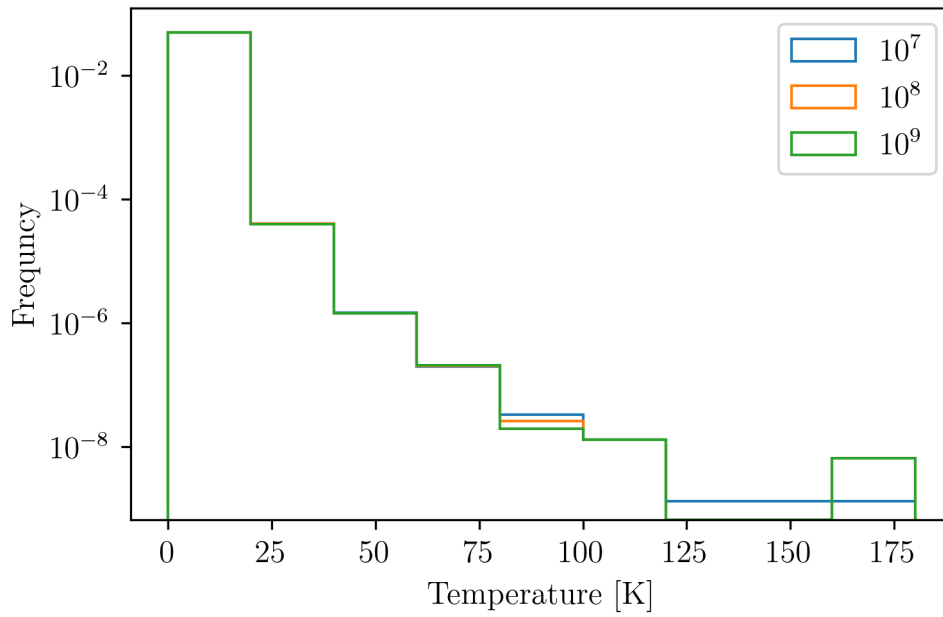


Figure 9: Histogram of temperature distribution for resolution tests of RADMC-3D with  $10^7$ ,  $10^8$  and  $10^9$  photon packages

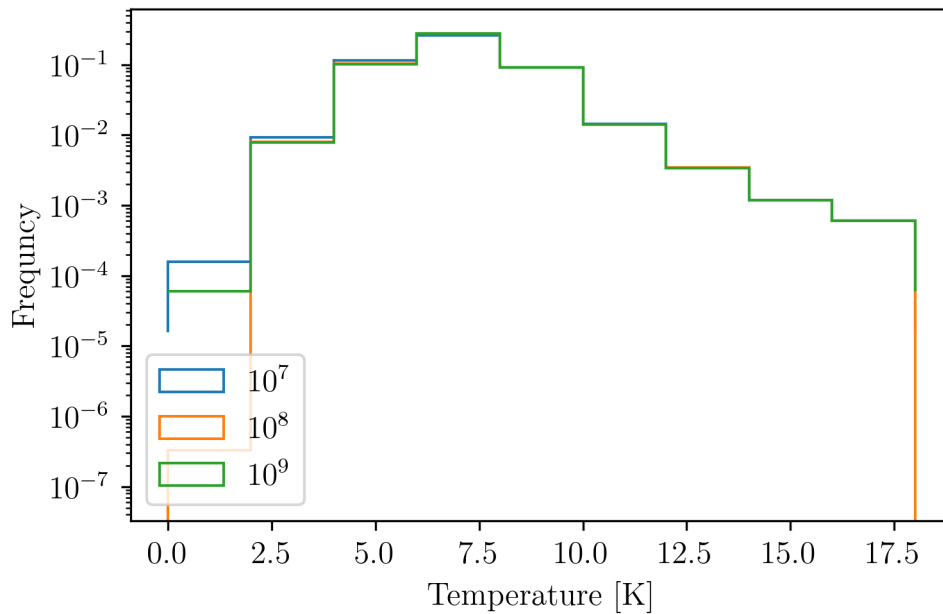


Figure 10: Zoomed-in histogram of temperature distribution for resolution tests of RADMC-3D with  $10^7$ ,  $10^8$  and  $10^9$  photon packages

which all the simulations ended within the running time of ODIN was at 37.8 kyr into the simulations. Hence this became the beginning of the time interval.

For the Final model, increasing the maximum refinement level from 10 to 12 means that we have more cells. So the average number of scattering per photon increased in this model, resulting in longer simulation time. A couple of simulations did not finish on ODIN within the run time limit and dust temperature calculations for these snapshots had to be performed on another cluster (ninurta).

Two specific snapshots, the ones corresponding to the first two accretion events, took too long. Such that after a week only 10 percent of the simulation was done. I decreased the refinement level in building the grid with SPHtool by 1. To investigate the effects of lower refinement I perform a resolution test for the neighboring snapshots. I run the same RADMC3D setup and only vary the maximum refinement level in producing the AMR grid. The result is shown in Figure 11.

Note that the Figure 11 is made after remapping the temperatures back on the SPH particles, which is the next step in the pipeline. The figure is a histogram of temperature distribution. By visual inspection, the difference between the two grid seems to be small, but to be thorough, I plot the relative difference between the number of the particles in different temperature bins (Figure 12). Here I calculate  $(n(T_{12}) - n(T_{11})) / n(T_{12})$ , where  $n(T_{11})$  and  $n(T_{12})$  are the number of particles in each temperature bins from the simulations with 11 and 12 refinement level respectively.

The relative difference between the two grid in temperatures below 100 Kelvin is under 5 percent and overall, it is lower than 30 percent. The relative difference rises with temperature, because there are less particles in high temperature region closer to the protostars, resulting in less number statistics in higher temperature bins (see Figure 11).

The next step is to map the calculated dust temperatures back onto the SPH particles. RADMC3D has a special function for calculating various quantities at any given point. I use this sampling function to map the dust temperature back to the SPH particles. At this point the dust temperature is calculated for every SPH particle and for every snapshot. This is used in the next step of the pipeline in chemistry simulations.

### 3.3 Chemistry simulations

All the ingredients for Saptarsy simulations are ready at this stage. For each particle out of the sampled 70 000 K particles, I have the density evolution from the hydrodynamic GANDALF simulations and the temperatures from the RADMC3D

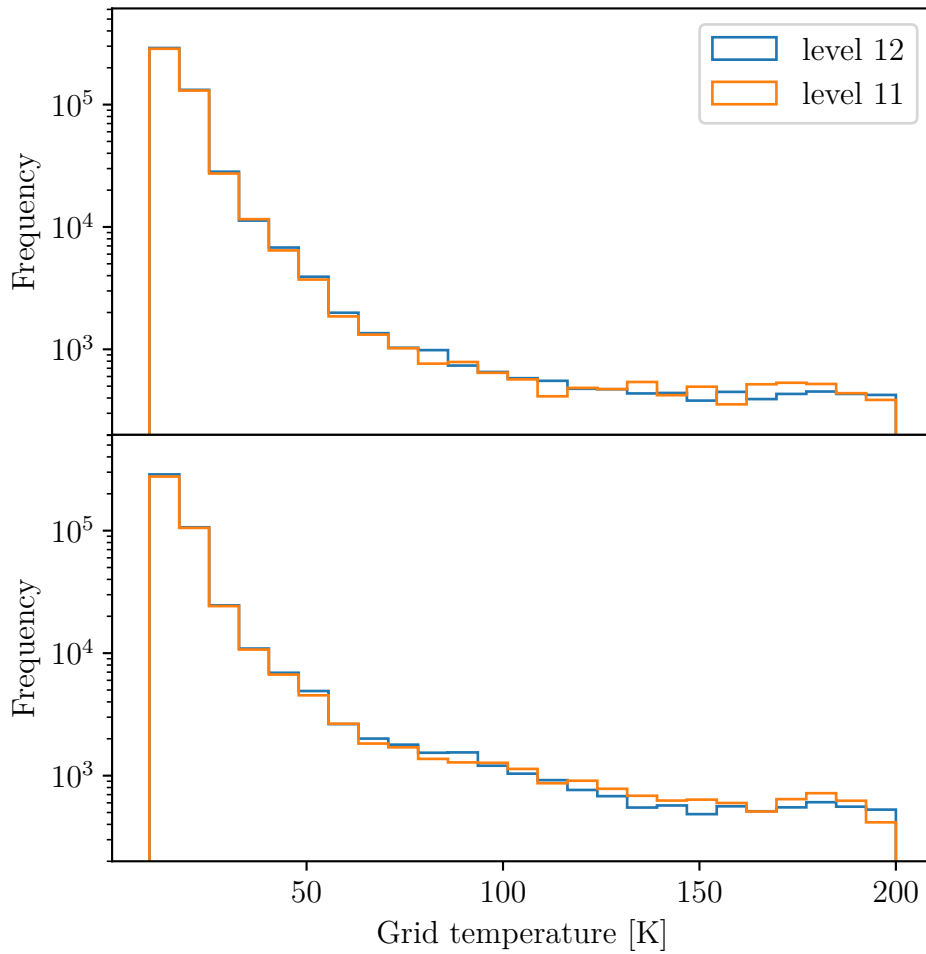


Figure 11: Grid resolution test for (top) the snapshot right after the first flare at 45.6 kyr and (bottom) the snapshot right after the second flare at 59.6 kyr into the simulation

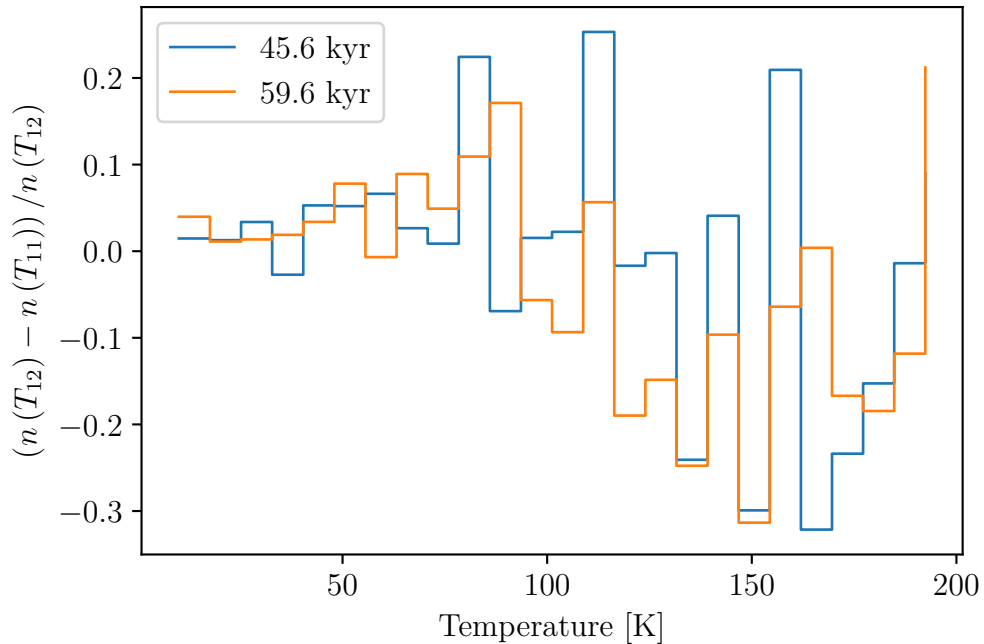


Figure 12: Relative difference between the number of particles of the two grids in different refinement levels, in each temperature bin for the snapshot right after the first flare at 45.6 kyr and the snapshot right after the second flare at 59.6 kyr into the simulation

simulations. Saptarsy also takes visual extinction as input. Unfortunately our hydrodynamic simulations do not include radiative transfer, hence this information is not available through the physical model. Since the subject of this study is in the highly embedded phase of collapse, I assume  $A_v = 1$  everywhere.

I run Saptarsy for each particle separately. The output is the time evolution of the abundances of species present in the network in gas and dust phase. In the next chapter I discuss these results and their implications.

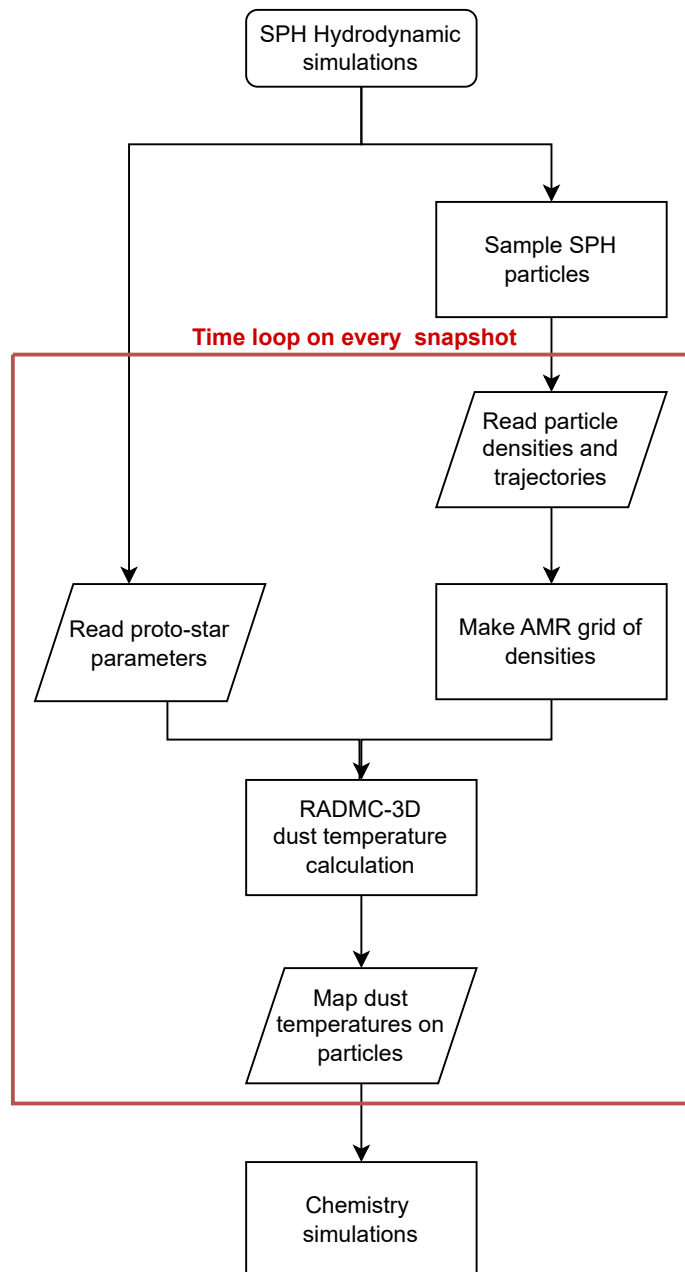


Figure 13: A flowchart of the pipeline of simulations, starting from hydrodynamic simulation as the physical model to the chemistry simulations.

## 4 Results and discussion

In this chapter, I will discuss the results from the chemistry simulations, which are the last steps of the pipeline I described in Chapter 3. I utilize different analysis methods to look at the behavior of chemistry and how it is coupled with the physics of our simulated collapsing core.

I run chemistry code Saptarsy for each particle. Figure 14 depicts the input and output of one example particle. The top panel shows the trajectory of this particle as during the simulation as it is accreted and finally falls into one of the protostars. The middle panel shows the input, which are temperature and density of the SPH particle along its trajectory and the bottom panel is the output, which is the time evolution of the abundances of some examples of different species in gas and dust. Abundance is calculated as  $n_X/n_H$ , where  $n_X$  is the number density of the species and  $n_H$  is the number density of the total hydrogen content:

$$n_H = n_{\text{H}_{\text{atomic}}} + 2n_{\text{H}_2} + n_{\text{H}^+}, \quad (20)$$

where  $n_{\text{H}_{\text{atomic}}}$ ,  $n_{\text{H}_2}$  and  $n_{\text{H}^+}$  are the number densities of atomic hydrogen, molecular hydrogen and ionized hydrogen, respectively.

On a close inspection of Figure 14, one can see spike-like features in the temperature of the particle (middle panel). We zoom in these features in Figure 15 to have a better look. As it was mentioned in Section 2.1.4, our hydrodynamics simulations incorporate the episodic accretion scenario, where during the short-lived accretion events, accretion heating heats up the surrounding material and produces a peak in temperature. The temperature spikes in Figure 15 are then caused by such accretion events. We can also see that these temperature spikes affect the chemistry. The resulting behavior of the abundances of different chemical species is complex. They undergo abrupt changes, but how much they change and how long does it take them to retain their previous state varies from species to species. While methanol has a very sharp jump of 4 orders of magnitude and decreases slowly afterwards, hydrogen cyanide seems to have a fast, yet less abrupt increase and stays on the same level. Sulfur monoxide on the other hand, increases by an order of magnitude and drops to its previous values very fast.

I will investigate the effect of episodic accretion on the chemistry in more detail in the following sections.

I have a set of 70 000 particles, therefore 70 000 simulations. Figure 16 shows a subset of the trajectories, temperatures and densities of these particles. The trajectories vary from quasi rotational in-falling material in various orbits to entrained material, which are being dragged outward by the outflow. This diversity

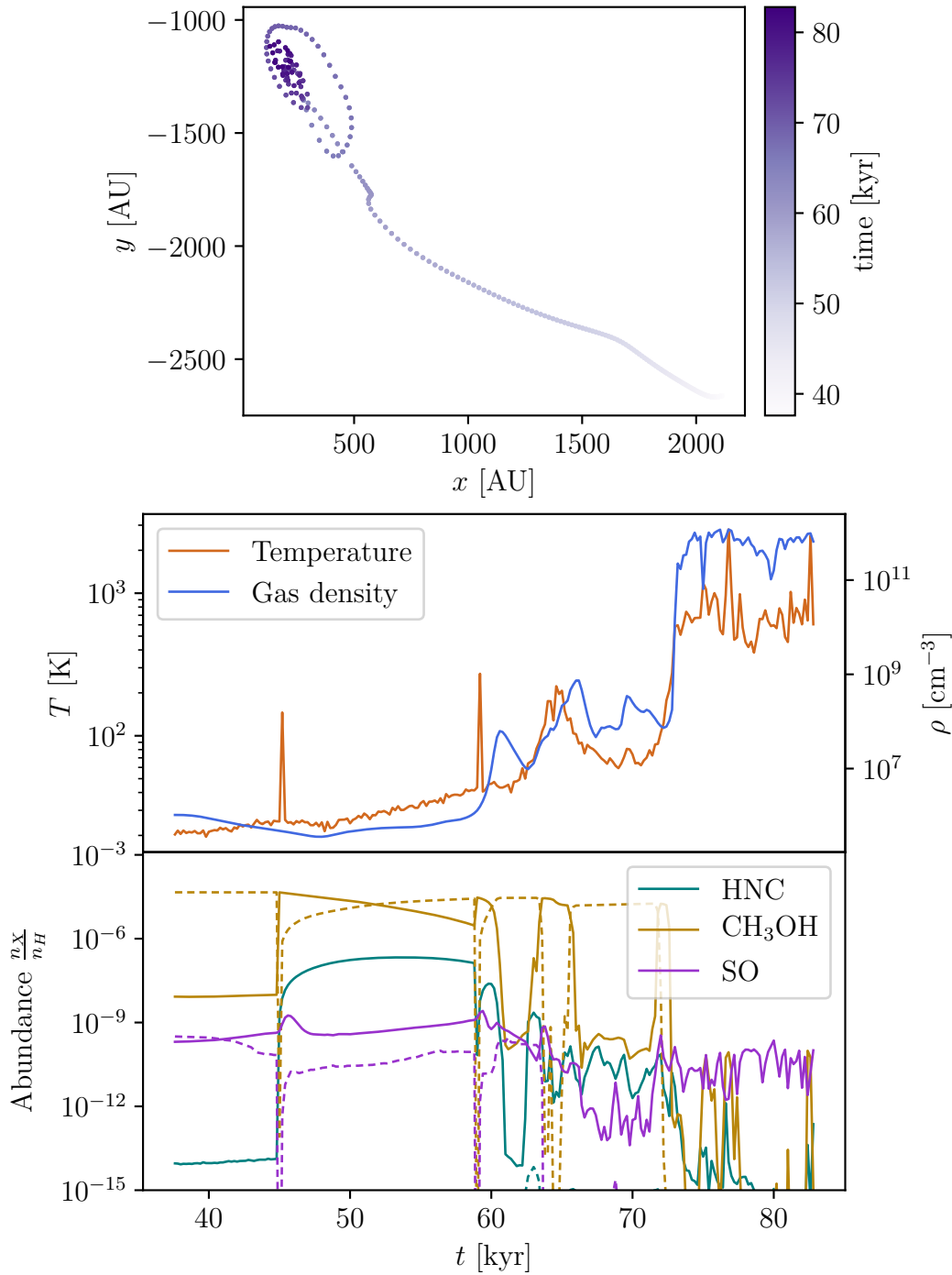


Figure 14: (top) The projection of the trajectory of an example particle on x-y plane. This is an in-falling particle. The color bar shows the time. Note that the protostars and hence, the center of the in-fall moves throughout the simulation. (middle) The input of Saptarsy, including temperature and density of the example particle and (bottom) the output of Saptarsy for the example particle, only a few species are shown here as examples. The solid lines are gas and the dash lines are dust abundance.

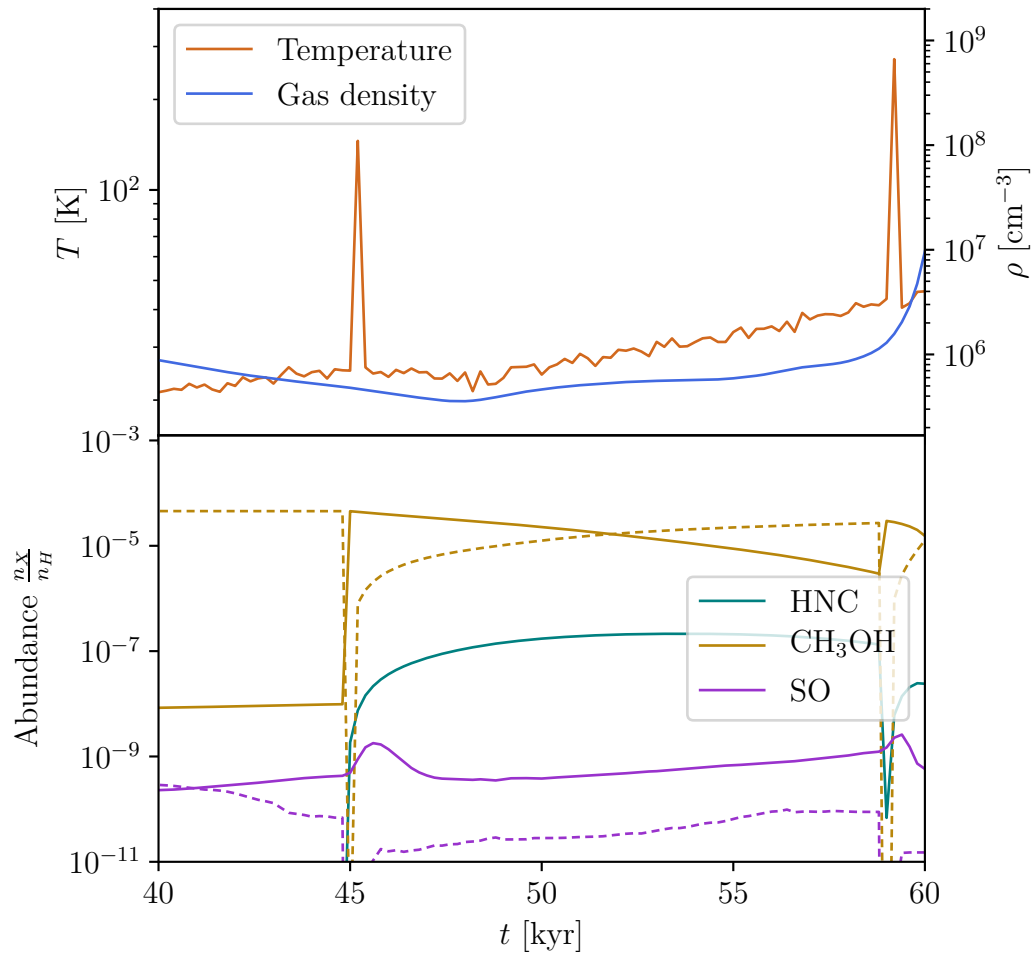


Figure 15: zoom in on the left side of the middle and bottom panels of Figure 14

in the input results in a big diversity in the chemical output space. Figure 17 shows the diversity in the abundance of methanol. Besides the big variation in the time evolution of the abundances of different particles, parts of the plot are more populated than others. The distinctive dark horizontal lines in Figures 16 as well as 17 show some semi equilibrium state. This is presumably the colder material from the outer regions. One sees that these features become less dense with time, as the system continues to collapse and less gas resides in outer regions. In addition the protostars become hotter and more luminous as they evolve and accrete more. The dark vertical lines, visible in temperatures and abundances, yet absent from the density are the accretion events, which impact a big portion of the gas.

In the next sections I will go through different analysis methods I have performed on the simulation outputs to look at the effects of the episodic accretion and episodic outflow scenario on the chemistry of the core.

To get a handle of the high dimensionality of the problem and get a feeling about the general behavior of the system, I use binning and averaging of my data. I start by binning the data in temperature bins in Section 4.1 and then follow it by radial bins in Section 4.2. Afterwards I look into the distribution of the data and the spread in radial bins in Section 4.3.

## 4.1 Temperature bins and chemical memory

Since temperature is an important factor in chemistry, first I bin the particles in temperature bins. In Figure 18 I plot the abundance of methanol against the temperature. The x axis is temperature and the y axis is the mean abundance of methanol in each temperature bin. The particles are binned in ascending temperature bins, such that there is a fixed number of particles of 1500 in each bin. If the number of particles be much lower than this, the lack of number statistic makes the result too noisy. Whereas if the number of particles are chosen to be much higher in each bin, the temperature variation within one bin becomes too big. Different line colors are different times. The red line is the snapshot right before the first accretion event, which puts it at 200 kyr before the flare and the rest are from snapshots after that accretion event and each is 1 kyr apart. This is a prototype of this kind of plots and we will keep the same setting for the rest which follow.

Figure 18 shows a curious behavior of methanol under the effects of the flares. The mean gas abundance of methanol is elevated by several orders of magnitude right after a flare and it remains high even after a few kilo years. This phenomena becomes more interesting if one pays attention to the temperature range it

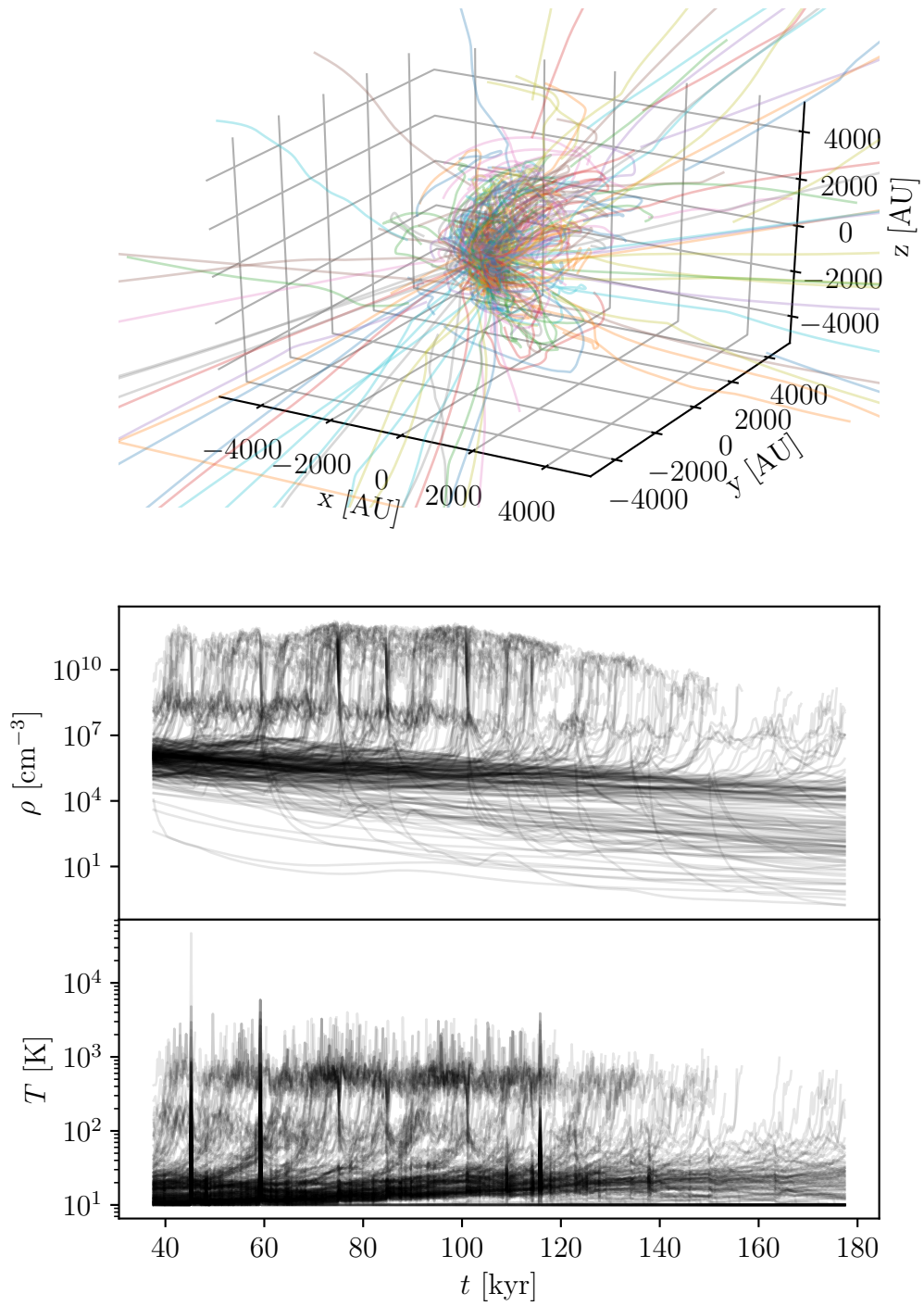


Figure 16: The trajectories (top), the densities (middle) and the temperatures (bottom) of a randomly selected subset of the SPH particles throughout the simulation; about 0.5 percent of the total number of SPH particles.

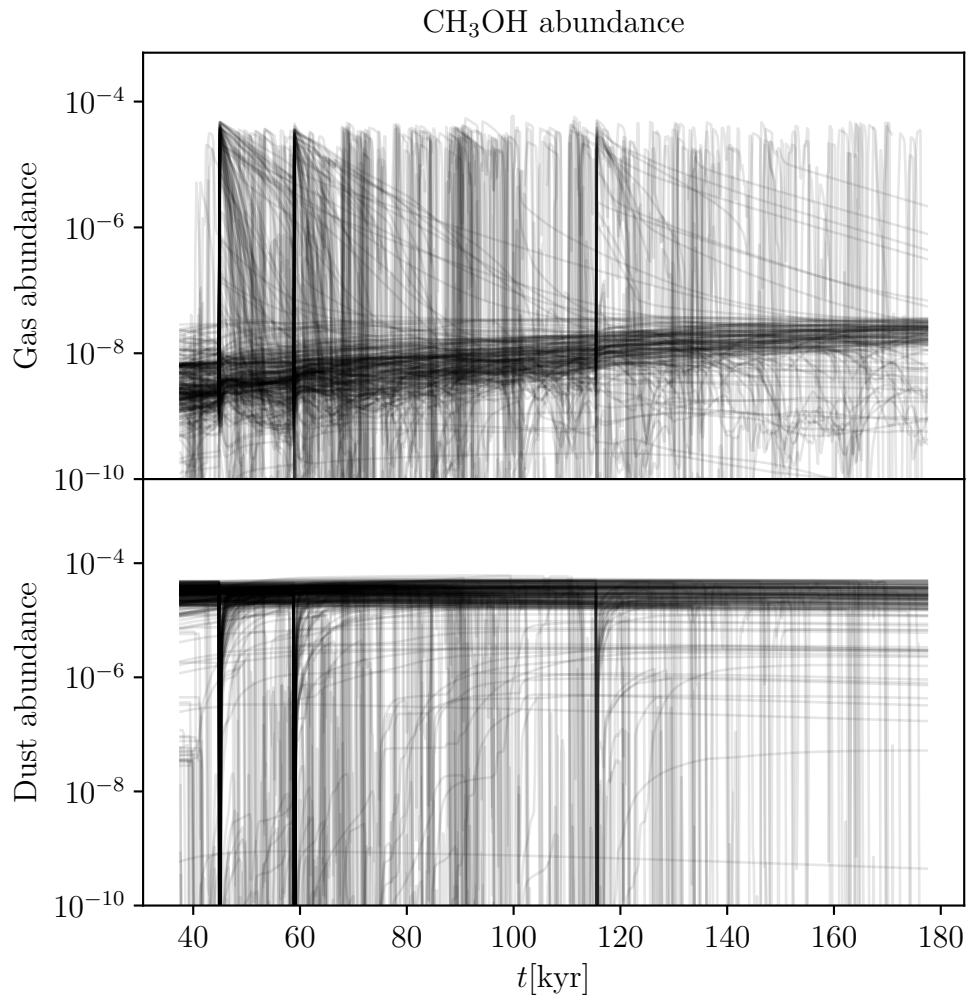


Figure 17: The gas (top) and the dust (bottom) abundance of methanol for a randomly selected subset of the SPH particles throughout the simulation

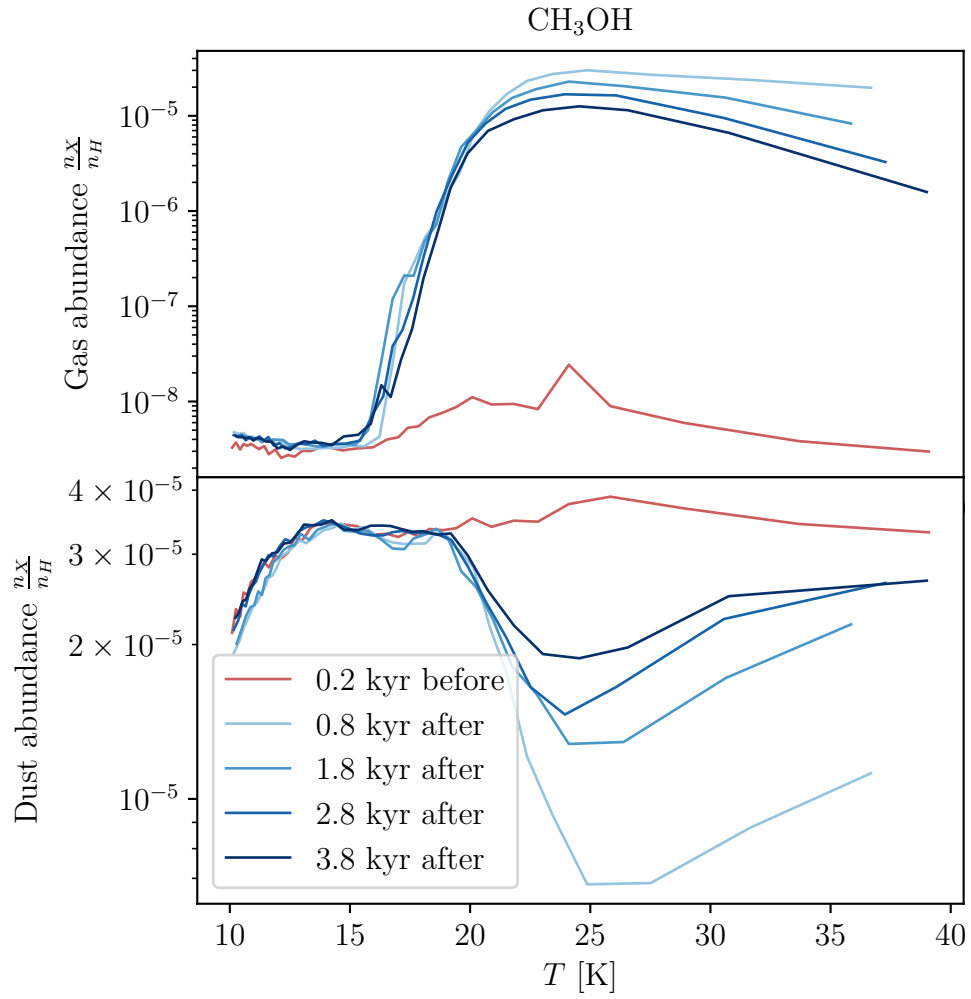


Figure 18: Mean abundance in temperature bins. Each bin has a fixed number of particles (1500 particles). Different times are different line colors. The red line is the snapshot right before the first flare and the rest of the lines are the times after that flare and each is 1 kyr apart. The top panel is the gas and the bottom panel is the dust abundance

occurs at. The temperature is between around 25 and 40 Kelvin. This is not temperatures in which one expects to find methanol in the gas phase. Methanol is produced on dust and is buried under ice mantle. It gets into the gas phase via thermal desorption. The temperatures needed for thermal desorption of methanol is between 100 and 200 Kelvin (see Section 4.3.2 and Equation 21) and these temperatures are way below those ranges. If one looks at the mean dust abundance in the lower panel of the Figure 18, one sees that there is a corresponding decrease in dust abundance in the same temperature range. Therefore one can deduce that during the flare, the accretion heating removes the methanol from the dust and into the gas phase. The temperature drops after the accretion event, yet the process of freezing out onto the dust grains takes some time and it results in high abundances of methanol in gas phase for some time after the flare.

We do observe methanol and other COMs in low mass prestellar cores (Vastel, Ceccarelli, Lefloch, and Bachiller (2014), Jiménez-Serra et al. (2016) for L1544 in Taurus and Taquet et al. (2017) for Barnard 5 in Perseus). The existence of methanol and COMs in cold regions poses a challenge for our existing models. Either these molecules are not produced on dust grains, or they get into the gas phase via other processes. There is no consensus on what these other processes are (Jørgensen et al., 2020; van Dishoeck, 2018). Some of the suggested models try to find non-thermal mechanisms for desorption of methanol off the dust. For example cosmic rays could sputter the ices, UV photons could cause photodesorption, or newly formed molecules can be excited and hence desorb through reactive desorption. However, lab studies on ices show photodesorption is not efficient in producing methanol Bertin et al. (2016); Martín-Doménech et al. (2016). Another theory explains the the production of certain COMs by reactions of H and O atoms with the surfaces of carbonaceous grains themselves, which could be a possible route for producing methanol (Potapov et al., 2017).

In this study the episodic accretion produces methanol, which lingers in low temperature regime, hence the simulation results suggest that episodic accretion scenario can be a candidate for producing methanol in cold cores. If the accretion events are close to each other, The methanol abundance will remain high. Figure 19 shows the same kind of plot as Figure 18, but for the second flare which is only 14 kyr apart from the previous flare.

In this plot, while the behavior after the flare remains similar to the one for the first flare, the abundance before the flare is still very high. This is in agreement with the expectation of methanol gas abundance to remain high while accretion events happen frequently and close to one another.

Using the same analysis for different molecules I find 4 different groups based on the way they respond to the flares.

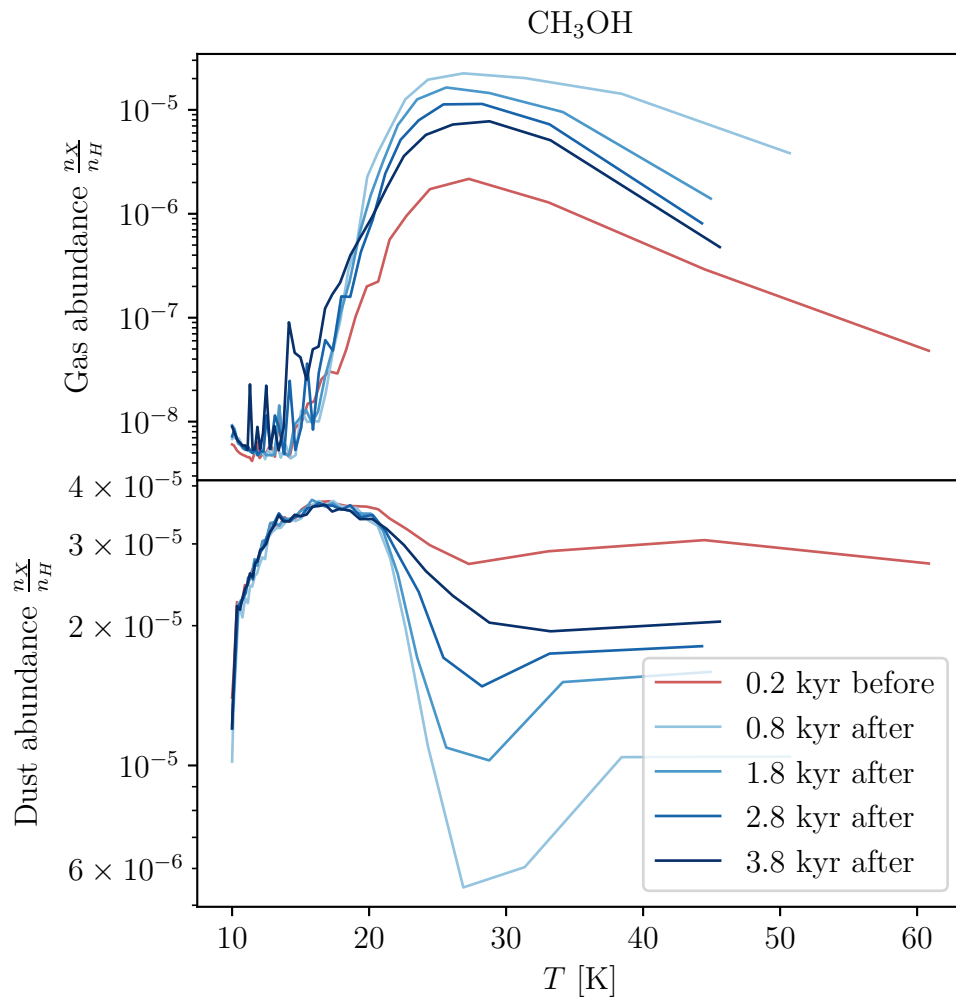


Figure 19: The same plot as Figure 18, only for the second flare.

Some molecules behave very similar to methanol, such as water and ammonia (Figure 20). These molecules are also produced on the dust grains and desorb into the gas phase via thermal desorption. Since they are also injected into the gas during the flares, they exhibit very similar response to the flares.

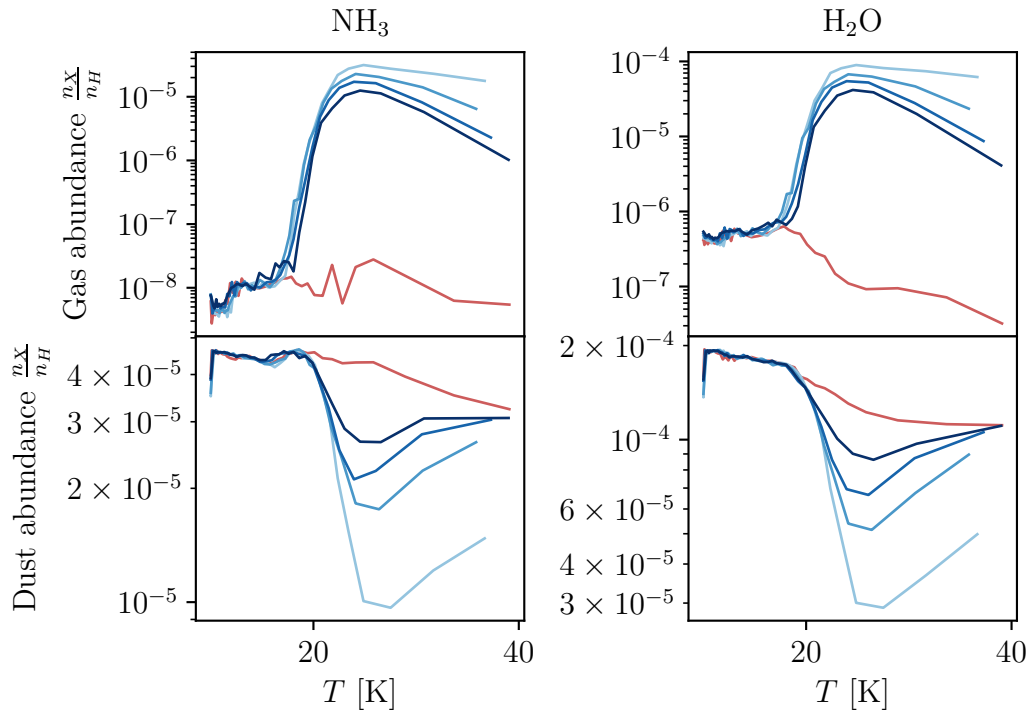


Figure 20: Mean abundance of ammonia (left panel) and water (right panel) in temperature bins, with the same procedure as Figure 18.

Figure 21 shows the behavior of HCN and HNC. We see that their gas abundance shows the same trait as methanol, while their dust abundance seems to be quite different. This is because these two molecules have different formation processes. They are produced in the gas phase. But their production has an energy barrier which is overcome during a flare and as such, their abundance increases after an accretion event.

Another class of behavior belongs to ions, such as  $\text{HCO}^+$  and  $\text{N}_2\text{H}^+$ . We chose these two specific ions to show here, because they are some of the most observed ones in the hot cores. In Figure 22 we see that these molecules get destroyed during a flare but they return to their previous state much faster than our dust produced species. The ions do not exist on dust, because dusts are often negatively charged and ions immediately recombine. That is why I only show their gas abundance. The ions are highly reactive and as soon as there are other molecules in the gas phase, they react and that is why they are removed from the gas phase during the flare.

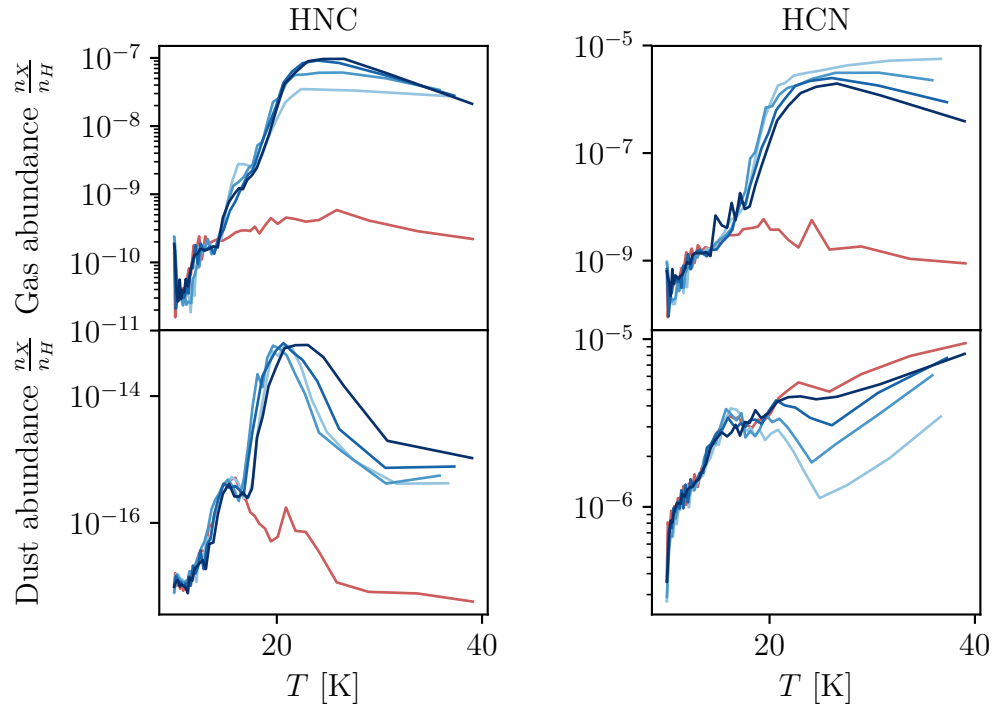


Figure 21: Mean abundance of HNC (left panel) and HCN (right panel) in temperature bins, with the same procedure as Figure 18.

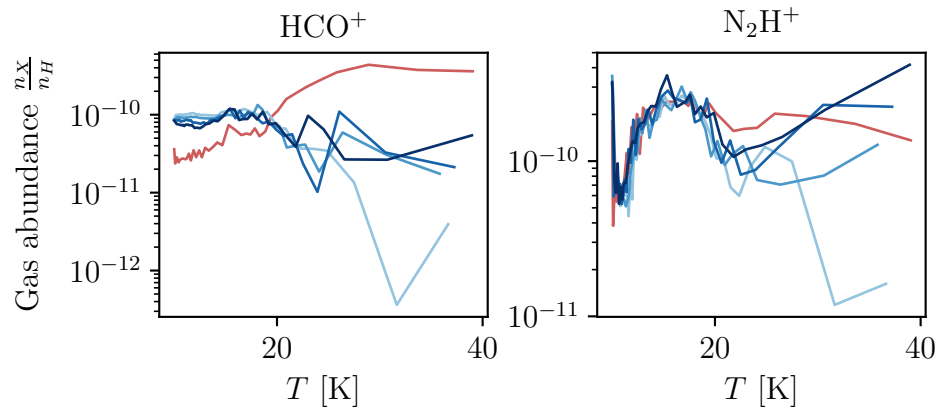


Figure 22: Mean abundance of  $\text{HCO}^+$  (left panel) and  $\text{N}_2\text{H}^+$  (right panel) in temperature bins, with the same procedure as Figure 18.

Beside this type of molecules which experience rapid changes after the flare, there is another class of molecules which behave very differently. Figure 23 shows the same type of plots for SO and H<sub>2</sub>S.

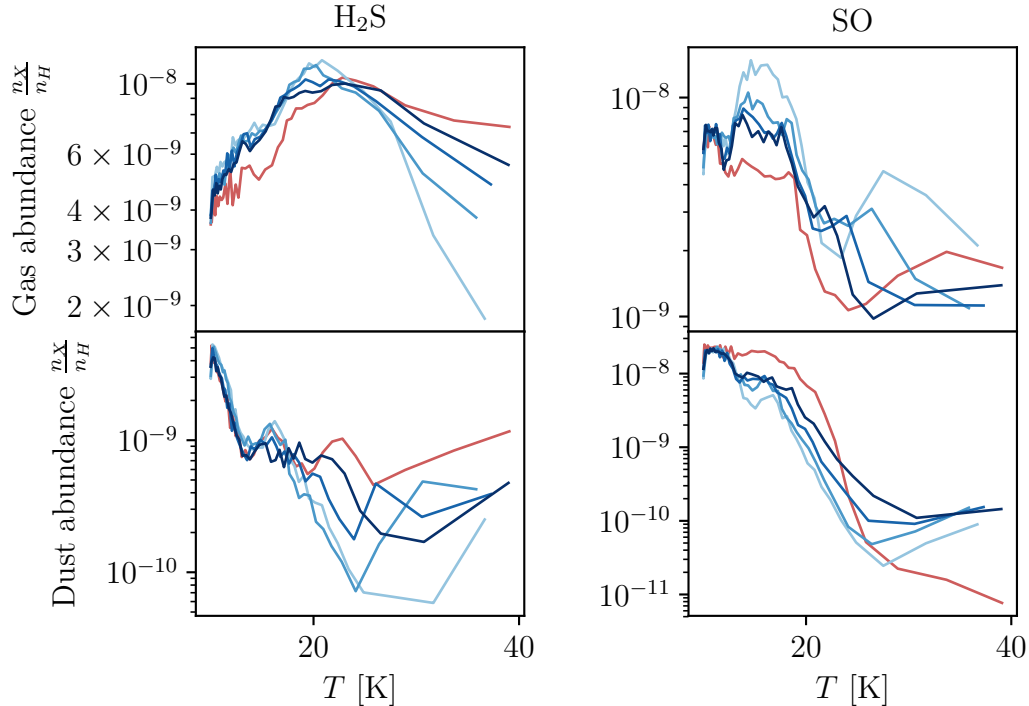


Figure 23: Mean abundance of H<sub>2</sub>S (left panel) and SO (right panel) in temperature bins, with the same procedure as Figure 18.

In this figure the mean abundance before and after the flare do not show considerable difference. It seems that these species forget about the flare, right after it happened. So in this sense, we can talk about chemical memory. Certain species, such as methanol, water, ammonia, etc, have a chemical memory of the thermal history of the system, while others such as H<sub>2</sub>S and SO do not. This is an important finding. Because while using different molecules to calculate different physical properties of an astronomical system, it is important to know which one is tracing the history of the system and which ones are tracing the state of the system at the moment of observation.

Because of the complexity of the chemistry I cannot look into every species beyond a general classification. From here forward I will focus only on methanol and how its dynamic and complex distribution, in an attempt to find how it is coupled to the physics of my collapsing core model with episodic accretion and episodic outflow feedback. Methanol is an important molecule in the formation of iCOMs (see Section 1.1.3). So modeling it correctly, is key for modeling other iCOMs .

## 4.2 Radial bins and the range of accretion heating on chemistry

From this section onward, I put my focus on methanol. It is the prototype of the molecules produced on dust. As we saw before these types of molecules react in a non-linear way to accretion episodes and seems to carry some sort of chemical memory of these events. So I look into methanol in more detail.

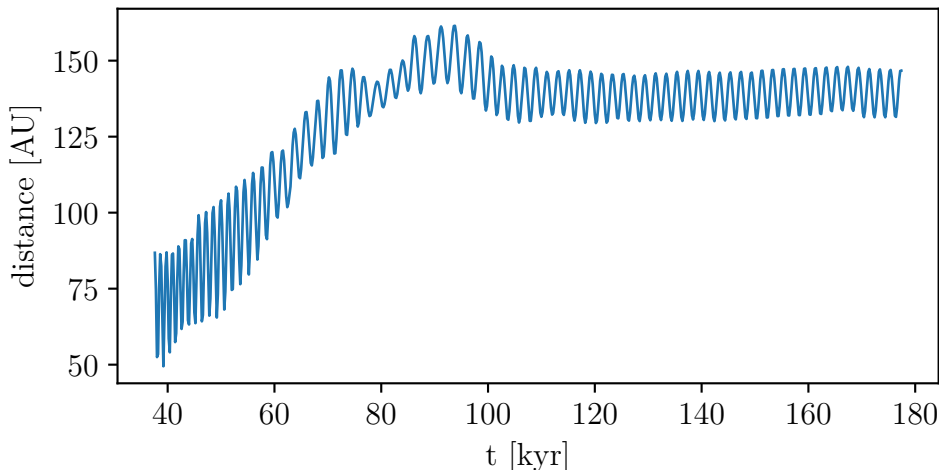


Figure 24: The distance between the two protostars as they revolve around each other throughout the simulation.

I want to look at the spacial distribution of this effect. I bin the particles in logarithmically-spaced radial bins and look at the mean of abundance of methanol and its time evolution in each bin. The result is shown in 4 dimensional Figure 25. The x axis is time, y axis is radius and the surface is the logarithm of the mean abundance in each temperature bin. The color bar is the logarithm of temperature. I bin the space between 250 AU and 10 000 AU into 16 logarithmically-spaced bins. My proto-stars are rather a tight binary (Figure 26), whose distance to one another varies between 50 and 160 AU throughout the time of my simulations. The lower limit of the radial bins (250 AU) is set so that we are fairly outside of the binary. Figure 24 shows the distance between the two protostars throughout the simulation. The maximum distance between the two protostar is 161.5 AU, therefore, 250 AU is sufficiently distant from the center of mass of the binary. For the outer limit and the number of bins I chose the same values I used to sample the gas, which ensures that I have good number statistics within each bin throughout the simulations. The sampling method is explained in Section 3.1. For center and the reference point from which I calculate the radii, I made a correction for the movement of the binary and used the middle point of the line

connecting the two sink particles as the center, as the binary moves hundreds of AU while spinning around their center of mass. Figure 26 depicts the positions of the two sink particles, i.e the protostars and the center throughout the simulation.

One of the first features one notices in Figure 25 are the 3 big peaks of abundance, which are marked by high temperatures, the sharp increase and the slow descent until the next peak. One also observes that these peaks are localized to a specific radius, after which they diminish and before which, we see a very spiky, noisy looking region. To get a better understanding of these features, I project this plot on x-z plane and I separate these three regions; the interior, the mid-range and the exterior.

#### 4.2.1 Mid-range

This region spans between radii 400 to 3000 AU (Figure 27). I start with this region because it is where one sees the effect I was expecting to see from Section 4.1.

In Figure 28 I show the mean abundance of methanol in 6 linearly spaced radial bins. One observes the 3 big peaks with the instantaneous increase of gas abundance and a sudden decrease in dust abundance. Comparing this plot with Figure 29, which depicts the mean temperature and density in the same bins, one sees that these peaks coincide with the temperature peaks. The temperature peaks in this radius range varies between 60 and 300 K and are, as said before, caused by accretion heating in each accretion event. These events have life times of the order of 10 years and since the output frequency of the hydrodynamic simulations are 200 yrs, accretion events result in a single output point. This behavior is in agreement with what I deduced in Section 4.1. Methanol comes off the dust very abruptly at the sharp increase of temperature, when the temperature goes above 100 K in flares and then slowly freezes out back on the dust. Note that in the third flare, the temperature peaks are lower than the first two. Hence, the three outer radial bins (radii larger than 1700) have mean temperatures below 100 K and the abundance increase in them looks dissimilar to the rest with temperature higher than 100 K. In following sections I will look more closely in the chemistry and the exact reaction channels which gets active in different temperature ranges.

One also sees small peaks in methanol abundance and they do not seem to correspond to any temperature peaks, i.e. the accretion events. To investigate further I plot the time evolution of mass and luminosity of the protostars, from the hydrodynamic GANDALF simulation (Figure 30) in the same time interval as my Saptarsy simulations. In this plot we see that there are more accretion events

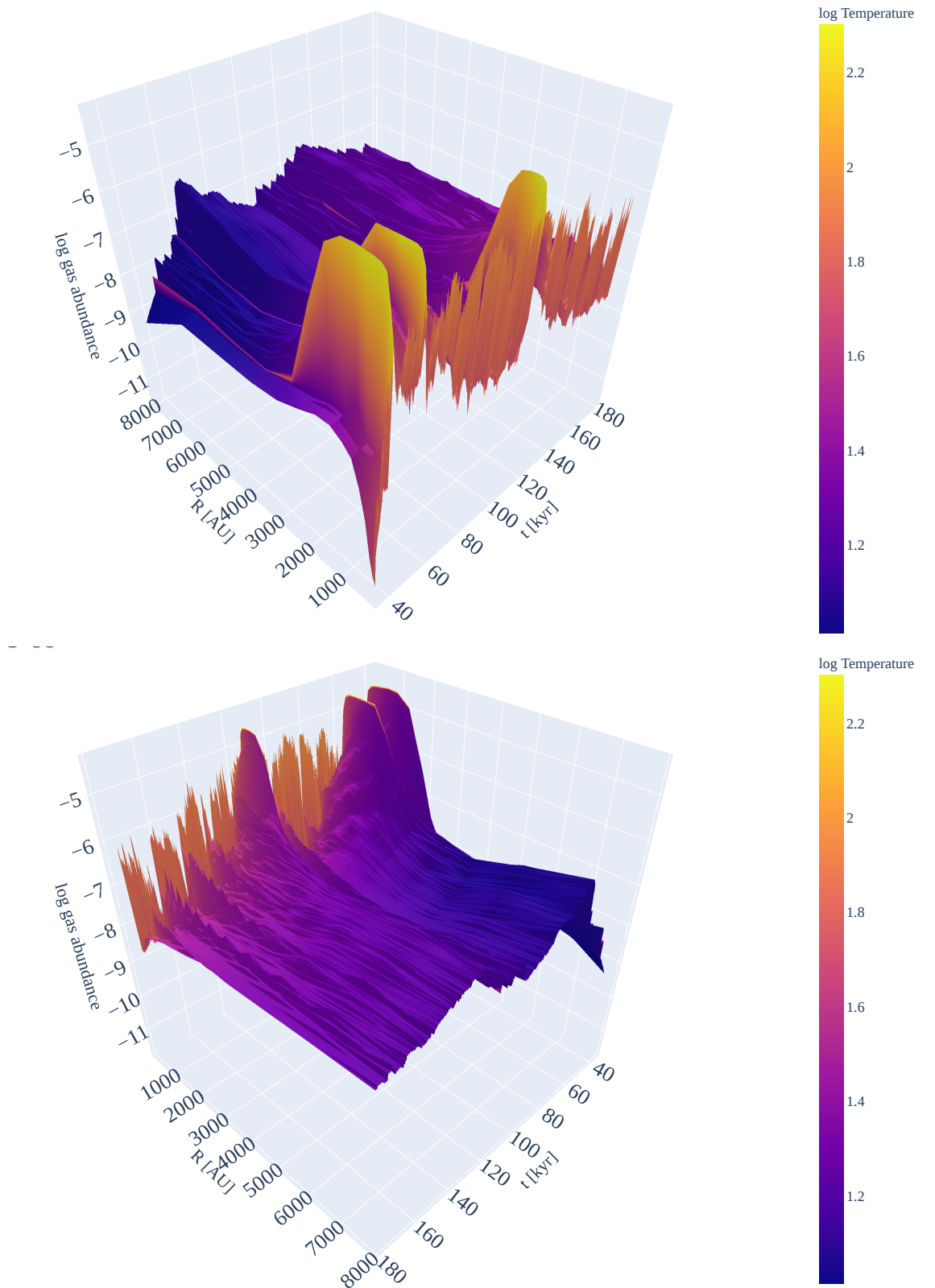


Figure 25: 4 dimensional mean methanol gas abundance in logarithmically-spaced radial bins. The x axis is time, the y axis is radius and the surface is the mean gas abundance in the radial bins ( $n_x/n_H$ ). The color-bar is the temperature in kelvin. The top and bottom panel show two different angles of the plot.

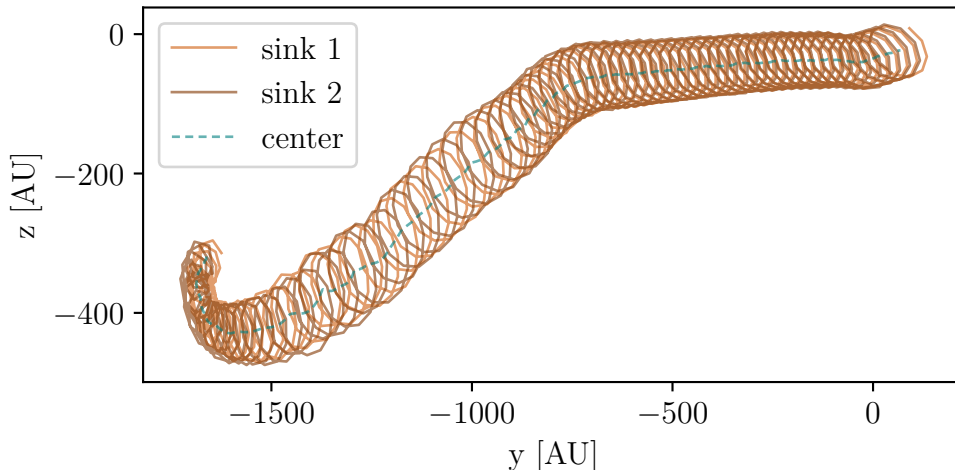


Figure 26: Position of the two protostars throughout the time interval of the simulation we are using for our work. The position of the middle of the line connecting the two protostars is overlaid.

as the luminosity peaks. Luminosity peaks correspond to the peaks which are visible in the temperature in Figure 29. This is because the output frequency of the hydrodynamic GANDALF simulations are set to one every 200 years. Because the time scale of an accretion event in episodic accretion scenario is of the order of 10 years, the accretions events are not properly resolved in time. There seem to be valleys in temperature corresponding to the unresolved accretion events.

The valleys in temperature could be caused by small contraction of protostars right after a flare, which translates to a drop in luminosity. Another possible cause to these temperature features could be the mechanical and dynamic effect of outflows as they move the material around and change the local density, hence changing the local visual extinction and as a result, the temperature calculated via RADMC3D. Meaning they could possibly disentangle the effect of outflows from the accretion events. In Section 4.3.1 I will revisit this topic, however, understanding these small minimums in temperature and peaks in abundance needs further investigation, which goes beyond the scope of this work. Future studies need to take temporal resolution into account. Specially since even in the case of the peaks we have caught, they are only one data point and we do not resolve the decay of the flare and understanding this type of chemistry seems to need a very high temporal resolution. implementing an adaptive temporal resolution could be a possible solution. More over, any attempt to disentangle outflow and accretion effects on chemistry, needs to include different hydrodynamic simulations turning episodic accretion and outflows on and off, as well as similar chemistry simulations on each of them to see how they affect chemistry.

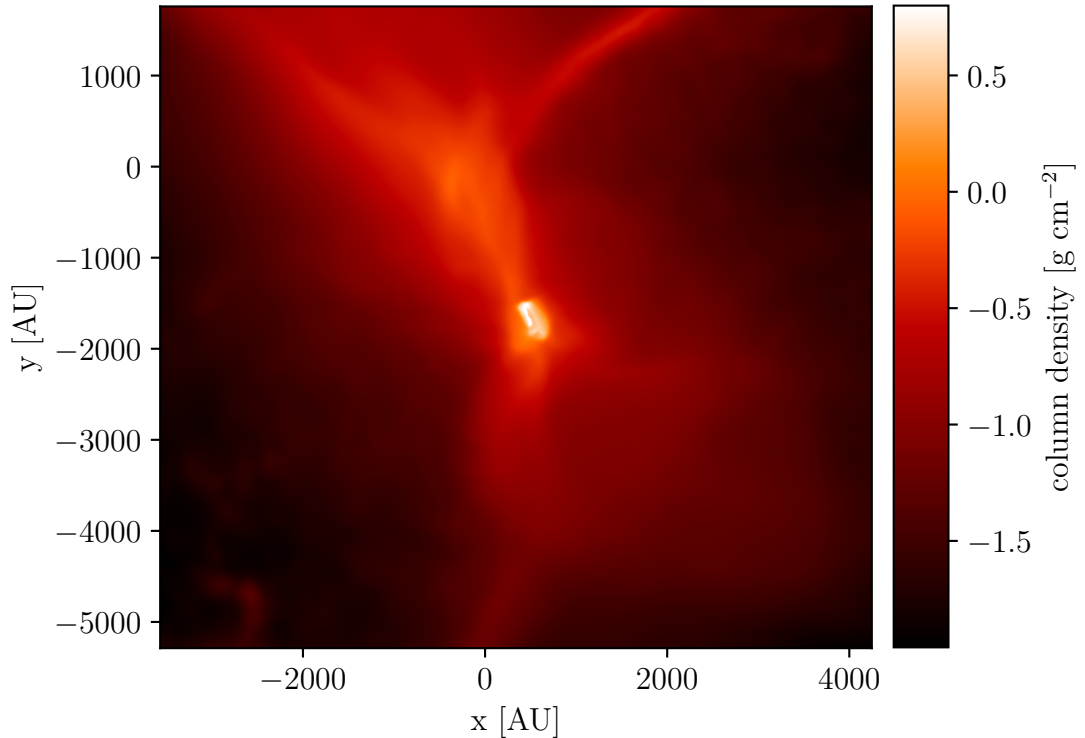


Figure 27: Column density map of the region of roughly 3000 AU radius from the binary protostars, which covers the mid-region. This is a snapshot at 50 kyr into the simulations and is located between our first two flares.

#### 4.2.2 Exterior

This is a region with radii between 3000 and 10000 AU. I have plotted the gas column density of this region in Figure 31. On this scales one sees the outflow cavity. I bin the particles of this region into 5 linearly-spaced bins and plot the average abundance of methanol in each bin (Figure 32).

In this plot we see a different behavior than the mid-range. There is no corresponding peak in gas abundance at the exact time of the flares, neither is there a corresponding valley in the dust abundance. The reason becomes clear if one looks at the mean temperature in the same bins in Figure 33. This region is far enough from the central objects, so that the peak temperatures at flares reach between 30 and 60 K. This is not enough temperature to cause thermal desorption. Thus the methanol remains buried under ice mantle of the dust.

That being said, there are still some peaks in Figure 32. They occur after the flare and their position is shifted to later times in the larger radii. These peaks are also flatter on the top compared to the abundance peaks in Figure 28. Comparing this plot with the corresponding temperature plot (Figure 33), there is no indication of any significant change in temperatures or density to explain this. I postulate that this can be material being dragged out by the outflow bullets

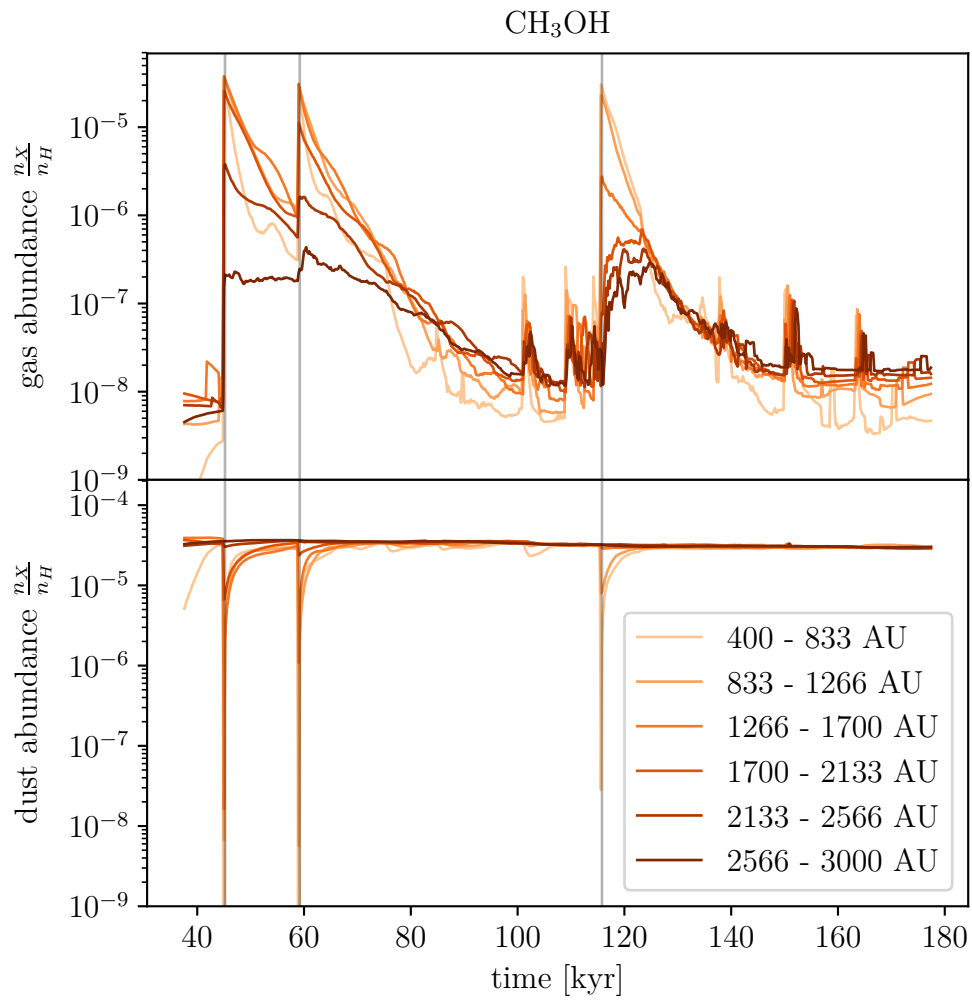


Figure 28: Mean gas (upper) and dust (bottom panel) abundance of methanol in 6 radial bins, i.e annuli around the protostars, between 400 and 3000 AU. The vertical lines indicate the position of the flares.

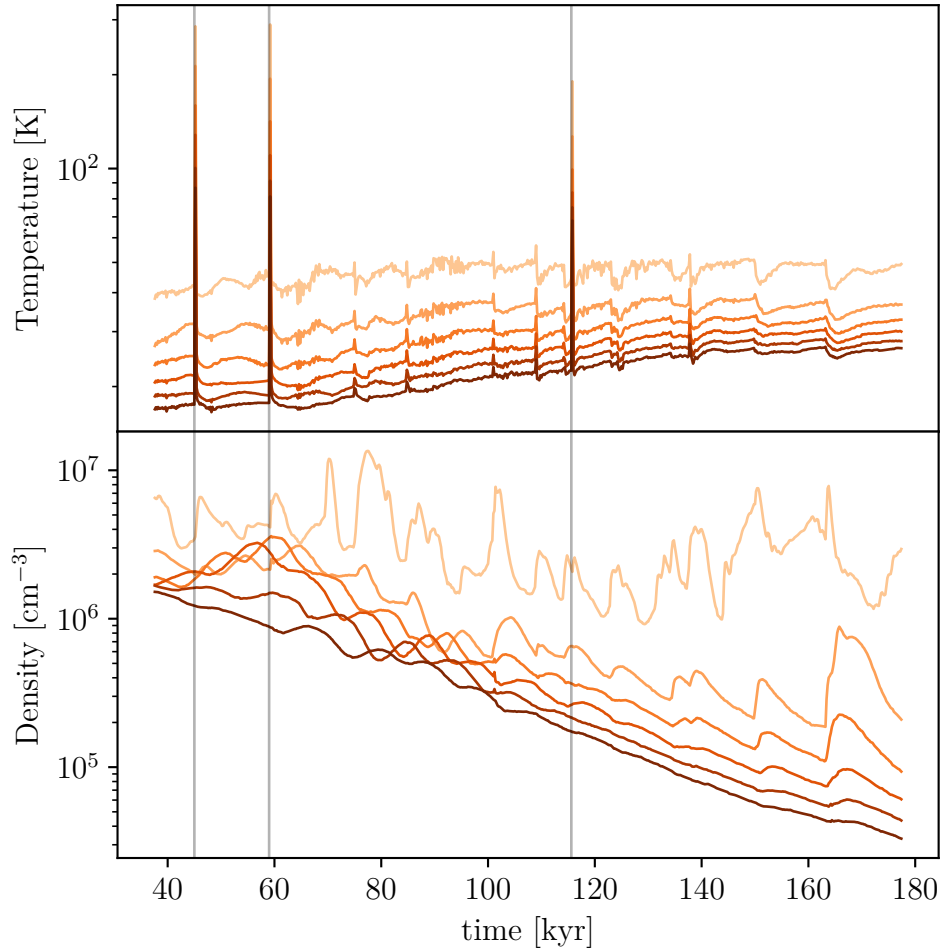


Figure 29: Mean temperature (upper) and density (bottom panel) in the same 6 radial bins as 28. We keep the same color scheme, which means we go from lighter to darker colors as we go from inner to outer layers between 400 and 3000 AU and the vertical lines indicate the position of the flares.

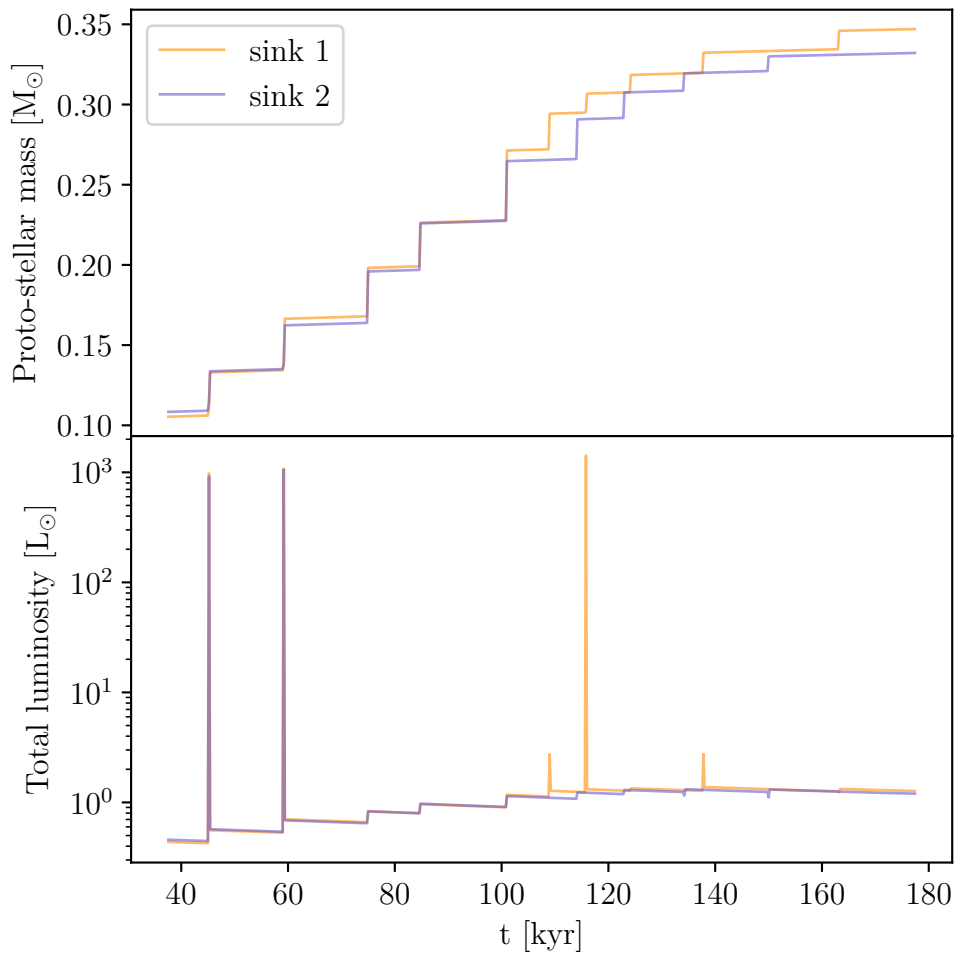


Figure 30: Time evolution of mass (upper panel) and luminosity (lower panel) of the protostars.

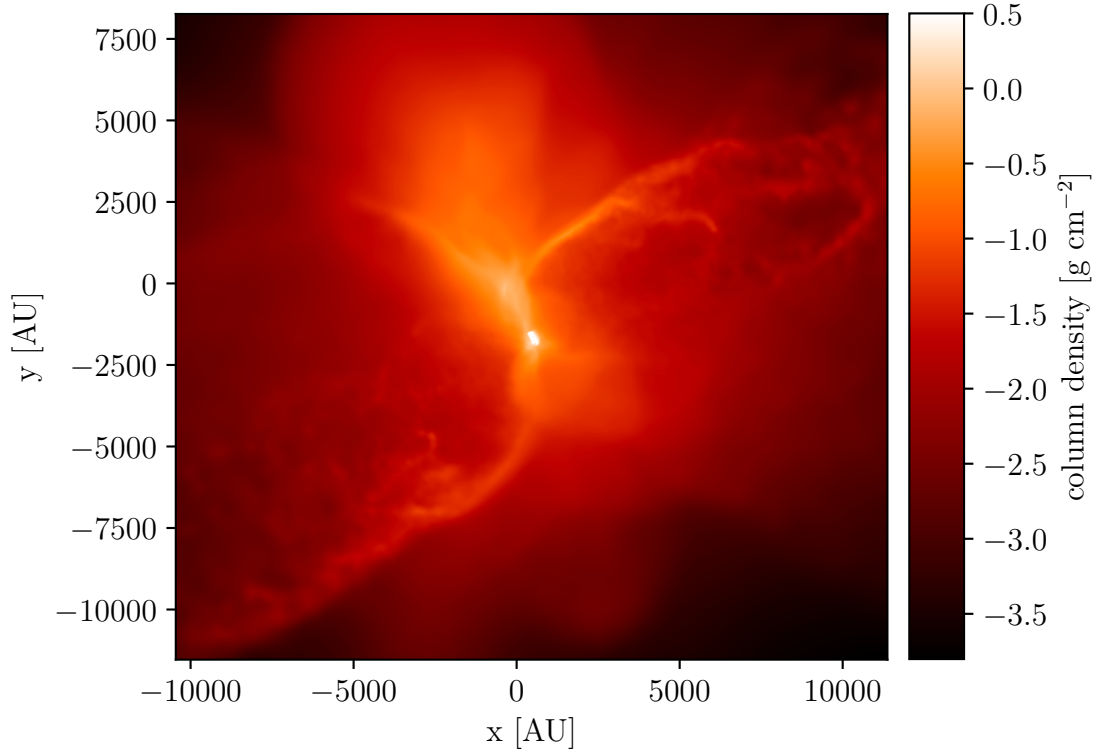


Figure 31: Column density map of the region of roughly 10000 AU, which covers the exterior region. This is a snapshot at 50 kyr into the simulations and is located between our first two flares.

from the more inner region. This material is presumably in smaller radii during an accretion event, therefore it was impacted by the accretion heating and gained high methanol abundance. Then it is dragged outward as its trajectory intersects with the outflow cone, hence enriching the gas with methanol and possibly other COMs at larger radii. I investigate this phenomena in later sections (see Section 4.3.3).

### 4.2.3 Interior

This is a region between radii 100 and 400 AU. I map the gas column density in Figure 34. On this scales one can see the binary and the disk clearly. I bin the particles in this region into 3 linearly spaced radius bins. I show the mean gas and dust abundance in each bin in Figure 35. The main feature of the plot in this region is large stochasticity. To understand this behavior I plot the mean temperature and mean density in the same bins (Figure 36).

Upon comparing the temperature and density plot in this region with the middle and exterior region (Figures 29 and 33 respectively), both the temperature and especially the density in the interior has a similar small scale variability. Furthermore the density is much higher than the outer regions. The overall rate of

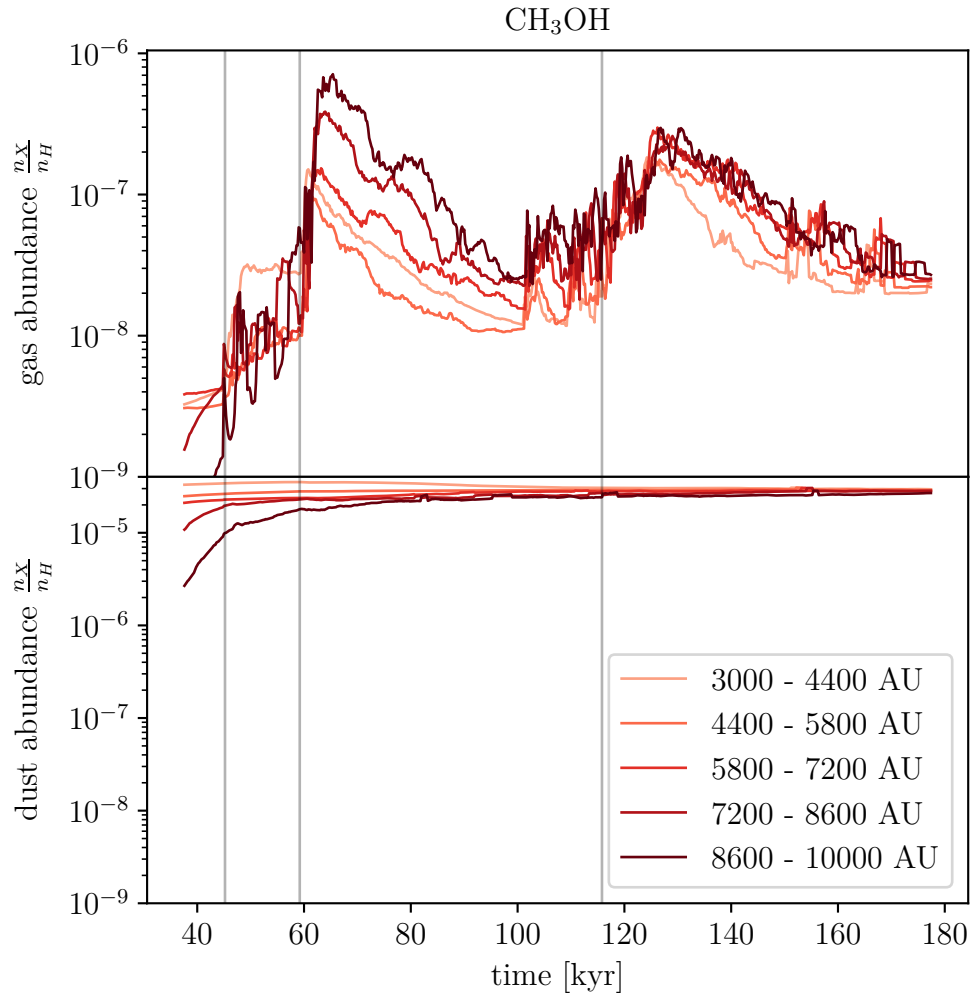


Figure 32: Mean gas (upper) and dust (bottom panel) abundance of methanol in 5 radial bins, i.e annuli around the protostars, between 3000 and 10000 AU. The vertical lines indicate the position of the flares.

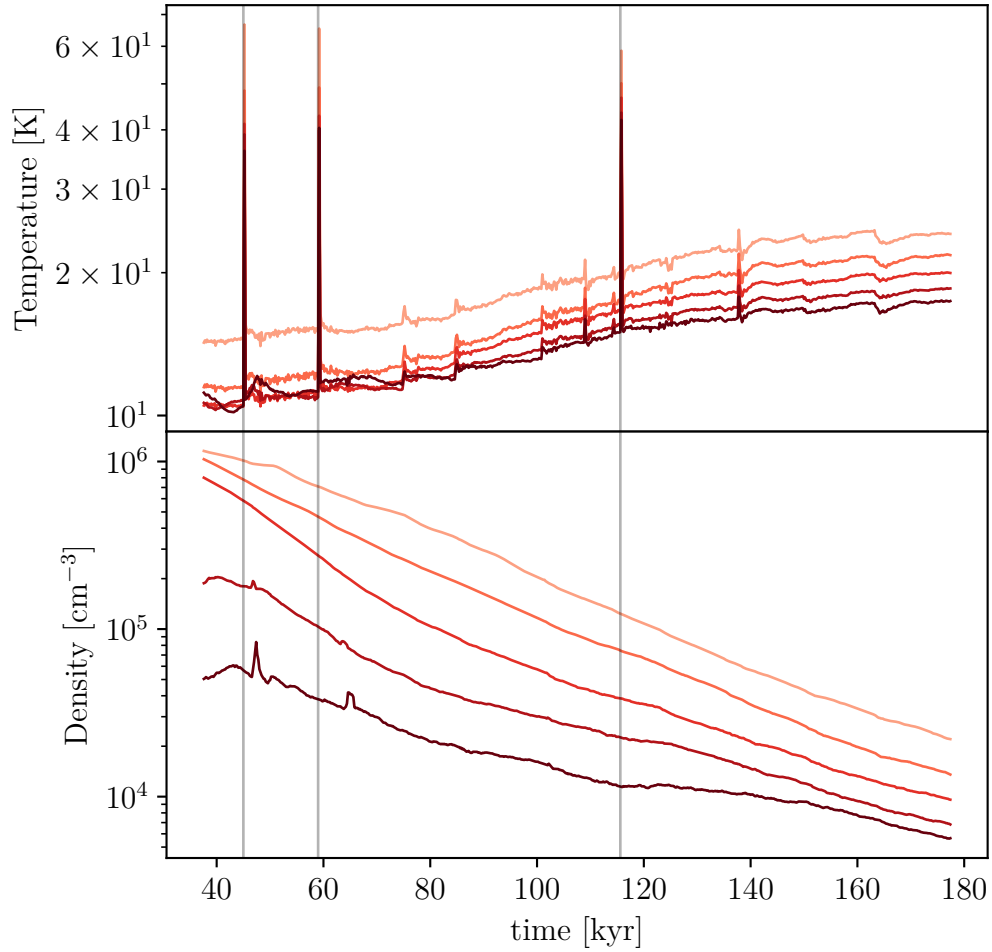


Figure 33: Mean temperature (upper) and density (bottom panel) in the same 5 radial bins as Figure 32. We keep the same color scheme, which means we go from lighter to darker colors as we go from inner to outer layers between 3000 and 10000 AU and the vertical lines indicate the position of the flares.

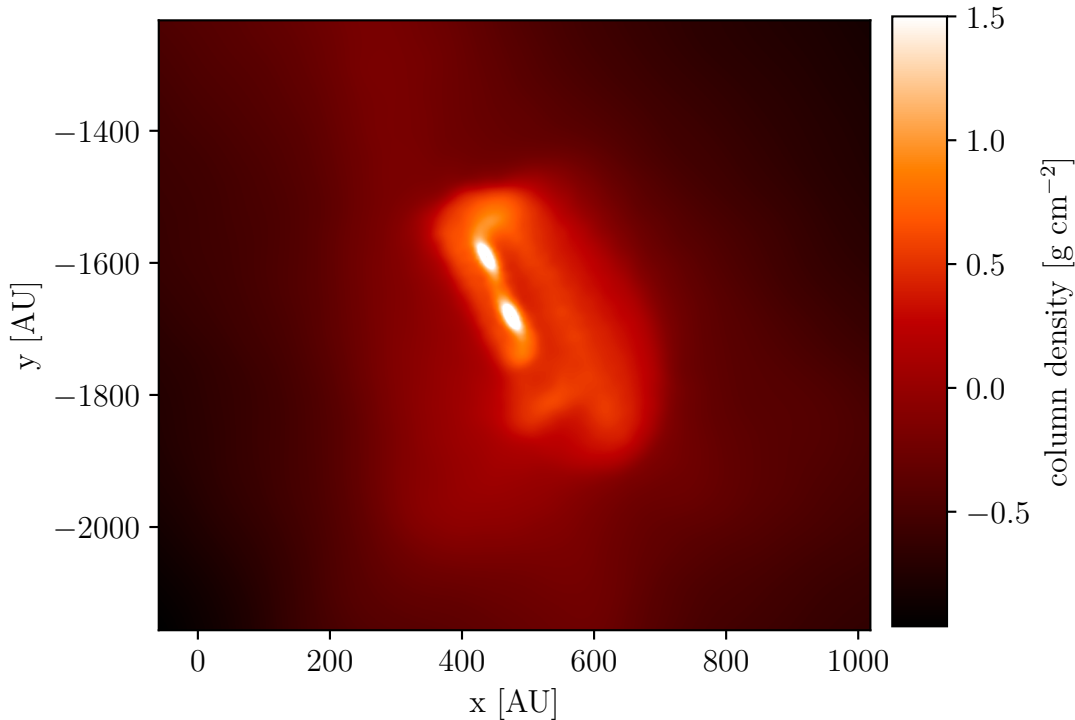


Figure 34: Column density map of the region of roughly 400 AU, which covers the interior region. This is a snapshot at 50 kyr into the simulations and is located between our first two flares.

any reaction is a product of the rate coefficients and the densities of the reactants (see Chapter 1). Hence, the higher the density, the faster is the chemistry. Or in other words having higher densities means that different species have a higher chance to encounter and react with one another. Thus the fast variations in abundance are a reflection of the fast variation in density and temperature. As a result mean is not a good descriptor of a system with such a high variability. In the next section we will look at the distribution of our parameters and abundances to have a better understanding of this variability.

Another interesting feature of the Figure 35 is the behavior of the mean methanol abundance during the flares. In the most outer region (between 333 and 400 AU) we see a peak, similar to the ones of middle range, in mean gas abundance on the flares and corresponding valleys in the mean dust abundance. The other two most inner bins have rather high gas abundance outside of flare and there is a valley both in gas and dust on the first two flares, where the abundance drops from around  $10^{-5}$  to  $10^{-7}$ . In the corresponding temperature and density plot (Figure 36), The temperature on the flare exceeds 400 K. Thus it seems that in temperatures higher than 400 K, other chemistry channels are becoming active which effectively destroy methanol in gas phase. We will investigate this in later sections, where we look more closely into the chemistry.

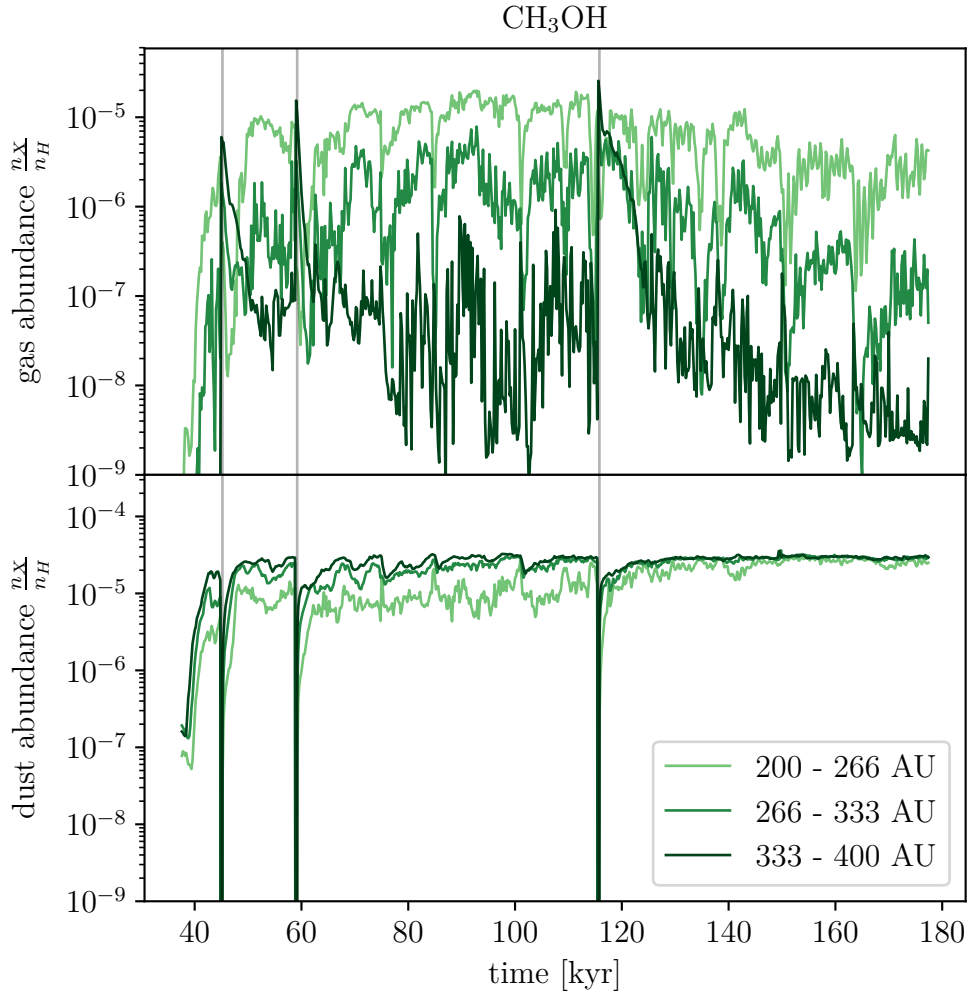


Figure 35: Mean gas (upper) and dust (bottom panel) abundance of methanol in 5 radial bins, i.e annuli around the protostars, between 200 and 400 AU. The vertical lines indicate the position of the flares.

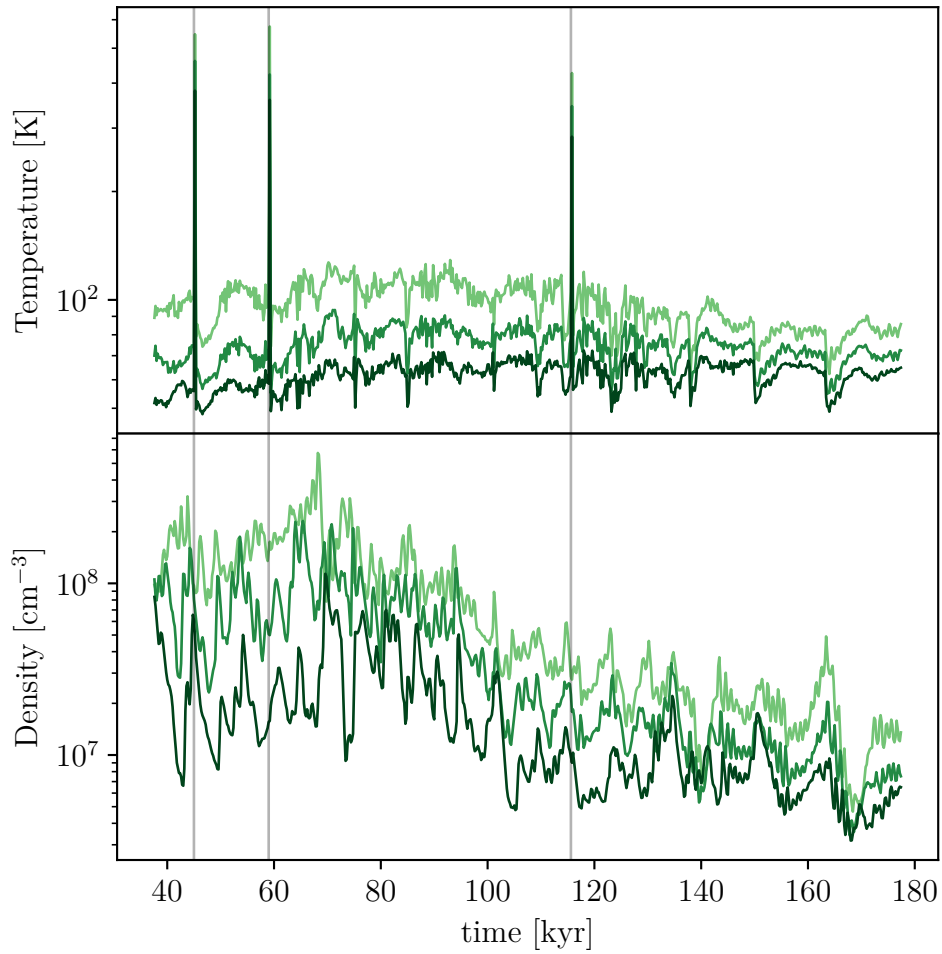


Figure 36: Mean temperature (upper) and density (bottom panel) in the same 3 radial bins as Figure 35. We keep the same color scheme, which means we go from lighter to darker colors as we go from inner to outer layers between 200 and 400 AU and the vertical lines indicate the position of the flares.

### 4.3 Violin plots and chemical inhomogeneity

So far I have only discussed the mean abundance without talking about the spread. In this section I look at the distribution of abundance in the same radial bins as Section 4.2. To investigate this I make violin plots for each bin. Since it mounts to many plots, I pick one plot from each region as a representative. Moreover I make these plots for each of the 3 main flares we are sampling in the time interval I have chosen for our chemistry simulation. Since the general behavior of chemistry is not that different between these three flares, I use different time resolution for the corresponding violin plots. These difference in time resolution emphasizes on different aspects of the distribution, which will become clear next.

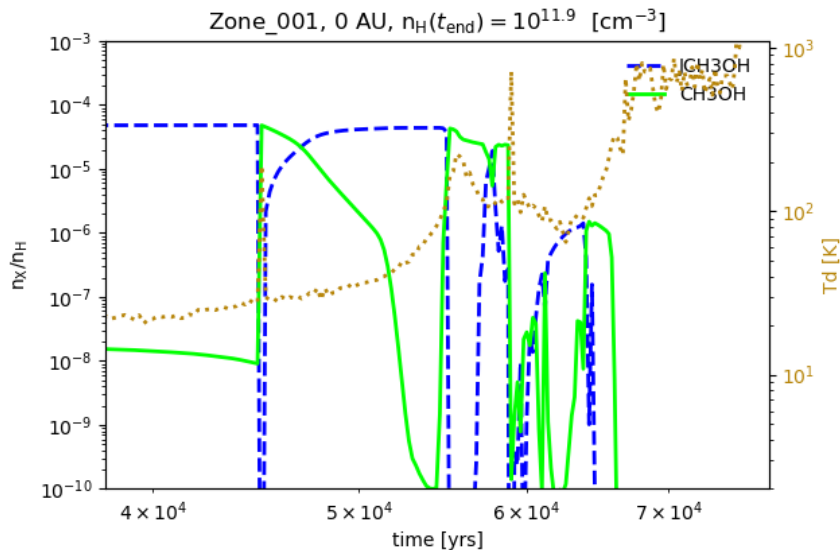


Figure 37: Methanol abundance in gas and dust over plotted with temperature for one example particle, produced by Saptalizer.

I will discuss the behavior of chemistry in the physical condition within our core collapse simulation, which gives rise to the behavior of methanol. To this end, I use an interactive visualization tool, Saptalizer (Schaefer, 2017), which is specifically made to visualize data from Saptarsy. I pick example particles which represent the specific physical condition I am looking at in different regions. Then I look at the reaction rates for formation and destruction of methanol to find the main producers and products, for which I repeat the same procedure and continue, until I find the main routes of production and destruction. These result in small networks for each region. Figures 37 and 38 show example plots produced by Saptalizer for an example particle.

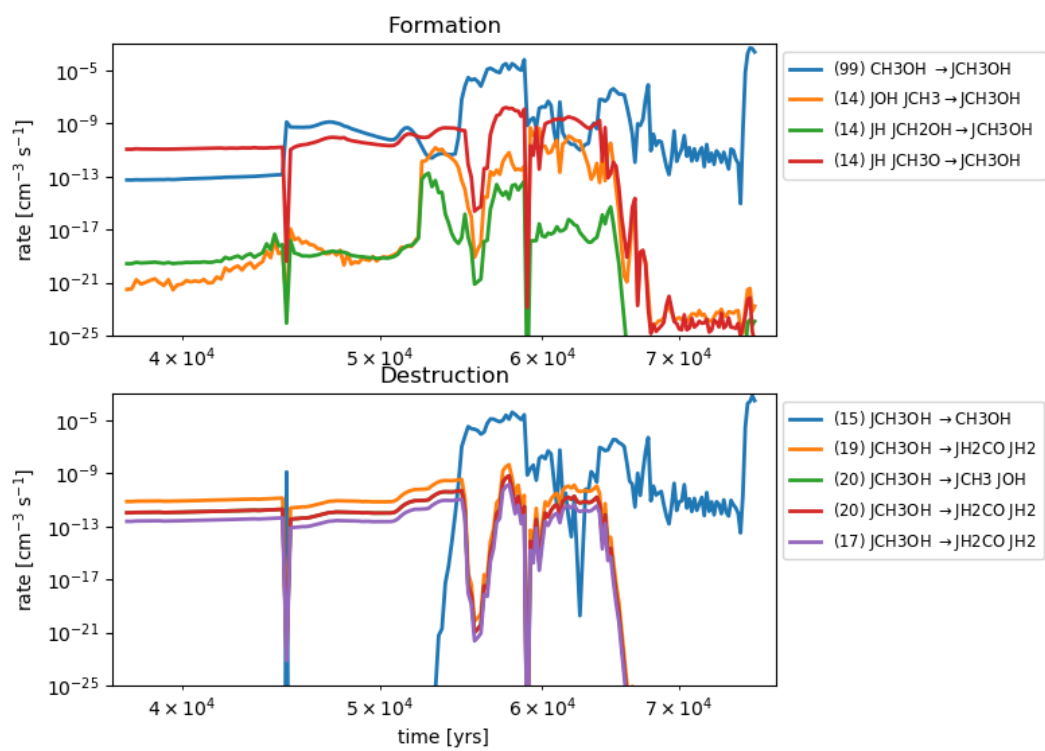


Figure 38: Methanol formation (top) and destruction (bottom) rates on dust grains for one example particle, produced by Saptalizer.

### 4.3.1 Interior

This is the same region as the one in Section 4.2.3, i.e., between 200 and 400 AU with the same 3 linearly spaced radial bins. Figure 39 shows the distribution of abundance of methanol in the most inner ring between radii 200 and 266 AU and between the first and second flares. In this figure I plot a violin plot for every time step.

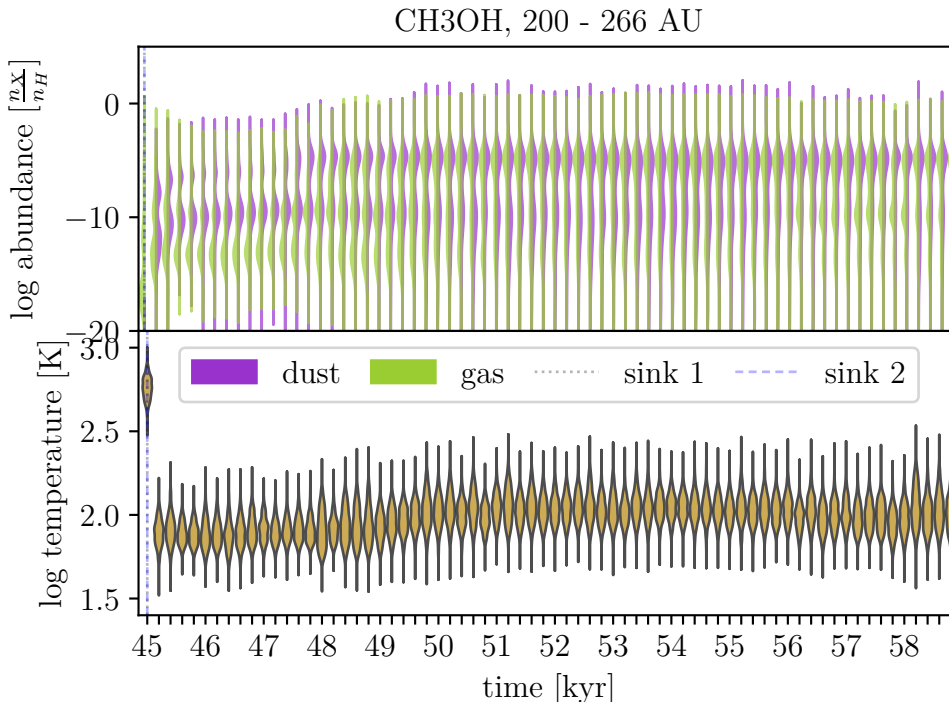


Figure 39: Distribution of methanol abundance for every snapshot (every 200 yr) between the first and second flares at 45.4 and 59.4 kyr (upper panel) for dust and gas between the radii 200 and 266 AU. (Bottom panel) The temperature distribution of the same radius bin. This plot is the distribution for the most inner ring of Figure 35 between the first and second peak.

The most prominent feature of the Figure 39 is the very big spread. The spread is over 20 orders of magnitude. As it was discussed in the previous section, the inner region is highly dynamic. The variation in density and temperatures are high. As we are close to the protostars and the disk, the temperature and density are high. Higher density means faster chemistry and higher temperature means more gas reaction channels getting activated. More over, particles from varying thermal history move through this region while being accreted. All these factors combined cause the chemistry to be highly inhomogeneous and produce the big spread in the violin plots.

Starting from the first violin plot in Figure 39, which is the one corresponding to the first flare, there is no methanol, neither on dust, nor on gas. Methanol on

dust completely deposits into the gas, as the temperature is above the thermal desorption temperature of methanol. But in high enough temperatures, i.e. temperatures above 500 K, methanol seems to also get destroyed in the gas phase. Moving to the right on the figure, the dust abundance seems to recover fast, but with two components and the gas abundance follows but with a significantly lower abundances. Temperature systematically increases with time, as the protostars accrete more material and become more luminous with time. It is followed by a much higher upper dust abundance and a very complex distribution with multiple peaks in both gas and dust. To understand these complex shapes better, we plot Figure 40, which is the same plot, only for the second flare and with less time resolution. Here I have plotted every 10 snapshots, which allows one to see the complex shape of distribution better.

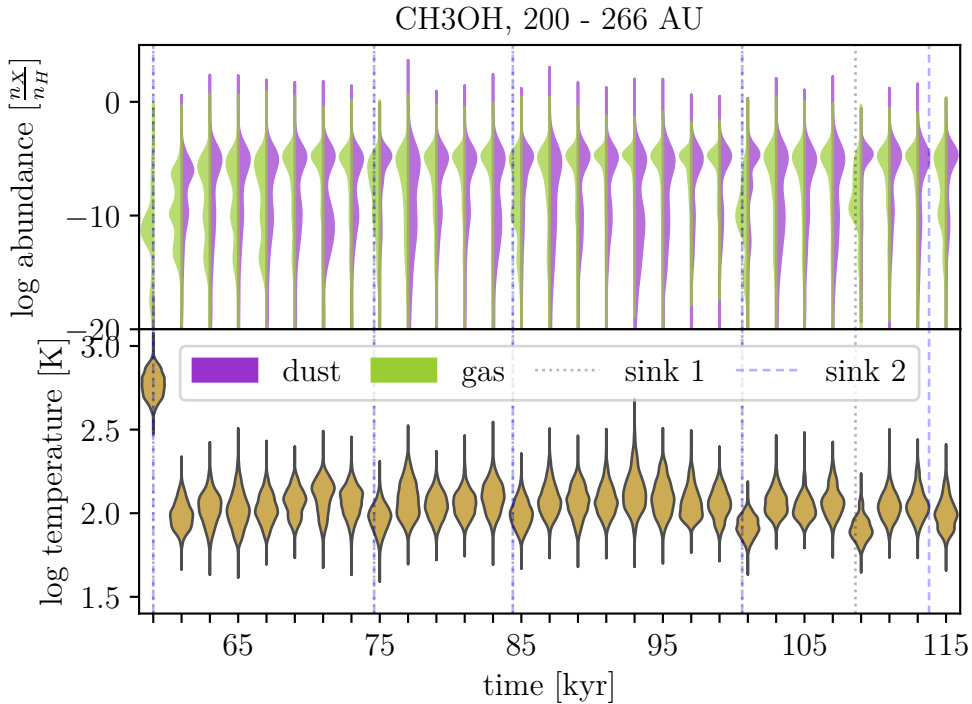


Figure 40: Distribution of methanol abundance for one in every 10 snapshot (every 2 kyr) between the second and third flares at 59.4 and 115.8 kyr (upper panel) for dust and gas between the radii 200 and 266 AU. (Bottom panel) The temperature distribution of the same radius bin. This plot is the distribution for the most inner ring of Figure 35 between the second and third peak. The vertical dashed lines are the accretion events corresponding to the two protostars.

The last violin plot on the Figure 39 shows a high abundance in both gas and dust. Going to the next time step, i.e. the first violin plot in Figure 40, again there is no methanol left on dust and very little on gas. With the time progression, both gas and dust have very complex and multi-component distribution. It shows

clearly that using mean is not a proper way of representing the chemistry in this region.

To look at the behavior of chemistry, I picked particles whose temperatures exceed 500 K during the second flare, losing their methanol content in both gas and dust, remain in the same region after the flare, and regain temperatures above 100 K. Then I use Saptalizer (see Section 4.3) and look at the production and destruction rates of reactions producing and destroying methanol on gas and dust. I follow the most important reactions, and the main reactants and repeat. This way I build a chemistry network for production or destruction of methanol in different points in time. Figure 41 shows such chemical network for the moment of flare in these close radii as temperatures reach above 500 K.

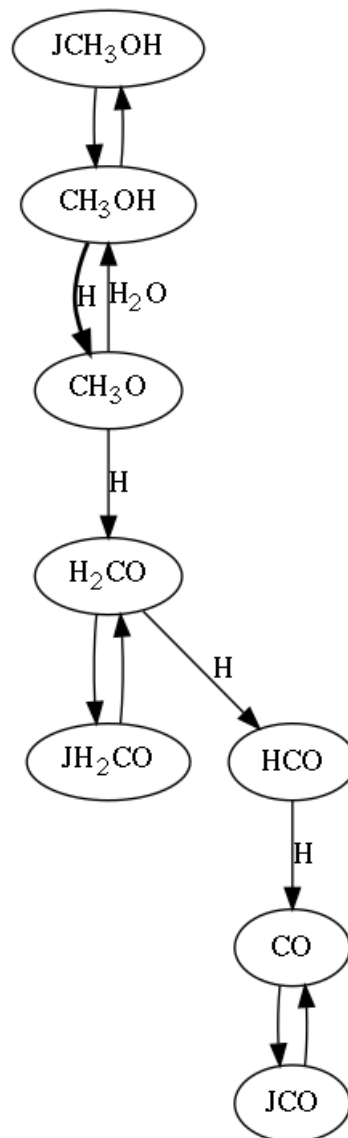


Figure 41: Methanol chemistry on the second flare, for material in temperatures above 500 K, which is losing its dust and gas abundance. J as prefix of chemical species specifies the dust content.

As it is demonstrated in Figure 41 Methanol evaporates into the gas phase and then it gets destroyed by reacting with atomic Hydrogen. The product,  $\text{CH}_3\text{O}$ , is a radical and is quickly hydrogenated and produces formaldehyde ( $\text{H}_2\text{CO}$ ). The chain of hydrogenation continues and results in production of hydrogen carbonate ( $\text{HCO}$ ) and finally carbon monoxide ( $\text{CO}$ ).

If after the flare the temperatures remain above 100 K, the methanol content will never be recovered. However, there are particles whose temperatures drop to below but still close to 100 K and can rebuild their methanol content on dust. Figure 42 shows The chemical network of such material.

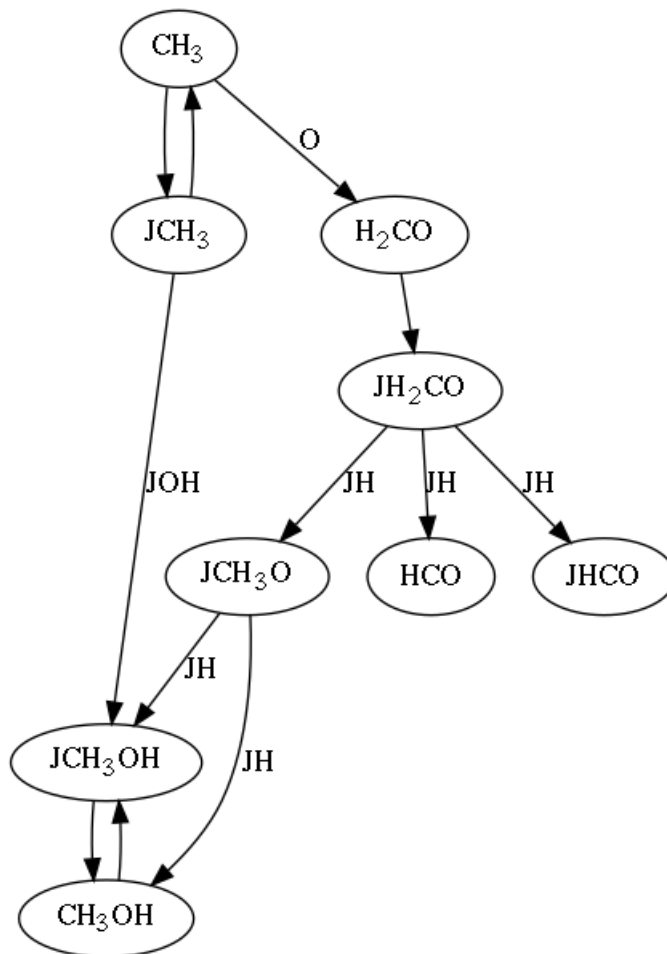


Figure 42: Methanol chemistry right after the second flare, for material which have already lost their methanol content in both gas and dust and have temperatures around 80 K and are rebuilding methanol on dust. J as prefix of chemical species specifies the dust content.

The plot shows how methanol is again built on dust.  $\text{CH}_3$  produces methanol on dust via two different routes. It can either condensate on the dust and react with OH on the dust and produces methanol. Or it reacts with oxygen and produces formaldehyde, which in turn freezes out onto the dust and gets hydrogenated repeatedly to produce  $\text{CH}_3\text{O}$  and finally methanol on both gas and dust.

The other competing reactions for this route are the production of HCO in both gas and dust phase. These two are rather slow channels. If this material continues its infall trajectory, it will go through another thermal desorption and the dust content will be deposited into the gas phase. This is typically not a stable state, as the temperature of such particles, on their way of collapsing into the protostars, will systematically increase and will eventually reach above 500 K and its methanol is destroyed completely through the same process, shown in Figure 41, i.e. destroyed by reacting with atomic hydrogen and producing CO in a repeated hydrogenation chain. More over since the time scales in which particles reside below 100 K in these close regions to the protostars are short, there is simply not enough time for methanol to be produced in high abundances, such that the methanol abundance can never reach above  $10^{-6}$ .

One can poses the question, if the gas and dust abundance is fully destroyed, and part of it is never restored or not fully restored, how do we see the upper peaks in Figure 40? The answer lies in how dynamic this region is and how material is quickly falls into these radii and then leaves the region and fall into the protostars. So methanol rich material keeps pouring in from the outer regions. This is a unique feature of having a fully dynamic physical model, as it can deal with mixing and movement of the material with different thermal histories. It results in a very inhomogeneous chemistry in the interior region. Figure 43 shows the mass ratio of infalling methanol rich material to the total mass between the radii 200 and 266 AU.

On Figure 43 the starting point is the second flare and the mass ratio of methanol rich infalling material is almost zero. As the time passes the ratio increases quickly and only after 10 kyrs over 60 percent of the material in this radius bin is methanol rich material which comes from outer regions, i.e, material which were far enough that it could be enriched by accretion heating during the second flare (see Section 4.3.2) and has travelled inwards toward the protostars. This remains consistent throughout this time interval except for several points where there is a sudden drop in the enriched material and then it resumes. These points of minima coincide with the unresolved accretion events, which are shown by vertical dashed lines(see Figure 30 and Section 4.2.1). Even though we do not resolve the accretion on these points, the outflows are launched and they drag the material outward, which then causes in these sudden drops in the plot. Hence at these points the chemical effects of outflow is disentangled from the accretion events, as outflows dynamically affect the mixing and radial movement of the material, whereas the episodic accretion affects the heating and energy budget of the material in the proto-stellar core. These unresolved accretion events also reflect on the violin plots with a visible decrease in temperature (Figure 40).

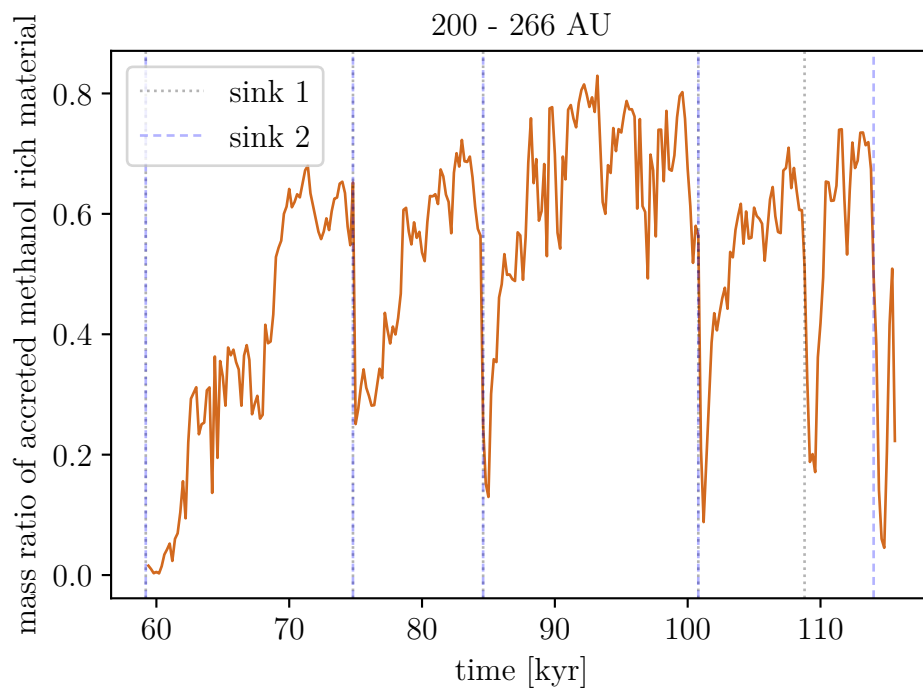


Figure 43: The mass ratio of the material with methanol abundance higher than  $10^{-6}$  between 200 and 266 AU radii, which were at larger radii at the moment of the second flare to the total mass in the same radii. The time interval is between the second and the third flare. This is the same time interval and radius bin as Figure 40 between the second and third peak and it is calculated for every time step. The vertical dashed lines are the accretion events corresponding to the two protostars.

Another possible contributor to the big spread of the methanol abundance, is local density variability. Variation of density could affect local visual extinction, hence affect heating via radiation. I calculate the temperature via RADMC3D (Section 3.2.3), so local density variation can cause local temperature variation, which in turn affect the chemistry. As it was mentioned in the previous Section (4.2.3) higher densities in the interior region means shorter mean free path between the molecules, which results in more collision and makes the chemistry faster. So to sum up, in this region, the gas is highly dynamic, temperature and density are high and they vary a lot, hence, the chemistry is far from equilibrium and homogeneity and it all result in a spread of over 20 orders of magnitude for the abundance of methanol.

Figure 44 shows the distribution of methanol for the same region as Figures 39 and 44, only after the third flare, where every time step is plotted as a violin plot.

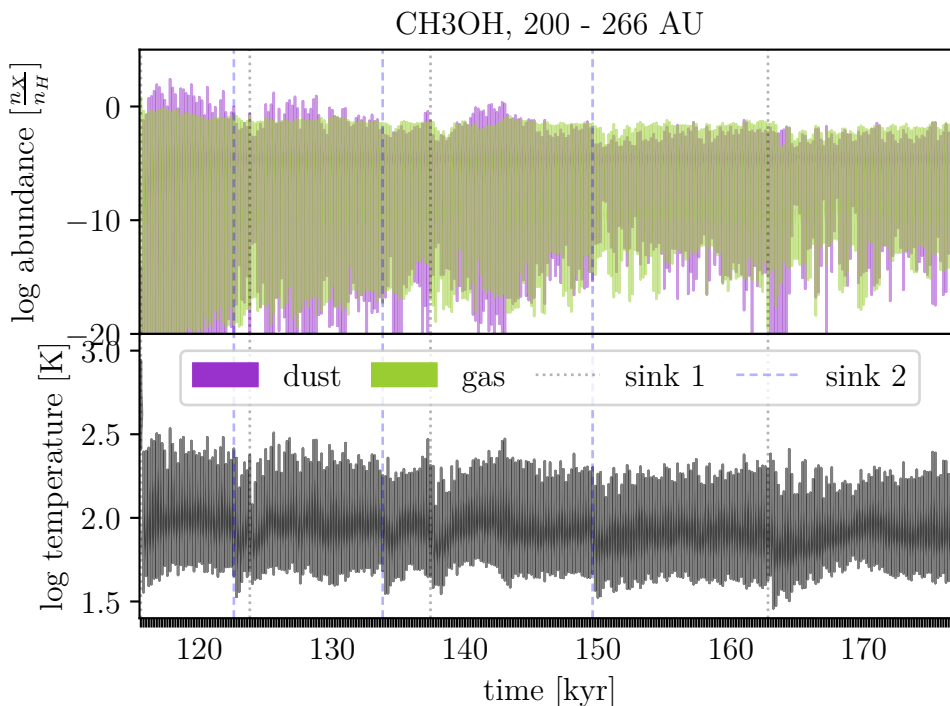


Figure 44: Distribution of methanol abundance for every snapshot (every 200 yr) from the third flare until the end of simulation at 115.8 and 177.8 kyr (upper panel) for dust and gas between the radii 200 and 266 AU. (Bottom panel) The temperature distribution of the same radius bin. This plot is the distribution for the most inner ring of Figure 35 after the third peak. The vertical dashed lines are the accretion events corresponding to the two protostars.

Even though this type of plot is too busy to see any details, the general behavior is more easily demonstrated. The dips in temperature also appear here always

right after every unresolved accretion event. As expected they also reflect in the average temperatures (Figure 36). It also seems that not only the peak temperature decreases, but also the temperature spread becomes smaller. Distribution of methanol abundance in dust follows these temperature features by becoming more compact, while it seems that the distribution of methanol abundance in gas becomes bigger. Since this is an effect caused by the temporal resolution, it is not straight forward to understand what exactly cause them. I discuss the possible sources of these temperature drops in Section 4.2.1.

Comparing the three different plots of the distribution after each flare (Figures 39, 40 and 44), one can see that with time the spread decreases systematically. As time goes by the accretion events become less prominent. In Figure 30, not only the accreted mass becomes less with time, but also two sinks become out of sync. This causes the effect of the flares to decrease with time. In Figures 29, 33 and 36 the temperature peak corresponding to the third flare is lower than the first two. This is also reflected in the bottom panel of the violin plots, the temperature in the third flare is less than the other two. As the accretion become less violent, the disk and its surrounding material become more stable, hence the spread decreases with time.

### 4.3.2 Mid-range

This is the same region as the one in Section 4.2.1, i.e, between 400 and 3000 AU radius with the same 6 linearly spaced radial bins. Figure 45 shows the distribution of abundance of methanol between radii 400 and 833 AU between the first and second flares. In this Figure I plot a violin plot for every time step.

Following the same format as the previous section, I proceed with a plot of the same region (Figure 46) for the time interval between the second and third flares and one violin plot in every 2 kyr.

Finally I make one for the same region and after the third flare (Figure 47), where I plot a violin plot for every snapshot.

Comparing these plots with their corresponding ones from the interior (Section 4.3.1), spread is systematically smaller by a few orders of magnitude and the distribution is more narrow. The same goes for temperature distribution, even though it is a bigger region in size. The further we go from the protostars, less dynamic becomes the gas, so the temperature and hence the abundance variations become smaller. On the point of the flare, the entire methanol is in the gas phase with peak around  $10^{-4}$  and the abundance on dust is negligible, as the temperatures reach between 200 and 300 K. Right after the flare, the temperatures drop fairly below 100 K and the dust abundance starts to build. At a lower pace gas abundance distribution starts becoming increasingly broader and after

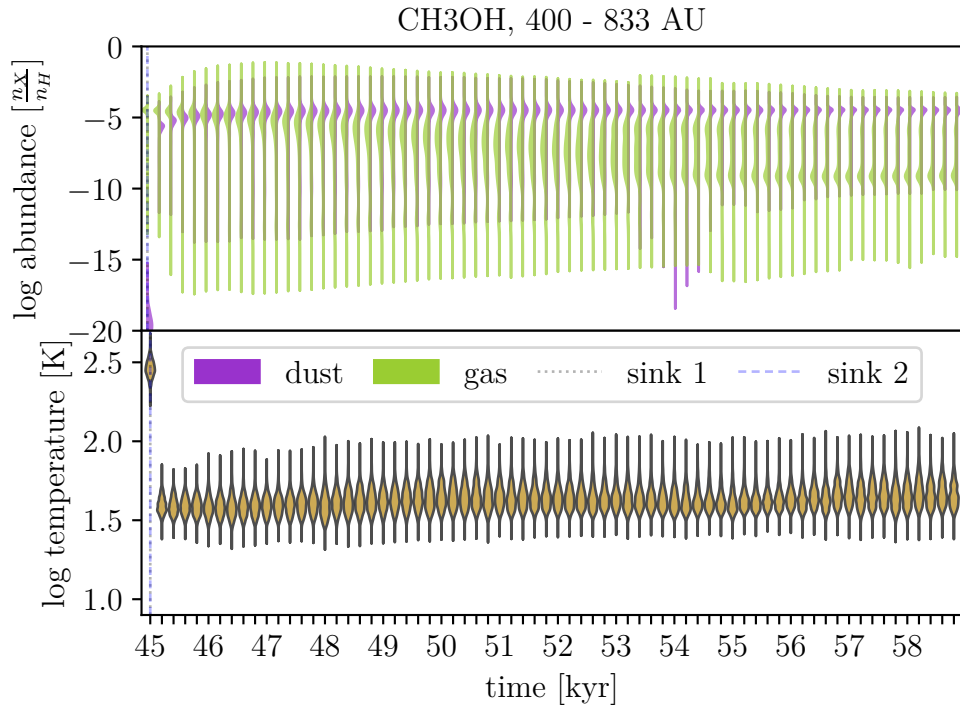


Figure 45: distribution of methanol abundance for every snapshot (every 200 yr) between the first and second flares at 45.4 and 59.4 kyr upper panel) for dust and gas between the radii 400 and 833 AU. (Bottom panel) is the temperature distribution of the same radius bin. This plot is the distribution for the most inner ring of Figure 28. The vertical dashed lines are the accretion events corresponding to the two protostars.

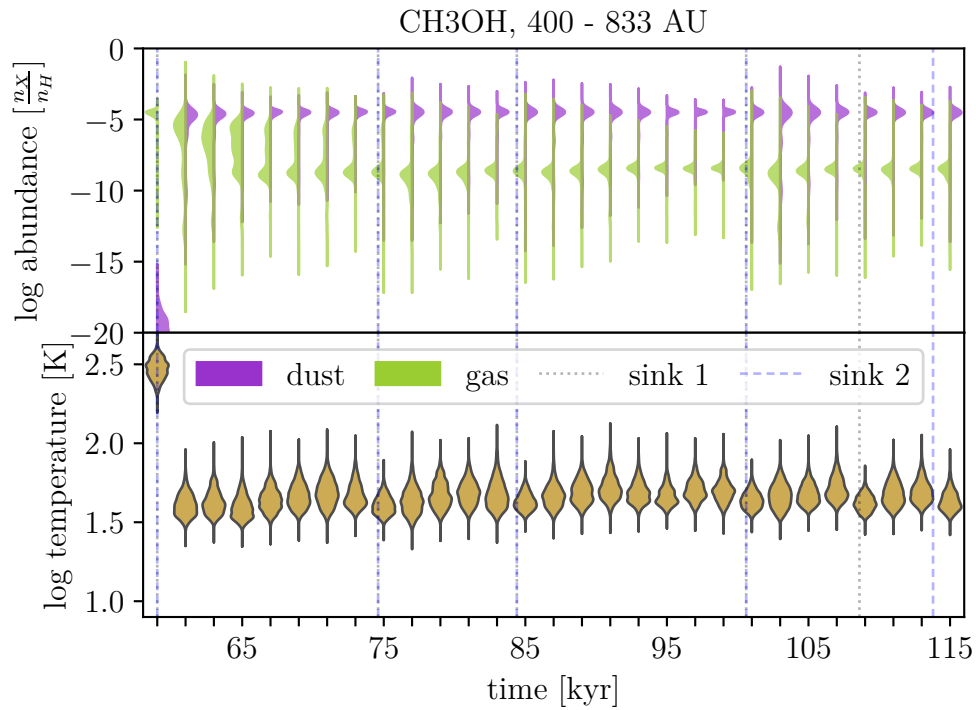


Figure 46: distribution of methanol abundance for one in every 10 snapshot (every 2 kyr) between the second and third flares at 45.4 and 59.4 kyr (upper panel) for dust and gas between the radii 400 and 833 AU. (Bottom panel) is the temperature distribution of the same radius bin. This plot is the distribution for the most inner ring of Figure 28. The vertical dashed lines are the accretion events corresponding to the two protostars.

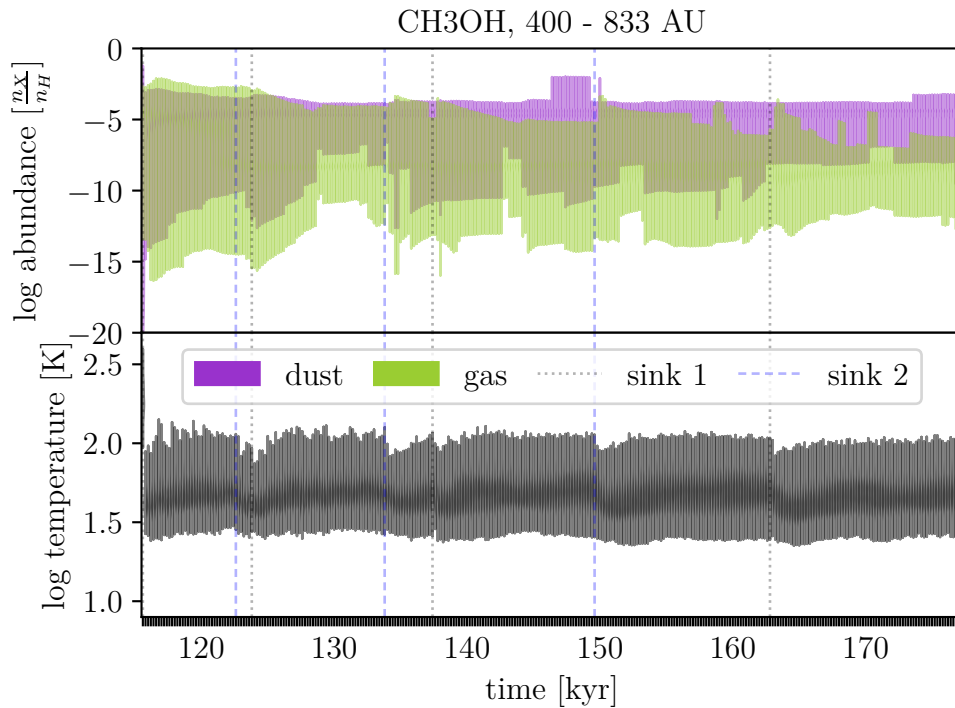


Figure 47: distribution of methanol abundance for every snapshot (every 200 yr) between the second and third flares at 45.4 and 59.4 kyr (upper panel) for dust and gas between the radii 400 and 833 AU. (Bottom panel) is the temperature distribution of the same radius bin. This plot is the distribution for the most inner ring of Figure 28. The vertical dashed lines are the accretion events corresponding to the two protostars.

about 10 kyr it turns into a very distinct double peak, with two peaks around  $10^{-6}$  and  $10^{-9}$ . The the upper peak fades with time within few kilo years, until the distribution becomes narrow again with only the lower peak present, but still with a long tail toward higher abundances.

The distribution becomes systematically narrower with time (Figure 47) as the system stabilizes dynamically; meaning the accretion mass becomes smaller and the accretion events for two protostars become unsynchronized (Figure 30). The unresolved flares still cause similar decrease in temperature as in inner region (Figure 44), but since the temperature is well below the thermal desorption levels, it does not affect the abundances, except for making the tail of the distribution wider.

Same as in the previous section, I use Saptalizer (see Section2) to look at the reaction rates to understand how chemistry is affected by the physical condition of the system. On The flare the only dominant reaction is thermal desorption (Figure 48).

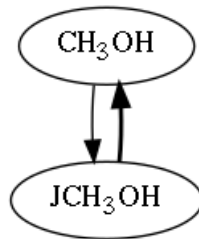


Figure 48: Methanol chemistry on the flare, for material in temperatures between 200 and 500 K, which is losing its dust and gas abundance due to thermal desorption. J as prefix of chemical species specifies the dust content

I show the reaction channels which become active right after the flare and contribute to the production of methanol on dust in Figure 49. Right after the flare, with drop of temperature, thermal desorption rate drops to negligible values and the methanol in the gas freezes out onto the dust and this is the main contributor of methanol abundance on dust, with rates of the order of  $10^{-10} \text{ cm}^{-3} \text{ s}^{-1}$ . The other important process is the hydrogenation of  $\text{CH}_3\text{O}$ . This reaction is completely removed during the flare, but returns to values of the order of  $10^{-11} \text{ cm}^{-3} \text{ s}^{-1}$  very fast.

This channel is a chain of reaction starting from the freeze out of CO, which quickly goes through multiple hydrogenation on dust and produces hydrogencarbonate ( $\text{HCO}$ ) and formaldehyde ( $\text{H}_2\text{CO}$ ) along the way. The main competitor for this chain is the production of  $\text{CO}_2$  on the dust. These rates remain similar as long as the material is in this temperature range. When the material moves closer and closer to the protostars, its temperature will increase high enough for thermal

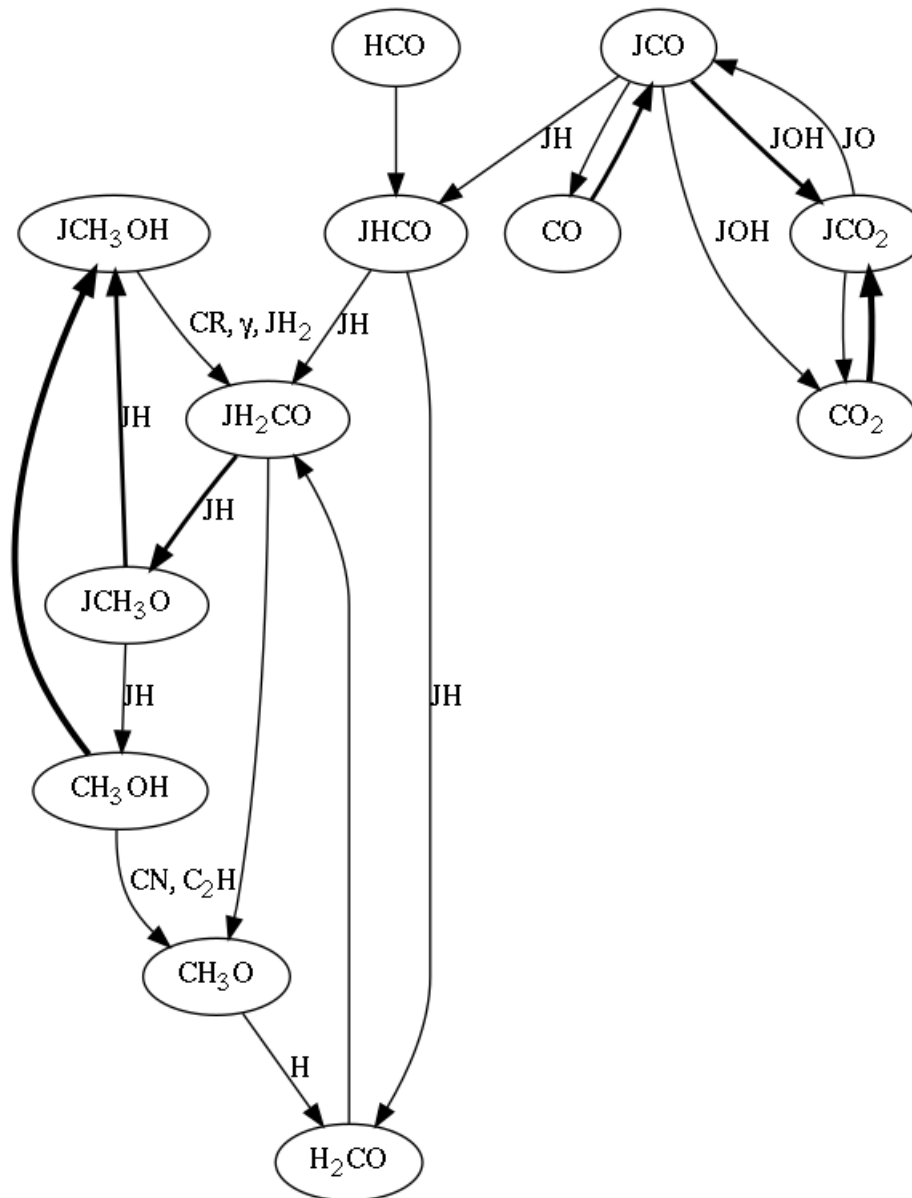


Figure 49: Methanol chemistry right after the flare, for material which has been heated up between 200 and 500 K, has lost its dust methanol content during the flare due to thermal desorption and now has cooled down to around 30 K and is rebuilding methanol on dust. J as prefix of chemical species specifies the dust content.

Species	$E_b$ [K]
H	650
CO	1300
H <sub>2</sub> CO	1600
OH	4600
CH <sub>3</sub> OH	5000
CH <sub>3</sub>	1600
H <sub>2</sub> O	5600
CH <sub>3</sub> O	4400
HCO	2400

Table 4: The binding energy of different species to ice layers on the dust.

desorption, independent of the flares and eventually reaches high enough temperatures for the gas channels to become active and for methanol to be destroyed on both gas and dust (see Section 4.3.1).

It is noteworthy that the production of formaldehyde in this regime is different than the one in the interior (Figure 42). Whereas in temperatures slightly under 100 K, H<sub>2</sub>CO on dust is mainly produced by condensation from the gas, in temperatures around 30 K, it is mainly produced by hydrogenation of CO on the dust. To understand why these production channels are so completely different in these different temperature regime, we need to look at the binding energies of the different relevant species to the dust. The sublimation rate coefficient is given by

$$k_{des} = \nu \exp \frac{-E_b}{kT}, \quad (21)$$

where  $\nu$  is the vibrational frequency of a certain species on the grain surface,  $E_b$  is the binding energy of that species to the surface,  $k$  is the Boltzmann constant and  $T$  is the desorption temperature. We can rewrite this formula in terms of residence time of a species on the dust grain as

$$\tau_{des} = \nu^{-1} \exp \frac{E_b}{kT}. \quad (22)$$

From these equations one sees that the desorption temperature is a function of both binding energy and time scale. For example the relevant time scale in a laboratory is of the order of seconds and the temperatures in which desorption starts is much higher than desorption in interstellar medium where relevant time scales are, in case of our simulations, of the order of hundreds of years. Table 4 shows the binding energies of different species in kelvin.

From Table 4 one sees that CO, whose condensation is the onset of the production of methanol in low temperatures (around 30 K), has a smaller binding

energy than  $\text{H}_2\text{CO}$  and  $\text{CH}_3$ , who are responsible for the production of methanol on the dust in warmer temperatures (around 80 K). However since we have a very low Hydrogen budget on the grain at these temperatures the latter two result in a much slower route in comparison. Figure 50 shows the desorption time as a function of dust temperature for different species.

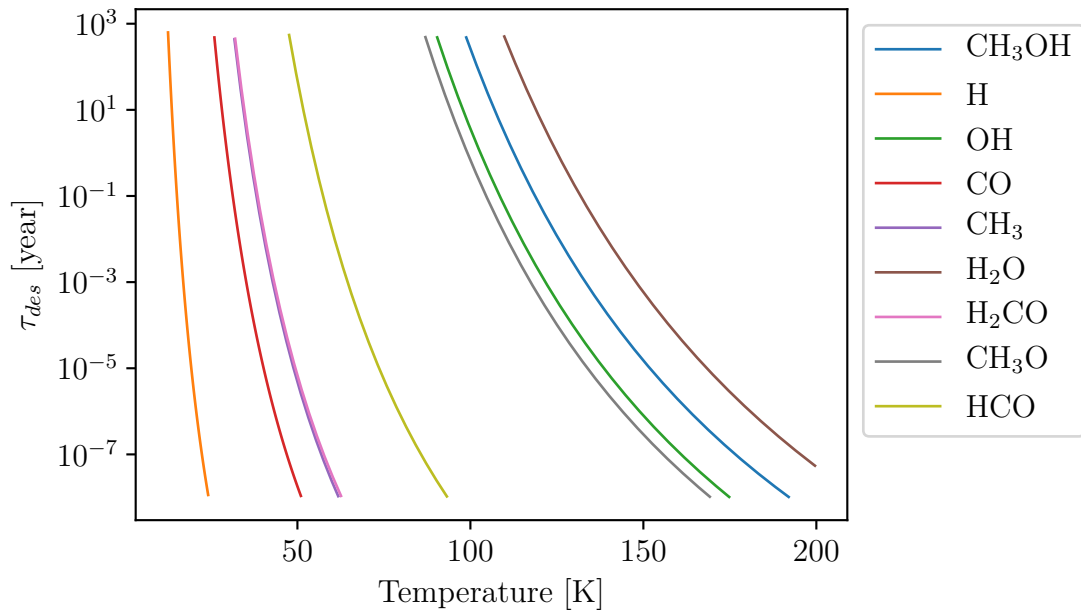


Figure 50: Comparison of the desorption time of different species as a function of dust temperature

### 4.3.3 Exterior

This is the same region as the one in Section 4.2.2, i.e. between 3000 and 10 000 AU, with the same 5 linearly spaced radial bins. I plot the distribution of methanol abundance in gas and dust, as well as temperature distribution for a radial bin between 8600 and 10 000 AU in Figure 51. Here I have plotted 1 violin plot for every time step between the first and second flares.

Similar to the previous two sections, I make the same plot for the time interval between the second and the third flare, with one violin plot for every 10 snapshot (Figure 52); and another for the time interval after the third flare, with one violin plot for every snapshot (Figure 53).

The spread of the methanol abundance is significantly smaller than the more inner regions, as are the temperatures. Except that there is a long tail toward higher temperatures with a very small second peak.

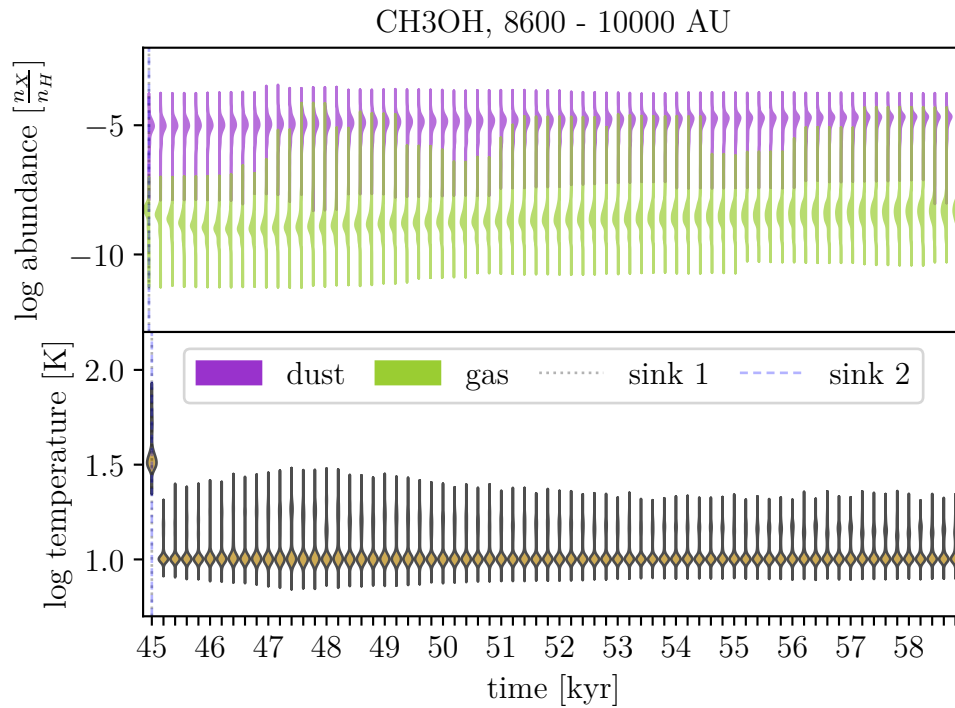


Figure 51: distribution of methanol abundance for every snapshot (every 200 yr) between the first and second flares at 45.4 and 59.4 kyr (upper panel) for dust and gas between the radii 8600 and 10000 AU. (Bottom panel) is the temperature distribution of the same radius bin. The vertical dashed lines are the accretion events corresponding to the two protostars.

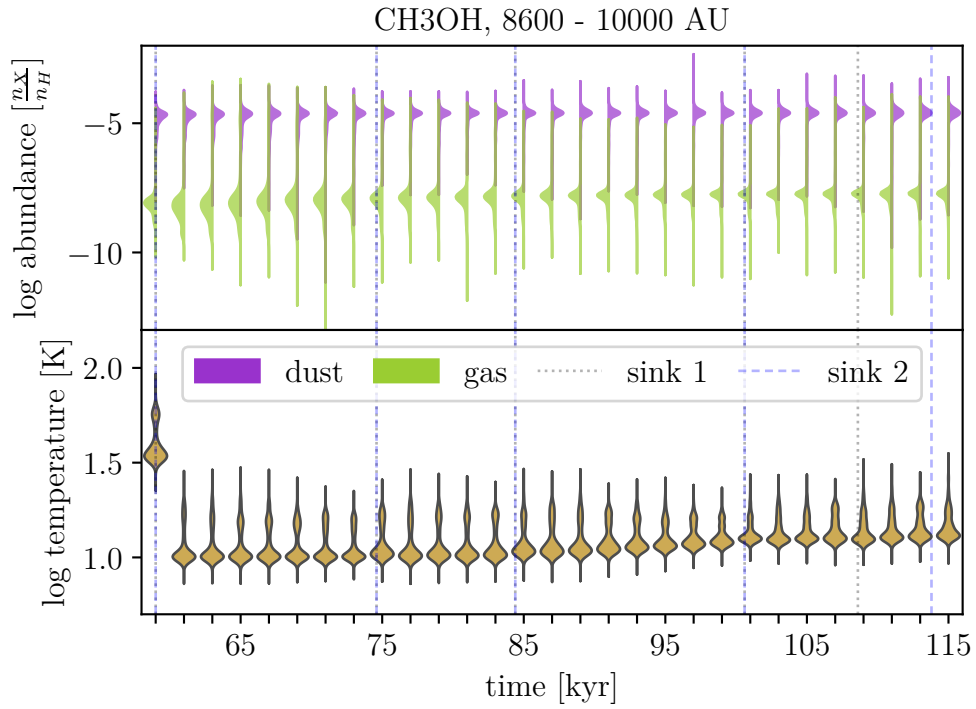


Figure 52: distribution of methanol abundance for one in every 10 snapshot (every 2 kyr) between the second and third flares at 45.4 and 59.4 kyr (upper panel) for dust and gas between the radii 8600 and 10000 AU. (Bottom panel) is the temperature distribution of the same radius bin. The vertical dashed lines are the accretion events corresponding to the two protostars.

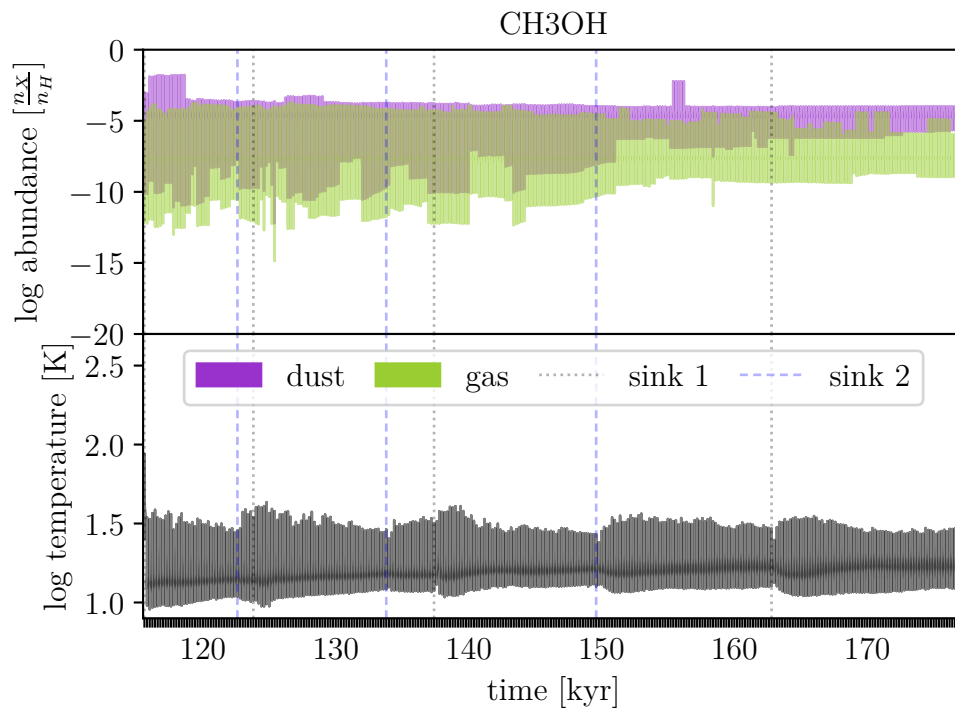


Figure 53: distribution of methanol abundance for every snapshot (every 200 yr) between the second and third flares at 45.4 and 59.4 kyr (upper panel) for dust and gas between the radii 8600 and 10000 AU. (Bottom panel) is the temperature distribution of the same radius bin. The vertical dashed lines are the accretion events corresponding to the two protostars.

The flares do not affect the methanol abundance in this region. The material here is far enough from the central protostars, that the temperature can only increase to 30 to 40 K during a flare, well below desorption temperatures. There is a broadening of methanol and a skewed tail toward higher abundances (up to  $10^{-4}$ ) in gas, which is not reflected into any change in dust abundance, which appears with some delay (between 1 to 5 kyr) after the second flare (Figure 52). As it was discussed in Section 4.2.2, this is reflected in the average very prominently (Figures 32 and 25). It could indicate that methanol rich material is migrating from inner regions to outer regions. To investigate this, I find the particles with gas abundances higher than  $5.0e^{-6}$ , between 8600 and 10000 AU for each snapshot after the second flare, which were at a radii less than 3000 AU on the second flare. I plot the ratio of these particles to the total number of particles in that region (Figure 54).

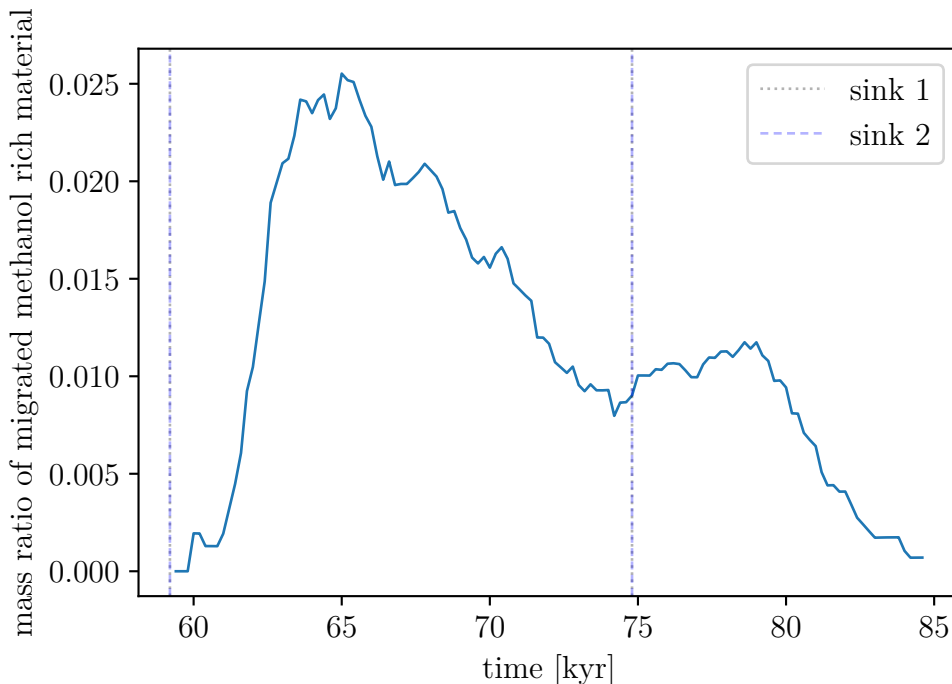


Figure 54: Mass ratio of migrated methanol rich material. These are the ratio of the number of particles with gas abundance higher than  $5.0e^{-6}$ , between 8600 and 10000 AU which were at a radii less than 3000 AU on the second flare, to the total particles in this region. The vertical dashed lines are the accretion events corresponding to the two protostars.

Since SPH particles have the same mass, the number ratio of particles gives us mass ratio. The plot indicates that there is an outflow of methanol rich material right after a flare. There is a second, much smaller peak which seems to be correlated with the next accretion event. Since this is an unresolved accretion event, there is no enrichment of methanol, which indicates that these are correlated with

outflows which are launched at the same time as I plot the trajectory of these particles and their abundances in Figures 55 and 56.

In this study I do not take the outflow particles themselves into account and they are omitted from the sampling (Section 3.1). Remembering this, Figures 55 and 56 show that these are material entrained by the outflow. They have converging densities and even more pronounced temperature trajectories, which reflects in their converging abundances. These are material, which are infalling in close orbits to the protostars, where they are heated up through a flare and obtain high methanol abundance in gas phase. Then as their trajectory collides with the outflow, which was launched at the same time as the flare, they are dragged outwards to very cold regions. This process enriches methanol in larger radii. It is noteworthy that this phenomena can only happen with a dynamic and non-symmetrical modeling of chemistry, which allows radial movement of material to mix material and affect chemistry.

These kinds of mixing are non-symmetrical and dynamic effects, both here and in inner region due to infall. They would be ignored in a symmetrical analysis, i.e. averaging in radial bins. To see these effects better I plot all the sampled SPH particles in 3D and use color map to show the abundance of each SPH particle. Figure 57 shows the 3D distribution of methanol abundance in three consequent time steps; before the first flare, on the first flare and right after it.

Before the flare all the methanol is in the dust, except for the very center, really close to the protostars, where methanol is efficiently destroyed. On the flare, methanol has deposited onto the gas within a certain radius and after the flare the dust has already started to retrieve its methanol content, whereas there are still a lot of methanol in the gas phase. This is all consistent with my analysis from previous sections (Sections 4.3.1 and 4.3.2).

To see the entrained material, I make a similar plot for the time step where the enrichment is the highest after the second flare, i.e. for the peak of the Figure 54, at 66 kyr into the simulation (Figure 58). On the left panel the red dots, which correspond to the material with high methanol abundance in gas phase, are visible all along the outflow cone.

Since I do not resolve most of the accretion events, the enrichment is highly underestimated. Future work should address this issue by better time resolution of accretion events, which I expect to lead to higher enrichment of the outer region.

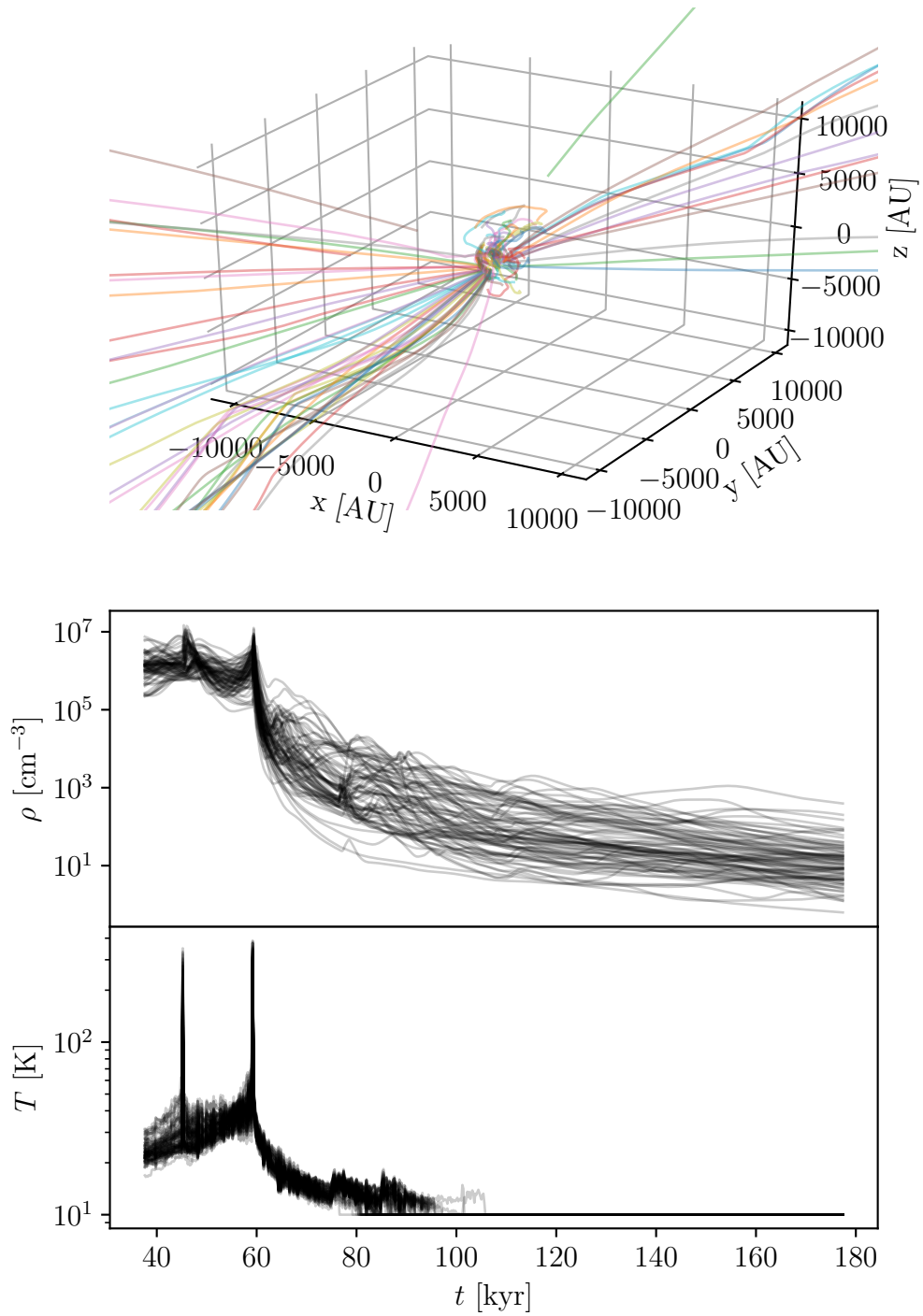


Figure 55: Trajectories (upper panel) and the densities (middle panel) and the temperatures (bottom panel) of the entrained particles. These are particles with gas abundances higher than  $5.0e^{-6}$ , between 8600 and 10000 AU which were at a radii less than 3000 AU on the second flare at the peak of Figure 54.

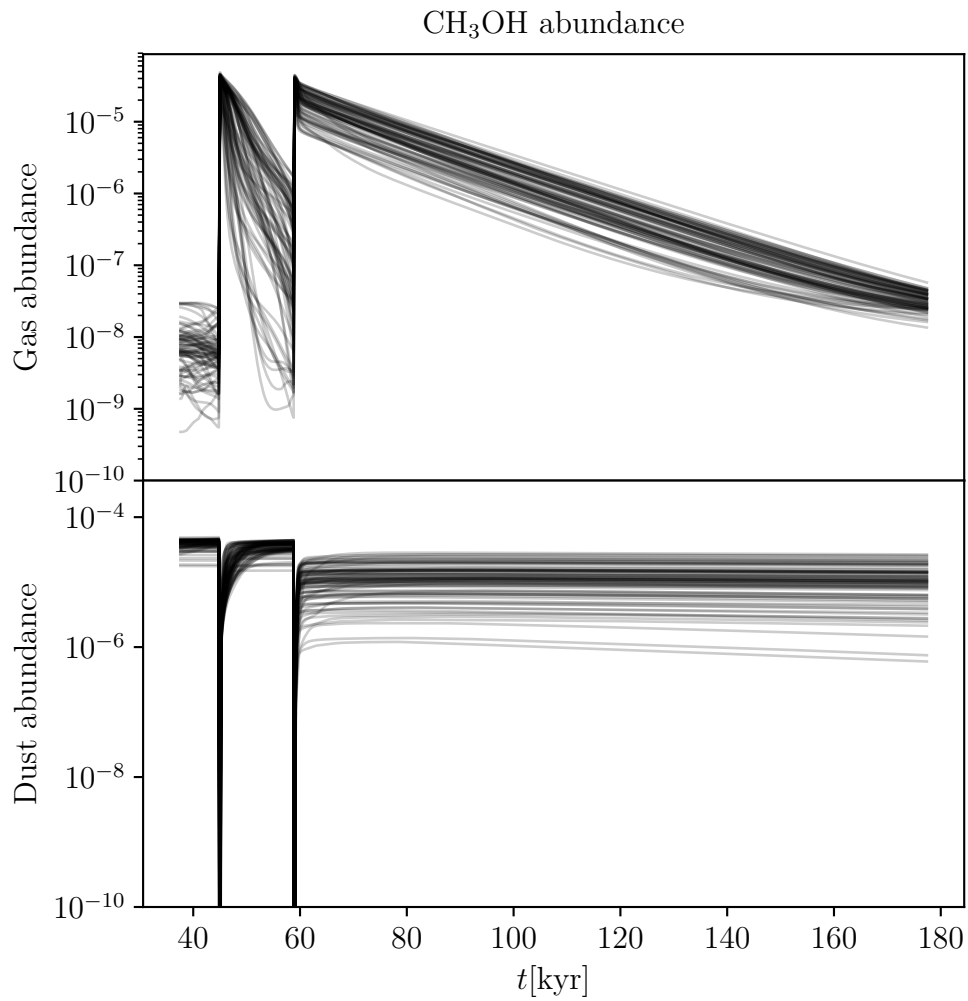


Figure 56: The gas (upper panel) and dust (bottom panel) abundances of methanol for entrained particles. These are particles with gas abundances higher than  $5.0e^{-6}$ , between 8600 and 10000 AU which were at a radii less than 3000 AU on the second flare at the peak of Figure 54.

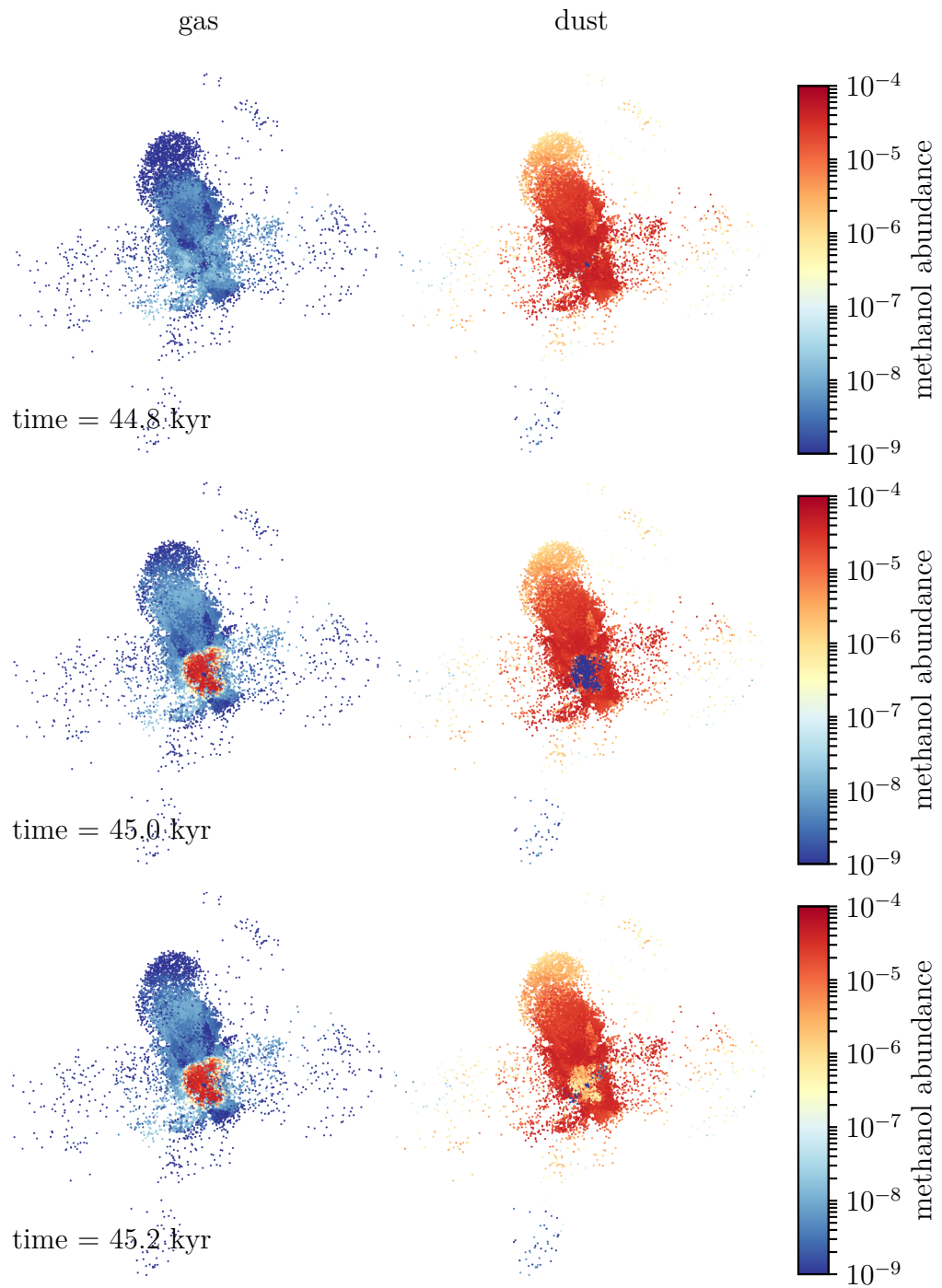


Figure 57: Methanol abundance on gas (left) and dust (right) of the SPH particles, in snapshots right before the first flare (top), on the first flare (middle) and right after the first flare (bottom).

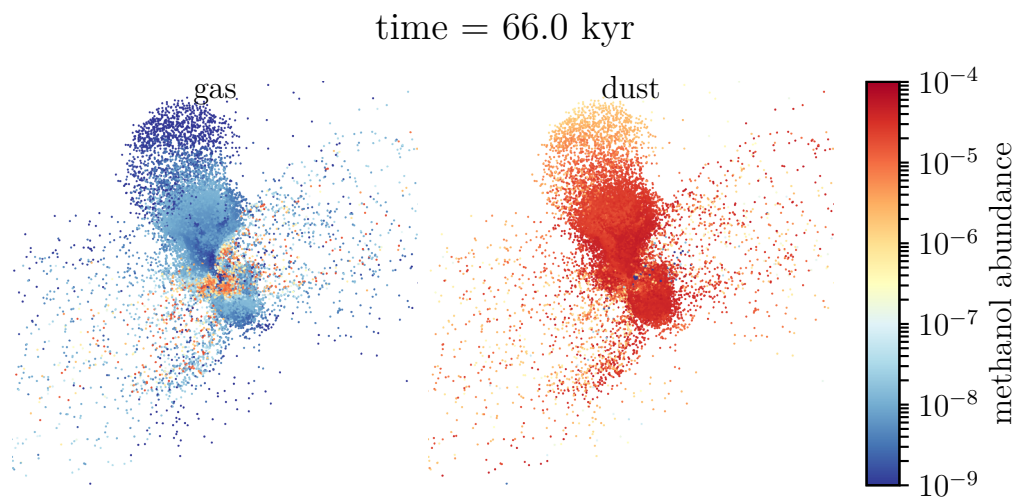


Figure 58: Methanol abundance on gas (left) and dust (right) of the SPH particles for the snapshot with the highest enrichment of methanol in outer region.

## 5 Conclusion and outlook

### 5.1 Summary

In this work I present dynamic modeling of chemistry, via the post-processing hydrodynamic simulations with chemistry simulations. The hydrodynamic simulation I use is an SPH simulation of a core collapse, which includes episodic accretion scenario and episodic outflow feedback, as well as a self consistent protostar evolution model. I select a representative subset of the gas within the 10 000 AU of the central binary objects by sampling the SPH particles and follow them throughout the simulation and track their physical properties, i.e. their trajectories and the density along their trajectories during the collapse. I calculate their temperatures, using a radiative transfer code RADMC-3D and the protostar luminosity and dust densities from the hydrodynamic simulation. I use the reaction rate chemistry code Saptarsy to post process this data. I use a chemical network with 185 species and run a model which includes gas reaction, dust surface reactions, gas-dust interactions and a multi-layered dust model. I run one chemistry simulation for each particle, using the temperature and density of each particle as inputs. The results are the time evolution of abundances of different species present in the chemical network along the trajectory of each particle in a time interval of 140 kyr, which covers the time shortly after the birth of protostars to near dissipation of the envelope.

I find that the highly non-linear dynamic of the core collapse, specifically the episodic accretion and outflows have a non-linear effect on chemistry. Episodic accretion, and the resulting sudden and short-lived ( $\sim 10$  yr) increases in luminosity of the protostar, deposits huge quantities of thermal energy onto the material of the core, causing the dust temperature to increase sharply as well. Different species react differently to these sudden variation of dust temperature. Species, which are mainly produced on dust and buried under ice mantle in low temperatures ( $\sim 30$  K), such as methanol, water, ammonia, etc, desorb thermally into the gas phase instantly, thus increasing the gas abundance by nearly 4 orders of magnitude. Then they slowly freeze back out onto the dust, such that during 1 to 10 kyrs after an accretion event, the abundances in the gas phase remain high. Some other species such as  $\text{H}_2\text{S}$  and  $\text{SO}$  retain their abundances from before the accretion event almost instantaneously. Therefore, one can speak of "chemical memory", i.e. some species have a chemical memory of the thermal history of the system and some do not. Meaning, the recent thermal history of the system is imprinted in the relative abundances of a set of chemical species.

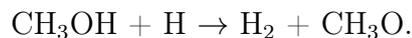
Methanol is the smallest and simplest of the iCOM and is a precursor molecule that through a series of reactions produces a wide selection of more complex

iCOMs. Methanol is observed in cold cores, yet most existing chemical models systematically under-produce it in these objects. I show that episodic accretion can be a candidate for producing methanol in cold gas, as it lingers beyond the duration of accretion events and desorbs again with a new accretion event, before it completely freezes out onto the dust.

Looking at the spatial and temporal distribution of methanol, I find that the production of cold methanol is confined into a region between  $\sim 500$  and  $\sim 3000$  AU, or the inner part of the envelope. Closer to the central protostars, methanol in warm gas is released and maintained due to the proximity to the source of luminosity without the aid of accretion heating, and is destroyed during the flares, via gas reactions. Further outside of this region, the increase in temperature during the accretion events is not high enough for the thermal desorption to happen. However, methanol rich material from the middle region are dragged by the outflows and are transported to larger radii.

The spread of the abundance, or in other words, the inhomogeneity of chemistry increases systematically with decreasing radius. The closer to the disk, the more dynamic is the gas, i.e. dynamic timescales are small. Particles with different histories all end up in the same region due to infall. Moreover, the higher the density the smaller is the mean free path between molecules, leading to faster gas phase reactions. These results in a highly chemically inhomogeneous regions close to the protostars with spreads of around 10 orders of magnitude or higher. This could result in high degree of diversity in observations of protostellar cores.

The main contributor to methanol in gas phase is thermal desorption consistently, while its destruction depends on temperature. Methanol gets efficiently destroyed in the gas phase in temperatures above 500 K (during flares in interior region or right before an SPH particle falls into the sink) via the reaction:



$\text{CH}_3\text{O}$  is a radical, hence highly reactive and reacts with atomic hydrogen and produces formaldehyde. The chain of hydrogen reaction continues and contributes to CO production in the gas phase. In lower temperatures, methanol is removed from the gas phase by freezing out onto the dust.

The production routes of methanol on the dust after a flare also depends on temperature. In inner region, where the dust temperature is  $\sim 80$  K between outbursts, the main route of production, beside direct freezing out, is from freeze out of formaldehyde and repeated hydrogenation on on the dust to produce methanol. However, further away, where dust cools down to  $\sim 30$  K, it is carbon monoxide which condensates on the dust and goes through hydrogenation chain to produce

methanol on dust. The difference is due to low desorption temperature of CO, which makes it absent on dust in lukewarm regions.

The production of methanol in the gas phase via accretion heating and mixing due to both collapse and entertainment by the outflow, show that dynamics of the gas is essential in modeling chemistry of core collapse.

## 5.2 Outlook

### 5.2.1 Astrochemistry

I show in this work that coupling dynamic to chemical models is essential and without it we ignore important mechanisms in enrichment/reduction of different chemical species in the process of star formation on different scales. As such one can expand this method into other scales. For example whether the methanol enrichment can affect larger structures in the molecular cloud where the core lives in. Or on a smaller scale how does dynamic modeling affect disc chemistry modeling. One can also investigate the chemistry at high mass star forming cores. In different scales, the relevant physical parameters and processes change and as such the physical models, namely the hydrodynamic simulations one use should incorporate those physical processes.

The hydrodynamic simulations I used do not include radiative transfer and I assumed the core to be optically thick and did not take variation of visual extinction into account. However, a more physically realistic model should calculate the local visual extinction. Especially if one wants to understand the chemistry in larger scales, in more diffused gas, where photo-processes become important. Moreover in my simulations I assumed the gas and dust densities to be the same. This is a good assumption as the core densities are high enough for the gas and dust to be collisionally coupled. In densities lower than  $\sim 10^{4.5}\text{cm}^{-3}$ , dust and gas temperature become decoupled (Goldsmith, 2001), hence it is important to have different gas and dust temperatures for chemical reactions happening in dust and gas phase. Saptarsy has the ability to treat dust and gas temperature as two distinct parameters, hence, if the hydrodynamic simulations can treat gas and dust temperatures properly, one can improve on this aspect as well. Slightly higher mass core collapse simulations, resulting in solar-type stars, would improve on this study as one could have a self-consistent physical model without the need to amplify the luminosity. As it was discussed in Section 4.3, these hydrodynamic simulations do not resolve the accretion events which leads to underestimation of the enrichment of methanol. Future studies should consider higher time resolution for the accretion events.

High mass star forming regions are very rich in chemical species, since the

protostars produce enough heating for the ice mantle to evaporate and gas chemistry to become important. However the physics of high mass star formation is less known and the physical processes involved are more complex. Hence hydrodynamic simulations including those processes such as radiative pressure and ionizing radiation should be used.

Saptarsy takes cosmic ray ionization rate as a fixed global parameter. This is an oversimplification which can affect the results. In future works, variable cosmic ray ionization should be included in Saptarsy. X-ray ionization is also neglected in this work. during the accretion events they can have relevance in episodic accretion and the funnel flow of material along the magnetic lines of the protostar, which leaves "hot spots" in density, on the surface of the protostar and producing how amounts of x-ray radiation (Espaillat et al., 2021).

Our chemical model cannot treat shocked gas. Outflows and accretion both shock the gas, can destroy the dust and affect local chemistry drastically. Hence adding shock chemistry to the chemical model as well as proper temperature estimation of outflow gas can improve this work.

In order to properly disentangle the effects of outflow feedback and episodic accretion, one needs to perform hydrodynamic simulations with and without each process, covering all 4 combination with the same initial condition and perform the same pipeline to post-process with chemistry code and compare the results.

Finally one can expand the same simulations to bigger chemical networks, which include bigger iCOMs, which are signatures for hot coronas.

### 5.2.2 Synthetic emission maps and comparison with observation

Comparing simulation results with observation can be a difficult task. First off, one cannot directly compare the simulated abundance of different species with the intensity we have from observation. One needs to solve the radiative transfer equation for the emission from the emitting material to produce synthetic spectra and then convolve it to produce synthetic observations. The next natural step for this work is to perform such calculations by a program such as RADMC-3D or XCLASS (Möller et al., 2017).

Moreover, since the parameter space of astronomical objects are very big, and we do not know the initial condition of the star formation, comparing the simulations and observations one to one can be misleading. One needs to perform many simulations to cover the parameter space and achieve good number statistics, then use big survey observational data and perform similar statistical analysis on both data set to properly compare them with each other. This is the way to go in order to inform our future models with real observational data and understand the star formation process.

## References

- Allen, M., & Robinson, G. W. (1977, March). The molecular composition of dense interstellar clouds. *Astrophysical Journal*, *212*, 396-415. doi: 10.1086/155059
- André, P., Di Francesco, J., Ward-Thompson, D., Inutsuka, S. I., Pudritz, R. E., & Pineda, J. E. (2014, January). From Filamentary Networks to Dense Cores in Molecular Clouds: Toward a New Paradigm for Star Formation. In H. Beuther, R. S. Klessen, C. P. Dullemond, & T. Henning (Eds.), *Protostars and planets vi* (p. 27-51). doi: 10.2458/azu\_uapress\_9780816531240-ch002
- Arrhenius, S. (1889). Über die reaktionsgeschwindigkeit bei der inversion von rohrzucker durch säuren. *Zeitschrift für physikalische Chemie*, *4*(1), 226–248.
- Audard, M., Ábrahám, P., Dunham, M. M., Green, J. D., Grosso, N., Hamaguchi, K., . . . Zhu, Z. (2014, January). Episodic Accretion in Young Stars. In H. Beuther, R. S. Klessen, C. P. Dullemond, & T. Henning (Eds.), *Protostars and planets vi* (p. 387-410). doi: 10.2458/azu\_uapress\_9780816531240-ch017
- Bacmann, A., Taquet, V., Faure, A., Kahane, C., & Ceccarelli, C. (2012, May). Detection of complex organic molecules in a prestellar core: a new challenge for astrochemical models. *Astronomy and Astrophysics*, *541*, L12. doi: 10.1051/0004-6361/201219207
- Balbus, S. A., & Hawley, J. F. (1998, January). Instability, turbulence, and enhanced transport in accretion disks. *Reviews of Modern Physics*, *70*(1), 1-53. doi: 10.1103/RevModPhys.70.1
- Baldwin, J. A., Ferland, G. J., Martin, P. G., Corbin, M. R., Cota, S. A., Peterson, B. M., & Slettebak, A. (1991, June). Physical Conditions in the Orion Nebula and an Assessment of Its Helium Abundance. *Astrophysical Journal*, *374*, 580. doi: 10.1086/170146
- Barnes, J., & Hut, P. (1986, December). A hierarchical  $O(N \log N)$  force-calculation algorithm. *Nature*, *324*(6096), 446-449. doi: 10.1038/324446a0
- Bate, M. R., Bonnell, I. A., & Price, N. M. (1995, November). Modelling accretion in protobinary systems. *Monthly Notices of the Royal Astronomical Society*, *277*(2), 362-376. doi: 10.1093/mnras/277.2.362

- Benson, P. J., & Myers, P. C. (1989, September). A Survey for Dense Cores in Dark Clouds. *Astrophysical Journal, Supplement*, 71, 89. doi: 10.1086/191365
- Bergin, E. A., Langer, W. D., & Goldsmith, P. F. (1995, March). Gas-Phase Chemistry in Dense Interstellar Clouds Including Grain Surface Molecular Depletion and Desorption. *Astrophysical Journal*, 441, 222. doi: 10.1086/175351
- Bertin, M., Romanzin, C., Doronin, M., Philippe, L., Jeseck, P., Ligterink, N., ... Fillion, J.-H. (2016, February). UV Photodesorption of Methanol in Pure and CO-rich Ices: Desorption Rates of the Intact Molecule and of the Photofragments. *Astrophysical Journal, Letters*, 817(2), L12. doi: 10.3847/2041-8205/817/2/L12
- Bjorkman, J. E., & Wood, K. (2001, June). Radiative Equilibrium and Temperature Correction in Monte Carlo Radiation Transfer. *Astrophysical Journal*, 554(1), 615-623. doi: 10.1086/321336
- Bodenheimer, P., Laughlin, G. P., Rozyczka, M., Plewa, T., & Yorke, H. W. (2006). *Numerical methods in astrophysics: an introduction*. CRC Press.
- Bonnor, W. B. (1956, January). The Formation of the Nebulae. With 3 Figures. *Zeitschrift fuer Astrophysik*, 39, 143.
- Bouvier, J., Alencar, S. H. P., Harries, T. J., Johns-Krull, C. M., & Romanova, M. M. (2007, January). Magnetospheric Accretion in Classical T Tauri Stars. In B. Reipurth, D. Jewitt, & K. Keil (Eds.), *Protostars and planets v* (p. 479). doi: 10.48550/arXiv.astro-ph/0603498
- Canosa, A., Sims, I. R., Travers, D., Smith, I. W. M., & Rowe, B. R. (1997, July). Reactions of the methylidene radical with CH<sub>4</sub>, C<sub>2</sub>H<sub>2</sub>, C<sub>2</sub>H<sub>4</sub>, C<sub>2</sub>H<sub>6</sub>, and but-1-ene studied between 23 and 295K with a CRESU apparatus. *Astronomy and Astrophysics*, 323, 644-651.
- Caselli, P., Hasegawa, T. I., & Herbst, E. (1998, March). A Proposed Modification of the Rate Equations for Reactions on Grain Surfaces. *Astrophysical Journal*, 495(1), 309-316. doi: 10.1086/305253
- Caselli, P., Stantcheva, T., Shalabiea, O., Shematovich, V. I., & Herbst, E. (2002, October). Deuterium fractionation on interstellar grains studied with modified rate equations and a Monte Carlo approach. *Planetary Space Science*, 50(12-13), 1257-1266. doi: 10.1016/S0032-0633(02)00092-2
- Cazaux, S., Tielens, A. G. G. M., Ceccarelli, C., Castets, A., Wakelam, V., Caux, E., ... Teyssier, D. (2003, August). The Hot Core around the Low-mass

- Protostar IRAS 16293-2422: Scoundrels Rule! *Astrophysical Journal, Letters*, 593(1), L51-L55. doi: 10.1086/378038
- Ceccarelli, C. (2004, December). The Hot Corinos of Solar Type Protostars. In D. Johnstone, F. C. Adams, D. N. C. Lin, D. A. Neufeld, & E. C. Ostriker (Eds.), *Star formation in the interstellar medium: In honor of david hollenbach* (Vol. 323, p. 195).
- Ceccarelli, C., Caselli, P., Fontani, F., Neri, R., López-Sepulcre, A., Codella, C., ... Yamamoto, S. (2017, December). Seeds Of Life In Space (SOLIS): The Organic Composition Diversity at 300-1000 au Scale in Solar-type Star-forming Regions. *Astrophysical Journal*, 850(2), 176. doi: 10.3847/1538-4357/aa961d
- Ceccarelli, C., Codella, C., Balucani, N., Bockelée-Morvan, D., Herbst, E., Vastel, C., ... Yamamoto, S. (2023, April). "organic chemistry in the first phases of solar-type protostars ". In S. Inutsuka, Y. Aikawa, T. Muto, K. Tomida, & T. Motohide (Eds.), *Protostars and planets vii* (Vol. 534, p. 379).
- Chevance, M., Krumholz, M. R., McLeod, A. F., Ostriker, E. C., Rosolowsky, E. W., & Sternberg, A. (2022, March). The Life and Times of Giant Molecular Clouds. *arXiv e-prints*, arXiv:2203.09570. doi: 10.48550/arXiv.2203.09570
- Choudhury, R., Schilke, P., Stéphan, G., Bergin, E., Möller, T., Schmiedeke, A., & Zernickel, A. (2015, March). Evolution of complex organic molecules in hot molecular cores. Synthetic spectra at (sub-)mm wavebands. *Astronomy and Astrophysics*, 575, A68. doi: 10.1051/0004-6361/201424499
- Dobbs, C. L., Krumholz, M. R., Ballesteros-Paredes, J., Bolatto, A. D., Fukui, Y., Heyer, M., ... Vázquez-Semadeni, E. (2014, January). Formation of Molecular Clouds and Global Conditions for Star Formation. In H. Beuther, R. S. Klessen, C. P. Dullemond, & T. Henning (Eds.), *Protostars and planets vi* (p. 3-26). doi: 10.2458/azu\_uapress\_9780816531240-ch001
- Draine, B. T. (2010). *Physics of the interstellar and intergalactic medium* (Vol. 19). Princeton University Press.
- Dullemond, C. P., Juhasz, A., Pohl, A., Sereshti, F., Shetty, R., Peters, T., ... Flock, M. (2012, February). *RADMC-3D: A multi-purpose radiative transfer tool*. Astrophysics Source Code Library, record ascl:1202.015.
- Dunham, J., T. (1937, February). Interstellar Neutral Potassium and Neutral Calcium. *Publications of the ASP*, 49(287), 26-28. doi: 10.1086/124759

- Durisen, R. H., Boss, A. P., Mayer, L., Nelson, A. F., Quinn, T., & Rice, W. K. M. (2007, January). Gravitational Instabilities in Gaseous Protoplanetary Disks and Implications for Giant Planet Formation. In B. Reipurth, D. Jewitt, & K. Keil (Eds.), *Protostars and planets v* (p. 607). doi: 10.48550/arXiv.astro-ph/0603179
- Ebert, R. (1957, January). Zur Instabilität kugelsymmetrischer Gasverteilungen. Mit 2 Textabbildungen. *Zeitschrift fuer Astrophysik*, *42*, 263.
- Espaillet, C. C., Robinson, C. E., Romanova, M. M., Thanathibodee, T., Wendeborn, J., Calvet, N., ... Muzerolle, J. (2021, September). Measuring the density structure of an accretion hot spot. *Nature*, *597*(7874), 41-44. doi: 10.1038/s41586-021-03751-5
- Evans, I., Neal J., Dunham, M. M., Jørgensen, J. K., Enoch, M. L., Merín, B., van Dishoeck, E. F., ... Sargent, A. I. (2009, April). The Spitzer c2d Legacy Results: Star-Formation Rates and Efficiencies; Evolution and Lifetimes. *Astrophysical Journal*, *181*(2), 321-350. doi: 10.1088/0067-0049/181/2/321
- Fischer, W. J., Hillenbrand, L. A., Herczeg, G. J., Johnstone, D., Kóspál, Á., & Dunham, M. M. (2022, March). Accretion Variability as a Guide to Stellar Mass Assembly. *arXiv e-prints*, arXiv:2203.11257. doi: 10.48550/arXiv.2203.11257
- Fleck, J., J. A., & Canfield, E. H. (1984, June). A Random Walk Procedure for Improving the Computational Efficiency of the Implicit Monte Carlo Method for Nonlinear Radiation Transport. *Journal of Computational Physics*, *54*(3), 508-523. doi: 10.1016/0021-9991(84)90130-X
- Garrod, R. T. (2008, November). A new modified-rate approach for gas-grain chemical simulations. *Astronomy and Astrophysics*, *491*(1), 239-251. doi: 10.1051/0004-6361:200810518
- Garrod, R. T., Wakelam, V., & Herbst, E. (2007, June). Non-thermal desorption from interstellar dust grains via exothermic surface reactions. *Astronomy and Astrophysics*, *467*(3), 1103-1115. doi: 10.1051/0004-6361:20066704
- Gingold, R. A., & Monaghan, J. J. (1977, November). Smoothed particle hydrodynamics: theory and application to non-spherical stars. *Monthly Notices of the Royal Astronomical Society*, *181*, 375-389. doi: 10.1093/mnras/181.3.375
- Glover, S. C. O., & Clark, P. C. (2012, March). Approximations for modelling CO chemistry in giant molecular clouds: a comparison of approaches. *Monthly Notices of the Royal Astronomical Society*, *421*(1), 116-131. doi: 10.1111/j.1365-2966.2011.20260.x

- Goldsmith, P. F. (2001, August). Molecular Depletion and Thermal Balance in Dark Cloud Cores. *Astrophysical Journal*, *557*(2), 736-746. doi: 10.1086/322255
- Graninger, D. M., Herbst, E., Öberg, K. I., & Vasyunin, A. I. (2014, May). The HNC/HCN Ratio in Star-forming Regions. *Astrophysical Journal*, *787*(1), 74. doi: 10.1088/0004-637X/787/1/74
- Gredel, R., Lepp, S., Dalgarno, A., & Herbst, E. (1989, December). Cosmic-Ray-induced Photodissociation and Photoionization Rates of Interstellar Molecules. *Astrophysical Journal*, *347*, 289. doi: 10.1086/168117
- Hasegawa, T. I., & Herbst, E. (1993, March). New gas-grain chemical models of quiescent dense interstellar clouds :the effects of H<sub>2</sub> tunnelling reactions and cosmic ray induced desorption. *Monthly Notices of the Royal Astronomical Society*, *261*, 83-102. doi: 10.1093/mnras/261.1.83
- Hasegawa, T. I., Herbst, E., & Leung, C. M. (1992, September). Models of Gas-Grain Chemistry in Dense Interstellar Clouds with Complex Organic Molecules. *Astrophysical Journal, Supplement*, *82*, 167. doi: 10.1086/191713
- Herbst, E., & van Dishoeck, E. F. (2009, September). Complex Organic Interstellar Molecules. *annual review of astronomy and astrophysics*, *47*(1), 427-480. doi: 10.1146/annurev-astro-082708-101654
- Hollenbach, D., & McKee, C. F. (1979, November). Molecule formation and infrared emission in fast interstellar shocks. I. Physical processes. *Astrophysical Journal, Supplement*, *41*, 555-592. doi: 10.1086/190631
- Hollenbach, D., & Salpeter, E. E. (1970, July). Surface Adsorption of Light Gas Atoms. *Journal of Chemical Physics*, *53*(1), 79-86. doi: 10.1063/1.1673836
- Hubber, D. A., Rosotti, G. P., & Booth, R. A. (2018, January). GANDALF - Graphical Astrophysics code for N-body Dynamics And Lagrangian Fluids. *Monthly Notices of the Royal Astronomical Society*, *473*(2), 1603-1632. doi: 10.1093/mnras/stx2405
- Hubber, D. A., Walch, S., & Whitworth, A. P. (2013, April). An improved sink particle algorithm for SPH simulations. *Monthly Notices of the Royal Astronomical Society*, *430*(4), 3261-3275. doi: 10.1093/mnras/stt128
- Jiménez-Serra, I., Vasyunin, A. I., Caselli, P., Marcelino, N., Billot, N., Viti, S., ... Bachiller, R. (2016, October). The Spatial Distribution of Complex Organic

Molecules in the L1544 Pre-stellar Core. *Astrophysical Journal, Letters*, 830(1), L6. doi: 10.3847/2041-8205/830/1/L6

Jørgensen, J. K., Belloche, A., & Garrod, R. T. (2020). Astrochemistry during the formation of stars. *Annual Review of Astronomy and Astrophysics*, 58, 727–778.

Kenyon, S. J., & Hartmann, L. (1995, November). Pre-Main-Sequence Evolution in the Taurus-Auriga Molecular Cloud. *Astrophysical Journal*, 101, 117. doi: 10.1086/192235

Kenyon, S. J., Hartmann, L. W., Strom, K. M., & Strom, S. E. (1990, March). An IRAS Survey of the Taurus-Auriga Molecular Cloud. *Astrophysical Journal*, 99, 869. doi: 10.1086/115380

Klessen, R. S., & Glover, S. C. O. (2016, January). Physical Processes in the Interstellar Medium. In Y. Revaz, P. Jablonka, R. Teyssier, & L. Mayer (Eds.), *Saas-fee advanced course* (Vol. 43, p. 85). doi: 10.1007/978-3-662-47890-5\_2

Leger, A., Jura, M., & Omont, A. (1985, March). Desorption from interstellar grains. *Astronomy and Astrophysics*, 144(1), 147-160.

Loison, J.-C., Wakelam, V., & Hickson, K. M. (2014, September). The interstellar gas-phase chemistry of HCN and HNC. *Monthly Notices of the Royal Astronomical Society*, 443(1), 398-410. doi: 10.1093/mnras/stu1089

Lombardi, J. C., McInally, W. G., & Faber, J. A. (2015, February). An efficient radiative cooling approximation for use in hydrodynamic simulations. *Monthly Notices of the Royal Astronomical Society*, 447(1), 25-35. doi: 10.1093/mnras/stu2432

Lucy, L. B. (1977, December). A numerical approach to the testing of the fission hypothesis. *Astronomical Journal*, 82, 1013-1024. doi: 10.1086/112164

Martín-Doménech, R., Muñoz Caro, G. M., & Cruz-Díaz, G. A. (2016, May). Study of the photon-induced formation and subsequent desorption of CH<sub>3</sub>OH and H<sub>2</sub>CO in interstellar ice analogs. *Astronomy and Astrophysics*, 589, A107. doi: 10.1051/0004-6361/201528025

Matzner, C. D., & McKee, C. F. (1999, December). Bipolar Molecular Outflows Driven by Hydromagnetic Protostellar Winds. *Astrophysical Journal, Letters*, 526(2), L109-L112. doi: 10.1086/312376

- McElroy, D., Walsh, C., Markwick, A. J., Cordiner, M. A., Smith, K., & Millar, T. J. (2013, February). The UMIST database for astrochemistry 2012. *Astronomy and Astrophysics*, *550*, A36. doi: 10.1051/0004-6361/201220465
- Min, M., Dullemond, C. P., Dominik, C., de Koter, A., & Hovenier, J. W. (2009, April). Radiative transfer in very optically thick circumstellar disks. *Astronomy and Astrophysics*, *497*(1), 155-166. doi: 10.1051/0004-6361/200811470
- Minissale, M., Dulieu, F., Cazaux, S., & Hocuk, S. (2016, January). Dust as interstellar catalyst. I. Quantifying the chemical desorption process. *Astronomy and Astrophysics*, *585*, A24. doi: 10.1051/0004-6361/201525981
- Möller, T., Endres, C., & Schilke, P. (2017, February). eXtended CASA Line Analysis Software Suite (XCLASS). *Astronomy and Astrophysics*, *598*, A7. doi: 10.1051/0004-6361/201527203
- Nakano, T., Hasegawa, T., Morino, J.-I., & Yamashita, T. (2000, May). Evolution of Protostars Accreting Mass at Very High Rates: Is Orion IRc2 a Huge Protostar? *Astrophysical Journal*, *534*(2), 976-983. doi: 10.1086/308765
- Nakano, T., Hasegawa, T., & Norman, C. (1995, September). The Mass of a Star Formed in a Cloud Core: Theory and Its Application to the Orion A Cloud. *Astrophysical Journal*, *450*, 183. doi: 10.1086/176130
- Nelson, R. P., & Langer, W. D. (1997, June). The Dynamics of Low-Mass Molecular Clouds in External Radiation Fields. *Astrophysical Journal*, *482*(2), 796-826. doi: 10.1086/304167
- Neufeld, D. A., & Dalgarno, A. (1989, May). Fast Molecular Shocks. I. Reformation of Molecules behind a Dissociative Shock. *Astrophysical Journal*, *340*, 869. doi: 10.1086/167441
- Offner, S. S. R., Klein, R. I., McKee, C. F., & Krumholz, M. R. (2009, September). The Effects of Radiative Transfer on Low-Mass Star Formation. *Astrophysical Journal*, *703*(1), 131-149. doi: 10.1088/0004-637X/703/1/131
- Ossenkopf, V., & Henning, T. (1994, November). Dust opacities for protostellar cores. *Astronomy and Astrophysics*, *291*, 943-959.
- Osterbrock, D. E., Tran, H. D., & Veilleux, S. (1992, April). Faint Emission Lines in the Spectrum of the Orion Nebula and the Abundances of Some of the Rarer Elements. *Astrophysical Journal*, *389*, 305. doi: 10.1086/171206

- Pineda, J. E., Arzoumanian, D., André, P., Friesen, R. K., Zavagno, A., Clarke, S. D., ... Kuffmeier, M. (2022, May). From Bubbles and Filaments to Cores and Disks: Gas Gathering and Growth of Structure Leading to the Formation of Stellar Systems. *arXiv e-prints*, arXiv:2205.03935. doi: 10.48550/arXiv.2205.03935
- Potapov, A., Jäger, C., Henning, T., Jonusas, M., & Krim, L. (2017, September). The Formation of Formaldehyde on Interstellar Carbonaceous Grain Analogs by O/H Atom Addition. *Astrophysical Journal*, *846*(2), 131. doi: 10.3847/1538-4357/aa85e8
- Prasad, S. S., & Tarafdar, S. P. (1983, April). UV radiation field inside dense clouds - Its possible existence and chemical implications. *Astrophysical Journal*, *267*, 603-609. doi: 10.1086/160896
- Price, D. J. (2012, February). Smoothed particle hydrodynamics and magnetohydrodynamics. *Journal of Computational Physics*, *231*(3), 759-794. doi: 10.1016/j.jcp.2010.12.011
- Robitaille, T. P. (2010, September). On the modified random walk algorithm for Monte-Carlo radiation transfer. *Astronomy and Astrophysics*, *520*, A70. doi: 10.1051/0004-6361/201015025
- Rohde, P. F., Walch, S., Clarke, S. D., Seifried, D., Whitworth, A. P., & Klepitko, A. (2021, January). The impact of episodic outflow feedback on stellar multiplicity and the star formation efficiency. *Monthly Notices of the Royal Astronomical Society*, *500*(3), 3594-3612. doi: 10.1093/mnras/staa2926
- Rohde, P. F., Walch, S., Seifried, D., Whitworth, A. P., & Clarke, S. D. (2022, February). Protostellar outflows: a window to the past. *Monthly Notices of the Royal Astronomical Society*, *510*(2), 2552-2571. doi: 10.1093/mnras/stab3572
- Rohde, P. F., Walch, S., Seifried, D., Whitworth, A. P., Clarke, S. D., & Hubber, D. A. (2019, February). Evolution of Hubble wedges in episodic protostellar outflows. *Monthly Notices of the Royal Astronomical Society*, *483*(2), 2563-2580. doi: 10.1093/mnras/sty3302
- Sakai, N., & Yamamoto, S. (2013, December). Warm Carbon-Chain Chemistry. *Chemical Reviews*, *113*(12), 8981-9015. doi: 10.1021/cr4001308
- Schaefer, D. (2017). *Modeling Icy Dust Mantles: A Multi-Phase Model for Gas-Grain Chemistry in the Rate Equation Approach* (Unpublished master's thesis). Universität zu Köln", Germany.

- Semenov, D., Hersant, F., Wakelam, V., Dutrey, A., Chapillon, E., Guilloteau, S., . . . Schreyer, K. (2010, November). Chemistry in disks. IV. Benchmarking gas-grain chemical models with surface reactions. *Astronomy and Astrophysics*, *522*, A42. doi: 10.1051/0004-6361/201015149
- Shen, C. J., Greenberg, J. M., Schutte, W. A., & van Dishoeck, E. F. (2004, February). Cosmic ray induced explosive chemical desorption in dense clouds. *Astronomy and Astrophysics*, *415*, 203-215. doi: 10.1051/0004-6361:20031669
- Shu, F. H. (1991). *The physics of astrophysics: Gas dynamics* (Vol. 2). University Science Books.
- Smith, I. W. M., Sage, A. M., Donahue, N. M., Herbst, E., & Quan, D. (2006, January). The temperature-dependence of rapid low temperature reactions: experiment, understanding and prediction. *Faraday Discussions*, *133*, 137. doi: 10.1039/b600721j
- Springel, V. (2010, September). Smoothed Particle Hydrodynamics in Astrophysics. *annual review of astronomy and astrophysics*, *48*, 391-430. doi: 10.1146/annurev-astro-081309-130914
- Stamatellos, D., Whitworth, A. P., Bisbas, T., & Goodwin, S. (2007, November). Radiative transfer and the energy equation in SPH simulations of star formation. *Astronomy and Astrophysics*, *475*(1), 37-49. doi: 10.1051/0004-6361:20077373
- Stamatellos, D., Whitworth, A. P., & Hubber, D. A. (2012, December). Episodic accretion, protostellar radiative feedback, and their role in low-mass star formation. *Monthly Notices of the Royal Astronomical Society*, *427*(2), 1182-1193. doi: 10.1111/j.1365-2966.2012.22038.x
- Stéphan, G., Schilke, P., Le Bourlot, J., Schmiedeke, A., Choudhury, R., Godard, B., & Sánchez-Monge, Á. (2018, September). Chemical modeling of internal photon-dominated regions surrounding deeply embedded HC/UCHII regions. *Astronomy and Astrophysics*, *617*, A60. doi: 10.1051/0004-6361/201730639
- Suzuki, H., Yamamoto, S., Ohishi, M., Kaifu, N., Ishikawa, S.-I., Hirahara, Y., & Takano, S. (1992, June). A Survey of CCS, HC 3N, HC 5N, and NH 3 toward Dark Cloud Cores and Their Production Chemistry. *Astrophysical Journal*, *392*, 551. doi: 10.1086/171456
- Swings, P., & Rosenfeld, L. (1937, November). Considerations Regarding Interstellar Molecules. *Astrophysical Journal*, *86*, 483-486. doi: 10.1086/143880

- Tan, J. C., & McKee, C. F. (2004, March). The Formation of the First Stars. I. Mass Infall Rates, Accretion Disk Structure, and Protostellar Evolution. *Astrophysical Journal*, *603*(2), 383-400. doi: 10.1086/381490
- Taquet, V., Wirström, E. S., Charnley, S. B., Faure, A., López-Sepulcre, A., & Persson, C. M. (2017, October). Chemical complexity induced by efficient ice evaporation in the Barnard 5 molecular cloud. *Astronomy and Astrophysics*, *607*, A20. doi: 10.1051/0004-6361/201630023
- Tielens, A. G. G. M. (2005). *The Physics and Chemistry of the Interstellar Medium*.
- Tielens, A. G. G. M., & Hagen, W. (1982, October). Model calculations of the molecular composition of interstellar grain mantles. *Astronomy and Astrophysics*, *114*(2), 245-260.
- Toulemonde, M., Dufour, C., Meftah, A., & Paumier, E. (2000, 05). Transient thermal processes in heavy ion irradiation of crystalline inorganic insulators. *Nuclear Instruments & Methods in Physics Research Section B-beam Interactions With Materials and Atoms - NUCL INSTRUM METH PHYS RES B*, *166*, 903-912. doi: 10.1016/S0168-583X(99)00799-5
- van Dishoeck, E. F. (2018, September). Astrochemistry: overview and challenges. *IAU Symposium*, *332*, 3-22. doi: 10.1017/S1743921317011528
- Vastel, C., Ceccarelli, C., Lefloch, B., & Bachiller, R. (2014, November). The Origin of Complex Organic Molecules in Prestellar Cores. *Astrophysical Journal Letters*, *795*(1), L2. doi: 10.1088/2041-8205/795/1/L2
- Vidali, G. (2013, December). H<sub>2</sub> Formation on Interstellar Grains. *Chemical Reviews*, *113*(12), 8752-8782. doi: 10.1021/cr400156b
- Wakelam, V., Dartois, E., Chabot, M., Spezzano, S., Navarro-Almáida, D., Loison, J. C., & Fuente, A. (2021, August). Efficiency of non-thermal desorptions in cold-core conditions. Testing the sputtering of grain mantles induced by cosmic rays. *Astronomy and Astrophysics*, *652*, A63. doi: 10.1051/0004-6361/202039855
- Wakelam, V., & Herbst, E. (2008, June). Polycyclic Aromatic Hydrocarbons in Dense Cloud Chemistry. *Astrophysical Journal*, *680*(1), 371-383. doi: 10.1086/587734
- Wakelam, V., Herbst, E., Loison, J. C., Smith, I. W. M., Chandrasekaran, V., Pavone, B., ... Wiesenfeld, L. (2012, March). A KInetic Database for

- Astrochemistry (KIDA). *Astrophysical Journal, Supplement*, 199(1), 21. doi: 10.1088/0067-0049/199/1/21
- Wakelam, V., Smith, I. W. M., Herbst, E., Troe, J., Geppert, W., Linnartz, H., ... Talbi, D. (2010, October). Reaction Networks for Interstellar Chemical Modelling: Improvements and Challenges. *Space Science Reviews*, 156(1-4), 13-72. doi: 10.1007/s11214-010-9712-5
- Walch, S., Naab, T., Whitworth, A., Burkert, A., & Gritschneider, M. (2010, March). Protostellar discs formed from turbulent cores. *Monthly Notices of the Royal Astronomical Society*, 402(4), 2253-2263. doi: 10.1111/j.1365-2966.2009.16058.x
- Ward-Thompson, D., & Whitworth, A. P. (2011). *An introduction to star formation*. Cambridge University Press.
- Yamamoto, S. (2017). Introduction to astrochemistry. *Editorial: Springer*, 614.
- Yamamoto, T., Miura, H., & Shalabiea, O. M. (2019, November). Thermal desorption induced by chemical reaction on dust surface. *Monthly Notices of the Royal Astronomical Society*, 490(1), 709-717. doi: 10.1093/mnras/stz2583
- Zhou, S., Wu, Y. F., Evans, I. N. J., Fuller, G. A., & Myers, P. C. (1989, January). A CS Survey of Dense Molecular Cloud Cores. In *Bulletin of the american astronomical society* (Vol. 21, p. 715).
- Zhu, Z., Hartmann, L., & Gammie, C. (2009, April). Nonsteady Accretion in Protostars. *Astrophysical Journal*, 694(2), 1045-1055. doi: 10.1088/0004-637X/694/2/1045
- Zhu, Z., Hartmann, L., Gammie, C., & McKinney, J. C. (2009, August). Two-dimensional Simulations of FU Orionis Disk Outbursts. *Astrophysical Journal*, 701(1), 620-634. doi: 10.1088/0004-637X/701/1/620
- Zhu, Z., Hartmann, L., Gammie, C. F., Book, L. G., Simon, J. B., & Engelhard, E. (2010, April). Long-term Evolution of Protostellar and Protoplanetary Disks. I. Outbursts. *Astrophysical Journal*, 713(2), 1134-1142. doi: 10.1088/0004-637X/713/2/1134

# Selbstständigkeitserklärung

Hiermit versichere ich an Eides statt, dass ich die vorliegende Dissertation selbstständig und ohne die Benutzung anderer als der angegebenen Hilfsmittel und Literatur angefertigt habe. Alle Stellen, die wörtlich oder sinngemäß aus veröffentlichten und nicht veröffentlichten Werken dem Wortlaut oder dem Sinn nach entnommen wurden, sind als solche kenntlich gemacht. Ich versichere an Eides statt, dass diese Dissertation noch keiner anderen Fakultät oder Universität zur Prüfung vorgelegen hat; dass sie - abgesehen von unten angegebenen Teilpublikationen und eingebundenen Artikeln und Manuskripten - noch nicht veröffentlicht worden ist sowie, dass ich eine Veröffentlichung der Dissertation vor Abschluss der Promotion nicht ohne Genehmigung des Promotionsausschusses vornehmen werde. Die Bestimmungen dieser Ordnung sind mir bekannt. Darüber hinaus erkläre ich hiermit, dass ich die Ordnung zur Sicherung guter wissenschaftlicher Praxis und zum Umgang mit wissenschaftlichem Fehlverhalten der Universität zu Köln gelesen und sie bei der Durchführung der Dissertation zugrundeliegenden Arbeiten und der schriftlich verfassten Dissertation beachtet habe und verpflichte mich hiermit, die dort genannten Vorgaben bei allen wissenschaftlichen Tätigkeiten zu beachten und umzusetzen. Ich versichere, dass die eingereichte elektronische Fassung der eingereichten Druckfassung vollständig entspricht.

Teilpublikationen:

Dynamic chemistry: effects of episodic accretion

Tanha et al. 2024 in prep.

(Copy) **Nassim Tanha**

Köln, den 11.08.2023

## Data availability

All data and code routines used in this work can be made available upon request to the Supervisor.

## Acknowledgement

First and foremost I would like to sincerely thank my supervisor, Prof. Schilke, for his scientific support and his understanding throughout the years we worked together. His kindness and flexibility in supporting me, when things do not go smoothly has been a source of strength. I would also like to extend my thanks to the member of my thesis advisory committee, Prof. Stefanie Walch-Gassner and Dr. Volker Ossenkopf-Okada and my second examiner Prof. Gary Fuller, whose guidance was of great help during this project and Prof. Dr. Susanne Crewell, for chairing my thesis committee.

One person without whom this thesis might have never succeeded is Dr. Seamus Clarke. A great colleague and even better friend. I consider him to be my unofficial additional supervisor. He always generously share his time to discuss ideas with me. Thank you for all the laughter and meals we shared. You made the first years of my PhD a very joyful one. No matter how much one likes their work, if not for good colleagues and office-mates, the work space becomes stale. I am grateful to all my coworkers, especially Pierre, Shashwata, Annika, Alvaro, Wonju and Massato, with whom I spent working hours happily. Another special thanks goes to those who proof-read this manuscript and helped me with my many spelling (and other) mistakes. Seamus, Shashwata, Katya, Massato and Pierre, thank you all. You are lifesavers.

The last year was the most difficult year of my life. The fact that I not only survived it, but also thrived, is because of the amazing support system I have. Thank you Rose, I would not have been here without you. To my dear friends in Iran, Khorshid and Maryam, you were there whenever I needed you. You listened to me and comforted me, when my life was too difficult to handle alone. To my wonderful friends in Berlin, Homa and Maryam, I cannot thank you enough for taking over some of my responsibilities, when I did not have the capacity for them. I am eternally grateful.

I would like to thank my family. Your love is a great source of strength in my life. And finally, I like to thank myself. For being persistent, for being true to myself, for being patient and resilient.